A STUDY OF THE EFFECTS OF

INLET PRESWIRL ON THE DYNAMIC COEFFICIENTS OF A STRAIGHT-BORE

HONEYCOMB GAS DAMPER SEAL

A Thesis

by

TONY BRANDON SPROWL

Submitted to the Office of Graduate Studies of
Texas A&M University
in partial fulfillment of the requirements for the degree of

MASTER OF SCIENCE

December 2003

Major Subject: Mechanical Engineering

A STUDY OF THE EFFECTS OF

INLET PRESWIRL ON THE DYNAMIC COEFFICIENTS OF A STRAIGHT-BORE

HONEYCOMB GAS DAMPER SEAL

A Thesis

by

TONY BRANDON SPROWL

Submitted to Texas A&M University
in partial fulfillment of the requirements
for the degree of

MASTER OF SCIENCE

Approved as to style and content by:

Dara W. Childs	Arun Srinivasa
(Chair of Committee)	(Member)
Ronald Darby	Dennis O'Neal
(Member)	(Head of Department)

December 2003

Major Subject: Mechanical Engineering

ABSTRACT

A Study of the Effects of Inlet Preswirl on the Dynamic Coefficients

of a Straight-Bore Honeycomb Gas Damper Seal. (December 2003)

Tony Brandon Sprowl, B.S.,

The University of Southwestern Louisiana

Chair of Advisory Committee: Dr. Dara W. Childs

In high-pressure centrifugal compressors, honeycomb seals are often used as replacements for labyrinth seals to enhance dynamic stability. A concern exists with the loss of this enhanced stability if the honeycomb cavities become clogged with debris over time. So, as a first objective, static and dynamic tests were conducted on a constant-clearance honeycomb and a constant-clearance smooth-bore seal under three inlet preswirl conditions to determine the effects of inlet preswirl. The resulting leakage flowrate and dynamic parameters, effective stiffness and damping of the seal, were measured for each seal and then compared, with the smooth-bore seal representing the honeycomb seal with completely clogged cells. The second objective was to evaluate a two-control volume theory by Kleynhans and Childs with the measured data under the influence of preswirl.

Both seals have a 114.7mm bore with a radial clearance of 0.2mm from the test rotor. The honeycomb seal has a cell width of 0.79mm and cell depth of 3.2mm. The target test matrix for each preswirl setting consisted of three exit-to-inlet pressure ratios

of 15%, 35%, and 50%, and three rotor speeds out to 20,200 rpm. The target inlet air pressure was 70 bar-a.

Experimental results show that, for a clean honeycomb seal, preswirl has little effect on effective stiffness, K_{eff}*, and decreases effective damping, C_{eff}*, by about 20% at the high inlet preswirl ratio (~0.6). However, comparing smooth and honeycomb seal results at higher inlet preswirl shows a potential reduction in K_{eff}* by up to 68%, and a large drop and shift in positive C_{eff}* values, which could cause an instability in the lower frequency range. Measured leakage shows a potential increase of about 80%, regardless of test conditions. A swirl brake at the seal entrance would fix this loss in stability by significantly reducing inlet preswirl.

The two-control-volume theory model by Kleynhans and Childs seems to follow the frequency-dependent experimental data well for the honeycomb seal. Theory predicts conservatively (under-predicts) for stability parameters such as k* and C_{eff}* and for leakage. Predictions for K and K_{eff} may possibly be improved with better measured friction factor coefficients for each seal.

ACKNOWLEDGEMENTS

I would like to start by thanking Dr. Childs for his direction, insight, and most of all for his patience in finishing this research and this thesis. I would also like to thank Stephen Phillips for his technical aptitude and dedication when unforeseen problems arose.

I would like to extend my appreciation to my colleagues and friends, Mark Weatherwax and Jeremy Carter, who were selfless in their work to help me finish. Special thanks also to Christopher Holt and Matthew Dawson whose research served as a foundation for me to build upon.

Finally, I would like to thank my parents and my wife, Alicia, for encouraging me to press on to completion. Most importantly, I would like to thank my Lord Jesus Christ for the opportunity to fulfill this dream.

TABLE OF CONTENTS

LIST OF FIGURES

LIST OF TABLES

Page

NOMENCLATURE

<u>Roman</u>

A Precession amplitude [L]

A_c Cross-sectional area [L^2]

C, c Direct and cross-coupled damping coefficients [F*t/L]

C^*, c^* Non-dimensional direct and cross-coupled damping coefficients [t]

C_d Discharge coefficient [-]

C_{eff} Effective damping coefficient [F*t/L]

C_{eff}^* Non-dimensional effective damping coefficient [t]

C_r Radial clearance between stator and rotor [L]

D Direct impedance [F/L]

D_{in} Seal inner diameter [L]

E Cross-coupled impedance [F/L]

f Blasius friction factor

F_x, F_y Seal reaction forces [F]

F_r, F_θ Radial and tangential seal reaction forces [F]

H Radial clearance between stator and rotor [L]

$H_{xx}, H_{xy}, H_{yx}, H_{yy}$ Frequency response functions [F/L]

i $\sqrt{-1}$

$Im[]$ Imaginary part

I_R, I_θ Radial and tangential impedance [F/L]

K, k Direct and cross-coupled stiffness coefficients [F/L]

K^*, k^* Non-dimensional direct and cross-coupled stiffness coefficients

K_{eff} Effective stiffness coefficient [F/L]

K_{eff}^* Non-dimensional effective stiffness coefficient

L Axial length of the seal [L]

$\dot{m}$ Mass flow rate of gas [M/T]

m_r Blasius index for rotor

m_s Blasius index for stator

M Inertia coefficient [M]

n number of samples

n_r Blasius coefficient for rotor

n_s Blasius coefficient for stator

P Pressure [F/L^2]

p_1 Perturbation of non-dimensional pressure

P_i Inlet pressure [F/L^2]

P_e Exit pressure [F/L^2]

R Length along radial clearance from rotor to stator [L]

R_c Specific Gas Constant of Air [L^2/t^2* T]

Re Reynolds number

$Re[]$ Real part

t Time [t]

T_I Inlet Temperature [T]

U Average gas velocity in seal circumferencial direction [L/t]

V Average gas velocity in seal radial direction into honeycomb cell [L/t]

W Average gas velocity in seal axial direction [L/t]

x, y Relative displacement between stator and rotor [L]

$\dot{x}, \dot{y}$ Relative velocity between stator and rotor [L/t]

$\ddot{x}, \ddot{y}$ Relative acceleration between stator and rotor [L/t^2]

$\bar{y}$ Sample average

y_i Sample value

Z Length along seal axis [L]

Greek

ϕ Flow coefficient [-]

μ Dynamic Viscosity [F*t/L^2]

Θ Angle around seal annulus

ρ Gas density [M/L^3]

σ Standard deviation

τ_r Rotor wall shear stress [F/L^2]

τ_s Stator wall shear stress [F/L^2]

ω Rotor rotational frequency [1/t]

Ω Rotor precession frequency [1/t]

1   INTRODUCTION

The basic operating principle of a turbo machine is simple: convert the enthalpy of a fluid into the kinetic energy of a rotating shaft, or rotor. This rotating shaft, thus, has the ability to do work on, or produce power for, another system. Examples can range from wind and water mills, to gas turbines, to large steam turbines used to produce electricity or power large ships. Of course, turbomachinery can operate on the reverse principle; whereby, the mechanical energy of a rotating shaft can be used to put enthalpy into a fluid. An example of this would be a pump or gas compressor.

The success of a turbo machine leans primarily on its tremendous power output given its weight and size. And, as one might expect, there is a continual demand for even more power from these devices. One significant way to satisfy this demand is to raise the operating speed of the rotor. By doing so, the principles of rotordynamics become increasingly more significant in the engineering of these devices. Since the 1950's, particular interest in the study of rotordynamics has been placed on bearings, which support a rotor, and seals, which control fluid leakage. It has been determined that these two components can be both the cause and the cure of many rotordynamic instability problems.

1.1   Honeycomb Seals

Annular seals used in turbomachinery are conventionally non-contacting and stationary while the rotor spins within its inner diameter. The clearance between the seal and rotor is typically larger than that of a bearing, and normally has a clearance-to-radius

---

This thesis follows the style and format of the *ASME Journal of Engineering for Gas Turbines and Power.*

ratio on the order of 0.003. The primary function of the seal is to impede leakage between compression stages and at the balance piston, as shown in Figure 1 below.

Interstage Seal — Impeller Eye Seal — Balance Piston Seal
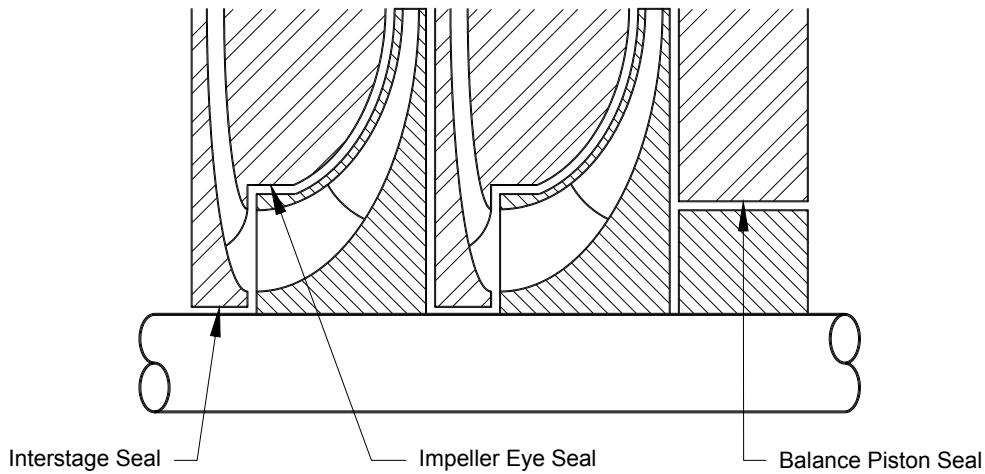
Figure 1: Annular Seal in a Turbomachine

One type of seal that has shown promise in increasing the performance of turbomachinery is the honeycomb annular seal, shown in Figure 2. It can be seen that the inner diameter of this type of seal consists of many hexagonal, or "honeycomb", pockets, thus giving its name. Childs et al. (1989) have shown that alteration of the width and depth of these pockets, or cells, can change the rotordynamic characteristics of the seal.
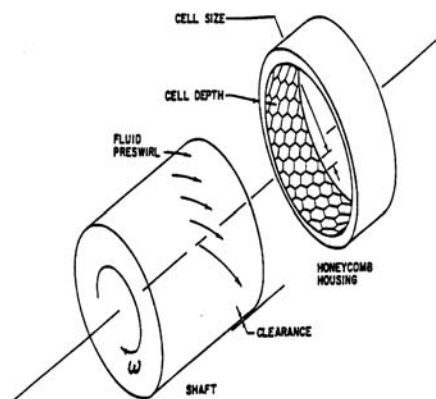
Figure 2: Honeycomb Annular Seal

The honeycomb seal was originally introduced in the 1960's as a replacement for aluminum labyrinth seals, which were being consumed by process fluids. It turned out that this type of seal had less leakage than a typical "see-through" labyrinth seal, and also was able to provide stability to otherwise unstable systems. For example, Childs and Moyer (1985) used honeycomb seals to eliminate synchronous and subsynchronous instabilities experienced by the high-pressure oxygen turbopump on the Space Shuttle main engine. Also, Zeidan, Perez, and Stephenson (1993) replaced labyrinth seals in two gas compressors with honeycomb seals, and were able to eliminate the previously experienced rotordynamic instabilities. A third example is by Armstrong and Perricone (1996), who replaced labyrinth seals with honeycomb seals in a steam turbine to reduce subsynchronous whirling.

Analysis and testing of honeycomb seals by Childs, Elrod, and Hale (1989) has shown that, for a seal length of greater than 51 mm (2.0 inches), they are superior in dynamic performance and leakage control, given the same radial clearance, to labyrinth and smooth-bore seals of similar dimensions. Particularly, honeycomb seals show significantly higher direct stiffness (K) and higher direct damping (C) than labyrinth seals, and lower cross-coupled stiffness (k) than smooth-bore seals. This can be particularly significant at the balance piston seal of a compressor, where the seal is typically longer in length. Many compressors are of the "back-to-back" type, as seen in Figure 3, in which the balance piston seal is located near the center of the machine. At this location, the balance piston can have a significant effect on the stability of the machine as the rotor takes its first bending mode shape, in which the highest oscillation amplitude and velocity occur at the rotor center.
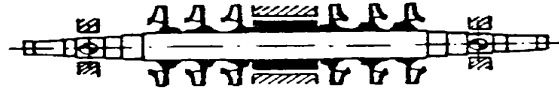
Figure 3: "Back-to-Back" Type Compressor

Added rotor stability from a seal is a direct consequence of the magnitude of its direct damping (C) and cross-coupled stiffness (k), and can be quantified as the effective damping as follows,

$$C_{eff} = C - k/\Omega \qquad (1)$$

where Ω is the precessional frequency of the rotor. Cross-coupled stiffness produces a destabilizing effect caused by fluid rotation within the seal. It is characterized by a force in one direction being proportional to a displacement in an orthogonal direction as illustrated in Figure 4 below:
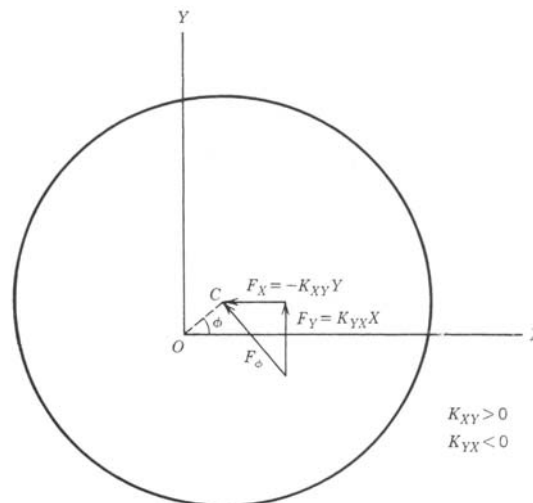
Figure 4: Cross-coupled Stiffness Representation on a Deflected Rotor Disk (from Vance, 1988)

A negative value of C_{eff} in Equation 1 indicates that k has become dominant and that the seal has become destabilizing. This could be detrimental if Ω is in the vicinity of the running speed of the machine.

Though labyrinth seals tend to produce lower values for cross-coupled stiffness (k), this gain in stability is insignificant compared to the much higher values of direct damping (C), obtained by the honeycomb seals. The effective damping of smooth-bore seals tends to be very dependent on rotor speed and inlet preswirl of the fluid.

1.2   Objectives of Work

Dawson (2000) showed that, for no inlet preswirl into the seal, a smooth-bore seal has much better damping capabilities (higher C_{eff}) than the particular honeycomb seal tested for this paper. However, Childs et al. (1989), as well as Yu and Childs (1998), have shown experimentally that the cross-coupled stiffness of a honeycomb seal similar to Dawson's increased about two-fold over the preswirl range tested, while a smooth-bore seal of similar dimensions increased more than six-fold over the same range. If a honeycomb seal is operating in a dirty environment, its cells may be susceptible to become clogged, thus causing it to perform as a smooth-bore seal. So, the purpose of this thesis is two-fold:

1.) Experimentally determine the leakage and the dynamic coefficients, such as effective stiffness and damping, of a honeycomb seal and a smooth-bore seal under varying inlet preswirl levels. Results for the two seals will then be compared under similar conditions to determine how much the performance of the honeycomb seal will degrade under inlet preswirl. The two seals are of similar

dimensions to facilitate comparison. Target inlet pressure for all tests is 70.0 bar-a. The specific honeycomb seal to be tested has a cell width of 0.79 mm (1/32") and cell depth of 3.2 mm (0.125") and is shown below in Figure 5.

2.) Compare measured leakage and dynamic coefficient values for each seal with that predicted by a new, two-control volume theory by Kleynhans and Childs (1997), over a precessional frequency range of 20-300 Hz.

1.3   Test Matrix

The targeted test matrix for each seal consists of tests under 27 different operating conditions, which are given as follows:

- three shaft speeds: 10,200 rpm, 15,200 rpm and 20,200 rpm;

- three backpressures: 15%, 35% and 50% of inlet pressure (70.0 bar-a) to the seal;

- three inlet preswirl magnitudes: 0%, 30%, 60% of the surface velocity of the rotor at 15200 rpm.

For each test condition, the stator is simultaneously excited at frequencies spanning from 20 to 300 Hz. The inlet pressure (70.0 bar-a) had to be reduced in some of cases in order to lower the magnitude of the cross-coupled stiffness, and thus prevent destructive instabilities from occurring.
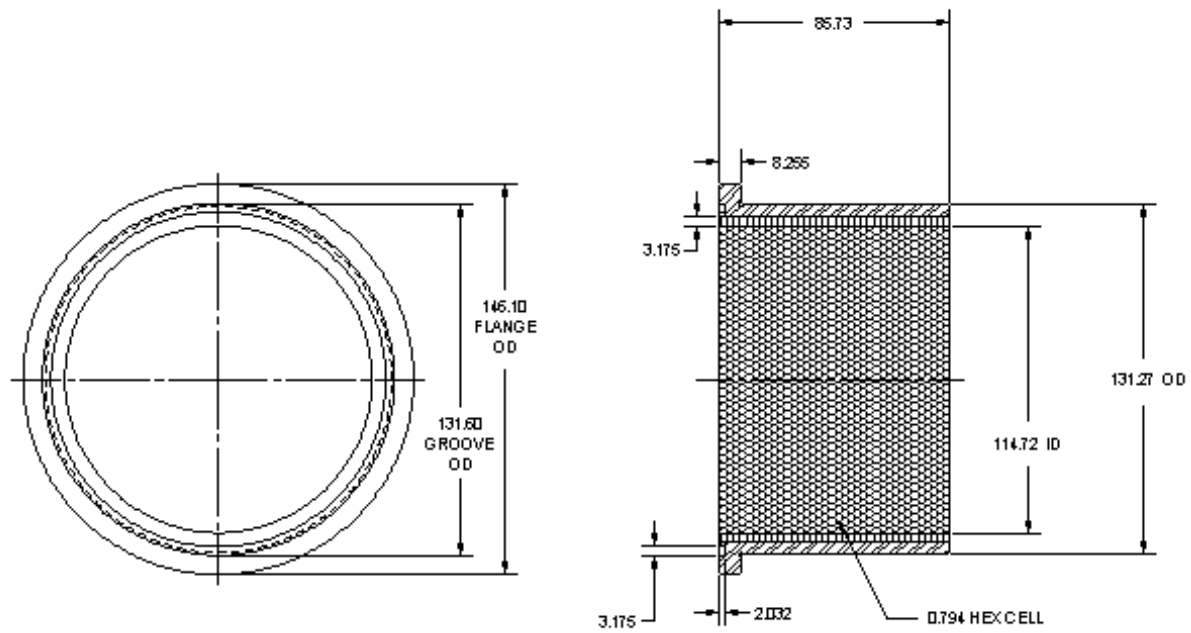
Figure 5: Honeycomb Damper Seal of 0.79 mm Cell Width and 3.2 mm Cell Depth

1.4   Literature Review

Lomakin (1958) first demonstrated that the pressure drop across a liquid annular seal induces a proportional hydrostatic centering force on the rotor. Black and Jenssen (1969, 1970) further investigated this pressure-induced hydraulic force and developed the initial analytical techniques for estimating the dynamic stiffness and damping coefficients for high-pressure liquid annular seals. Their theoretical predictions were based on a bulk-flow model of the fluid passing through the seal. Also, a circumferential bulk-flow velocity of $R\omega/2,$ where R is rotor radius and ω is the rotor speed, was assumed. This led to a significant prediction that the principal effect of fluid rotation within the seal is a reduction of effective damping forces by one-half as compared to the stiffening forces. Later, Allaire et al. (1976) extended Black and Jenssen's theory to account for large static eccentricities of the rotor.

In 1977, Fleming (1977) developed an analytical technique, which predicted that a convergent taper within the seal would significantly increase direct stiffness (K) for a given clearance-to-radius ratio. Subsequently, Fleming (1979) initiated the analytical techniques for compressible-fluid, or gas, seals. His analysis; however, neglected fluid rotation within the seal.

Experimental work by Wachter and Benckert (1980) showed that eliminating the circumferential flow between the seal and rotor would reduce the magnitude of the cross-coupled stiffness coefficient (k) in gas labyrinth seals, and thus increase stability of the rotor. They also concluded that honeycomb seals had larger k values than labyrinth seals. Von Pragenau (1982), however, proposed that a surface-roughened stator, such as a honeycomb seal, would reduce circumferential flow, and thus k, as compared to a

smooth-bore seal. Shortly after this, Childs (1983a, 1983b) began to build on Black and Jenssen's earlier analytical work by including the effects of general preswirl at the seal inlet, as well as, previously neglected fluid inertia terms. Childs' model utilized Hirs' (1973) turbulent bulk flow model in its development, as opposed to various 'ad hoc' governing equations used by Black and Jenssen. Nelson (1984, 1985) followed with a similar analysis for compressible-flow seals.

Childs and Kim (1986) tested a number of liquid hole-pattern seal configurations, which confirmed Von Pragenau's prediction of a reduction in cross-coupled stiffness, and showed higher values of C_{eff} than a smooth seal tested under similar conditions. Childs, Elrod, and Hale (1989) conducted the first dynamic tests for honeycomb seals, in which the rotor was shaken horizontally within the test seal over a frequency range of 30 to 75 Hz. This allowed not only the measurement of the stiffness coefficients (K and k), but damping (C and c) also. Their results agreed with Wachter and Benckert's claim that honeycomb seals produce a higher destabilizing cross-coupled stiffness (k) than labyrinth seals. This difference; however, was marginal in comparison with the significantly higher values of C produced by the honeycomb seals.

Comparison of Nelson's theory for gas seals with experimental results showed an over prediction of k and poor prediction of K and C. So, Elrod, Childs, and Nelson (1990) investigated a new, empirical friction factor model in the analysis. Results showed improvement in the prediction of k; however, K and C predictions remained poor in comparison with experimental results. Because of this, Ha and Childs (1992) proposed modeling the fluid within the seal in a two-control-volume fashion. Subsequently, Kleynhans and Childs (1997) developed a new analytical technique for determining

dynamic coefficients of the seal based on the two-control-volume model. This analysis used a conventional control volume for the through flow of the fluid and a "capacitance-accumulator" model for the individual honeycomb cell. The control volume for the honeycomb cell drops the acoustic velocity of the main fluid flow to within the frequency range of interest in rotordynamics, thus causing the dynamic coefficients to become frequency dependent. Testing over a large frequency range (40 to 230 Hz) by Dawson (2000) and Holt (2001) showed this frequency dependence, as well as, a marked improvement in the correlation between experimental results and this new theory.

1.5   Small-Motion Model for Gas Seal Forces

Nelson's theory for compressible flow through an annular gas seal is based on a bulk-flow model consisting of,

- a compressible flow continuity equation

- an axial-momentum equation

- a circumferential-momentum equation

- an energy equation

- a perfect-gas equation of state

The energy equation was later omitted after experimentation showed the flow through the seal to be virtually isothermal. All of these equations, for both the honeycomb and smooth-bore seal, are given in Appendix A. The friction factor f used for wall shear stress was determined using the Blasius model, and is also given in Appendix A.

Following Kleynhans and Childs' (1997) application of perturbation-of-variables and separation-of-variables, the remaining equations can be reduced to ordinary, linear

differential equations, with non-dimensional pressure p, circumferential velocity u, and axial velocity w as the dependent variables, and non-dimensional axial location z as the only dependent variable. Numerical integration yields a solution for pressure p, which is then integrated for discrete frequencies over the length of the seal to obtain the radial and tangential impedances:

$$I_r(\Omega) = -\pi \int_0^1 \mathrm{Re}[p_1(\Omega)]dz \qquad (2)$$

$$I_\theta(\Omega) = -\pi \int_0^1 \mathrm{Im}[p_1(\Omega)]dz$$

It was originally assumed that the dynamic characteristics of the honeycomb seal were independent of the precessional frequency of the rotor within the seal. Thus, a frequency-independent, force-motion model was used, as given below,

$$-\begin{Bmatrix} F_x \\ F_y \end{Bmatrix} = \begin{bmatrix} K & k \\ -k & K \end{bmatrix} \begin{Bmatrix} \Delta x \\ \Delta y \end{Bmatrix} + \begin{bmatrix} C & c \\ -c & C \end{bmatrix} \begin{Bmatrix} \Delta \dot{x} \\ \Delta \dot{y} \end{Bmatrix} + M \begin{Bmatrix} \Delta \ddot{x} \\ \Delta \ddot{y} \end{Bmatrix} \qquad (3)$$

The coefficients can be backed out by curve fitting to I_r and I_θ versus precessional frequency as follows,

$$I_r(\Omega) = (K - M\Omega^2) + c\Omega$$
$$\qquad (4)$$
$$I_\theta(\Omega) = k - C\Omega$$

Assuming $\Delta x \cong \Delta y = A$, then the resulting forces on the rotor can be expressed as,

$$F_r = [(K - M\Omega^2) + c\Omega]A$$
$$\qquad (5)$$
$$F_\theta = [k - C\Omega]A$$

which are illustrated below in Figure 6:
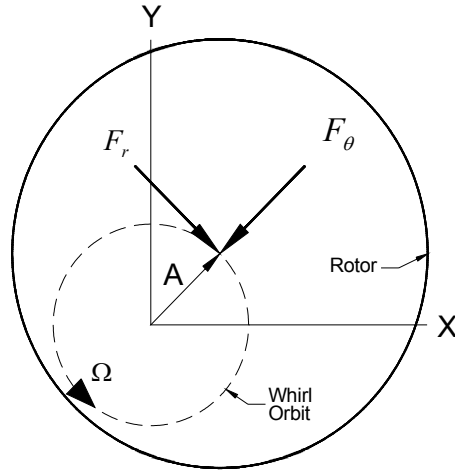
Figure 6: Whirling Rotor with Induced Tangential and Circumferential Forces

Nelson's model predicts well for smooth-bore seals. However, for damper seals, such as honeycomb and hole-pattern, in which the cell depth is significantly larger than the seal-rotor clearance, the frequency-independent model begins to break down as shown by Ha and Childs (1992). So, the following general transfer function model is presently used for damper seals:

$$-\begin{Bmatrix} F_x(s) \\ F_y(s) \end{Bmatrix} = \begin{bmatrix} D & E \\ -E & D \end{bmatrix} \begin{Bmatrix} \Delta x(s) \\ \Delta y(s) \end{Bmatrix} \tag{6}$$

Using the two-control-volume model previously discussed to find I_r and I_θ, the values of D and E can be backed out from the following equations:

$$I_r(\Omega) = \text{Re}[D] + \text{Im}[E] \tag{7}$$

$$I_\theta(\Omega) = \text{Re}[E] - \text{Im}[D]$$

From here, the dynamic coefficients are found from the definitions below:

$$D = K(\Omega) + i\Omega C(\Omega) \tag{8}$$

$$E = k(\Omega) + i\Omega c(\Omega)$$

And the effective stiffness and damping are given as,

$$K_{eff} = K(\Omega) + \Omega c(\Omega) \tag{9}$$

$$C_{eff} = C(\Omega) - k(\Omega) /\Omega \tag{10}$$

1.6   Test Equipment

The Annular Gas Seal Test Stand (AGSTS) is derived from an existing Hybrid Hydrostatic Bearing Test Stand. A diagram of the test stand is shown below in Figure 7.
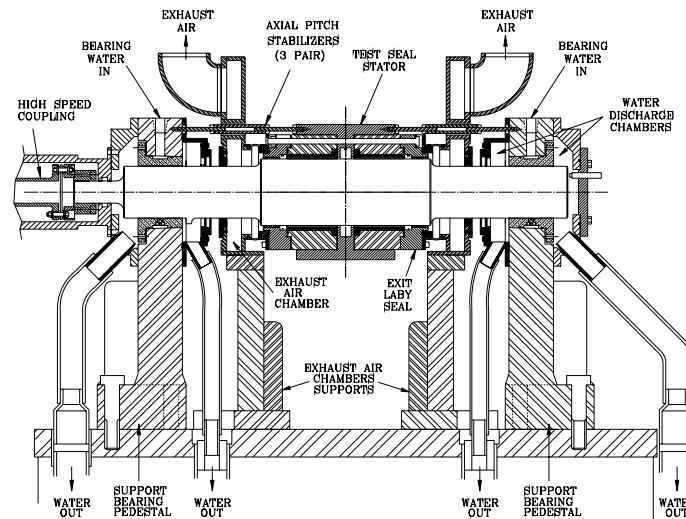
Figure 7: Annular Gas Seal Test Stand

The rotor is supported by two hydrostatic bearings, which provide very high stiffness in comparison with that developed by the seals. The test stator is supported independently and between the hydrostatic bearing pedestals by two hydraulic shakers. The shakers are oriented orthogonal to one another, representing the X and Y directions. They are also both oriented 45° from vertical, as shown in Section A-A of Figure 8 below, so that gravity loads are shared symmetrically. The shakers, which are mounted on two large I-beam supports, excite the stator with a pseudo-random waveform to obtain

the rotordynamic coefficients of the seals. The pitch and yaw of the stator is controlled by six axial pitch stabilizers, configured in triangular arrays on both sides of the stator. These pitch stabilizers ensure that the stator will remain coaxial and nominally centered with respect to the rotor during excitation.

The stator is designed with an inlet annulus located at its center and an exit annulus on each end. Behind each exit annulus is a labyrinth seal, which provides backpressure at the exit. This backpressure can be adjusted via two vent lines at each exit annulus as shown in Section B-B of Figure 8.
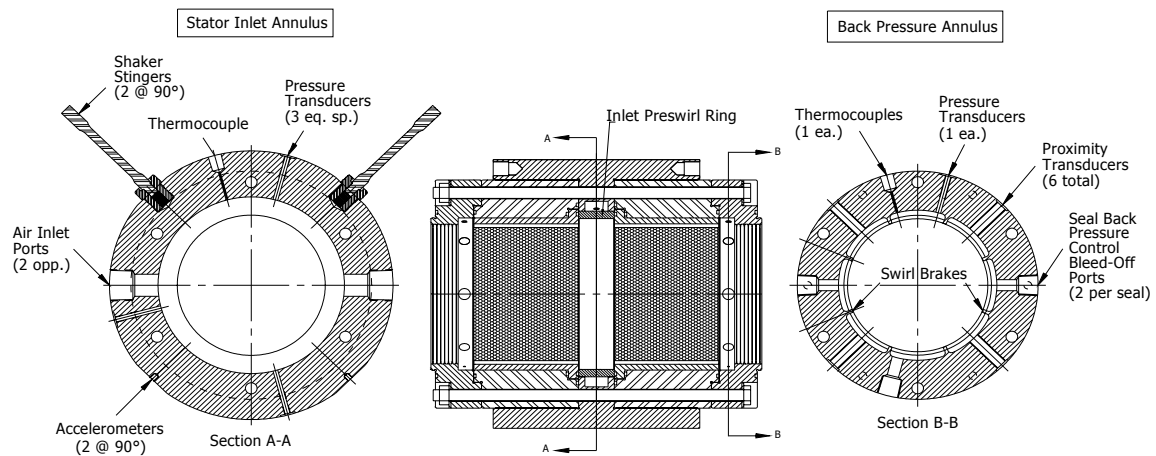
Figure 8: Stator Test Section and Instrumentation

The supply air is fed into the inlet annulus, with varying levels of preswirl via compression fitted swirl rings, shown in Figure 8. Each of three preswirl rings consists of 32 equally spaced holes, except where the inlet air enters the stator. At these two points, shown in Section A-A of Figure 8, there are no holes so that air is forced around the upstream side of the ring and evenly distributed through the holes. The two "non-zero preswirl" rings have their holes drilled at 60° from radial. Higher preswirl is obtained by

smaller diameter holes, which increases fluid velocity. Testing showed very little pressure loss across the rings.

1.7   Waveform Generation

For each set of seals, a specific pseudo-random waveform is generated. This is done through a sequential process of shaking the stator with the two seals at an individual frequency in order to find the output voltage necessary to give a shaking amplitude of 0.025 mm (1 mil) peak-to-peak. The range of frequencies tested is 20-300 Hz, so the process is started at 20 Hz and continued in 40 Hz increments until 300 Hz reached. Then a code is run that interpolates between the 40 Hz incremental values to give discrete amplitudes at increments of 10 Hz. Finally, an optimized time trace is produced, which will be used to shake the stator and seals, by performing a reverse-FFT on these data.

1.8   Data Reduction

Tests are performed in only one direction at a time, X direction followed by Y. Each test is comprised of 32, 0.1 second excitations. So, total test time is 3.2 seconds. As the stator and seals are shaken, data are recorded by the computer, measuring displacement, acceleration, and force in both the X and Y directions. A data reduction program then performs an FFT on these data in order to transform the time record to frequency domain. The reduced data are then used to back out the frequency response functions (FRF's) of the seal using Equation 11 below:

$$\begin{bmatrix} F_{xx} - Ma_{xx} & F_{yx} - Ma_{yx} \\ F_{xy} - Ma_{xy} & F_{yy} - Ma_{yy} \end{bmatrix} = \begin{bmatrix} H_{xx} & H_{xy} \\ H_{yx} & H_{yy} \end{bmatrix} \bullet \begin{bmatrix} XX & YX \\ XY & YY \end{bmatrix} \tag{11}$$

Once the FRF's are calculated, they are divided by two, since two seals are tested simultaneously. It can be seen that the inertial forces induced by the mass of the stator and seals is subtracted out, leaving only the force cause by the fluid-structure interaction between the gas and the seal.

The resulting FRF's are complex functions, and can be compared to theoretical predictions for the honeycomb seal as follows:

$$D(i\Omega)= H_{xx} = H_{yy}$$

$$E(i\Omega)= H_{xy} = -H_{yx}$$

(12)

The experimental effective stiffness and damping coefficients can then be found using Equations 9 and 10. For smooth-bore seals, however, the dynamic coefficients are frequency-independent. It should be noted that agreement between the X and Y were fairly poor and, therefore, $H_{xx} \neq H_{yy}$ and $H_{xy} \neq -H_{yx}$. In the past, experiments by Dawson (2000) and Holt (2001) on the same test rig have shown Equation 12 to be relatively true. However, during testing for this paper, the proximity probe measuring displacement for the Y direction was discovered to be faulty and could not be replaced in a timely manner. So, only data for the X-direction are presented in this paper for the sake of accuracy.

The same testing procedure is carried out with no test seals to create a "baseline". FRF's obtained in this test are subtracted from those measured with the test seals. This step eliminates the influence of the pitch stabilizers, backpressure labyrinth seals, etc., so that only the FRF's of the test seals themselves should be left at this point.

As stated earlier, 32 excitations are performed in each test. For each excitation, the FRF's obtained are averaged over the 32 excitations. This is one of two methods used to try to account for random noise in a test. The other method used is the application of

the power spectral density function, which consists of the auto and cross-spectral density functions. In this application, all of the measured parameters; force, acceleration, and displacement, are multiplied by the complex conjugate of the input excitation when in the frequency domain. This is discussed in detail by Rouvas (1993).

1.9 Uncertainty Analysis

For each re-assembly of the test rig, or equivalently, for each of the three different preswirl rings, 10 tests were run at a single operation condition (10200 rpm and 50% backpressure) to obtain data for uncertainty analysis. These tests were reduced as described earlier, and the mean impedance value at each frequency was calculated along with a standard deviation using the following classical equation for a Gaussian distribution:

$$\sigma = \left[\frac{1}{n-1} \sum_{i=1}^{n} (y_i - \bar{y})^2 \right]^{1/2} \tag{14}$$

where,

$$\bar{y} = \frac{1}{n} \sum_{i=1}^{n} y_i \tag{15}$$

Reference to the Nomenclature at the beginning of the report will help in understanding these equations. The standard deviations were then calculated, according to their respective frequency, to form error bars around the impedance points of the 6 nominal tests. The error bars represent a 68% chance that, if a test was repeated, the given impedance value would lie within that range.

2   EXPERIMENTAL RESULTS

This section gives experimental results for the dynamic coefficients of each seal. Section 2.1 discusses the effects of preswirl on each dynamic coefficient for the honeycomb seal. Section 2.2, similarly discusses the effects of preswirl on the smooth seal. Finally, Section 2.3 makes a comparison of the two seals for each level of preswirl.

As mentioned in discussing the test matrix in Section 1.3, the target inlet pressure of 70.0 bar-a was not obtainable for the entire test matrix of each seal. This was especially true for the smooth seals. Therefore, the measured dynamic coefficients were normalized in order to compare them on a common basis by using the clearance between the rotor and stator and the nominal force on the stator. An example of this normalization is given below for direct stiffness in Equation 16.

$$K^* = \frac{K \cdot C_r}{F_o} = K\left(\frac{C_r}{\Delta P \cdot D_{in} \cdot L}\right) \tag{16}$$

The asterisk after the coefficient represents that it has been normalized. The remaining normalized dynamic coefficients will be identified in a like manner with the asterisk. Note that the normalized stiffness coefficients, such as K^* and k*, are non-dimensional, however, the normalized damping coefficients, such as C^* and c^*, have units of seconds. This is a consequence of the normalizing process. However, the purpose of creating a common basis for comparison is still served.

2.1   Honeycomb Seals

A total of 27 test cases were conducted using the 0.79 mm (1/32") cell width honeycomb seal. The actual test conditions for each case are given in Table III of

Appendix B. The table shows that only 4 of the 27 test cases show an inlet pressure less than the target pressure of 70.0 bar-a as a result of system instability. Three of these four were under high preswirl conditions.

Figure 9 shows that there is very little change (<10%) in the magnitude of the measured direct stiffness, K^*, as the level of inlet air preswirl is increased. There is also no obvious pattern to the effects of increased preswirl. Though, measured data do show that K^* is highest for medium preswirl for excitation frequencies above 200 Hz. There is, however, a consistent drop of the peak magnitude of K^* by about 45% when comparing 15% backpressure to 50% backpressure for all levels of preswirl.

Figure 10 shows an evident sensitivity of the cross-coupled stiffness, k^*, to an increase in inlet preswirl. This is most apparent at the 10,200-rpm test speed, where there is, on average, a 37% increase in the values of k^* when comparing low and medium preswirl results; and a 50% increase when comparing medium and high preswirl conditions. As rotor speed is increased, results for low and medium preswirl begin to converge, showing medium preswirl to be, on average, only 6% higher at 20,200-rpm. High preswirl, however, still shows about a 38% increase, on average, over medium preswirl at 20,200-rpm. It can also be observed in the low shake frequency range that k^* shows a slight decrease in magnitude as backpressure is decreased.

Figure 11 demonstrates the insensitivity of direct damping C^* to inlet preswirl, showing no distinct pattern, and, on average, no more than 8% change in magnitude. For frequencies below 50 Hz, rotor speed has a noticeable effect on C^*, averaging about a 30% increase at 20,200-rpm versus 10,200-rpm.

Figure 12 presents measured data for the effective direct stiffness $K_{eff}*$, which takes into account the effect of cross-coupled damping, $c*$, on the direct stiffness, as illustrated by Equation 9. The sensitivity to preswirl seems to be slightly more pronounced than for direct stiffness, $K*$, but is still small. High inlet preswirl shows the lowest values in most cases, especially below 200 Hz. Medium preswirl begins to show the highest values for frequencies above about 250 Hz, similar to $K*$. Again, comparing 15% backpressure to 50% backpressure, there is a consistent drop of the peak magnitude of $K*$ by about 45% for all levels of preswirl. Note that $K_{eff}*$ begins to show negative values below 50Hz as rotor speed is increased.

Last, and perhaps most important in the context of this paper, Figure 13 compares the effective damping, $C_{eff}*$, for the different levels of preswirl. There is a definite decrease in the magnitude of $C_{eff}*$ for excitation frequencies from 20 to 200 Hz as the level of preswirl is increased. Above this frequency, low and medium preswirl begin to converge. High preswirl, however, consistently gives the smallest values of $C_{eff}*$ for the entire frequency range. Observing Figure 13, increased rotor speed tends to decrease $C_{eff}*$ for all preswirl levels. Looking at shake frequencies below 200 Hz for 10,200-rpm rotor speed, there is an average decrease of about 14% transitioning from low to medium preswirl, and about 25% transitioning from medium to high preswirl. Observing 20,200-rpm test cases, there is an average decrease of about 15% transitioning from low to medium preswirl, and about 19% transitioning from medium to high preswirl. So, the average change is similar for the two rotor speeds. However, the peak magnitude drops on average 38% for the 10,200-rpm test cases, compared to only 25% for the 20,200-rpm test cases when comparing high preswirl to low preswirl.

Figure 9: Experimental *K** Versus Excitation Frequency for Honeycomb Seals at Three Levels of Preswirl

Figure 10: Experimental *k** Versus Excitation Frequency for Honeycomb Seals at Three Levels of Preswirl
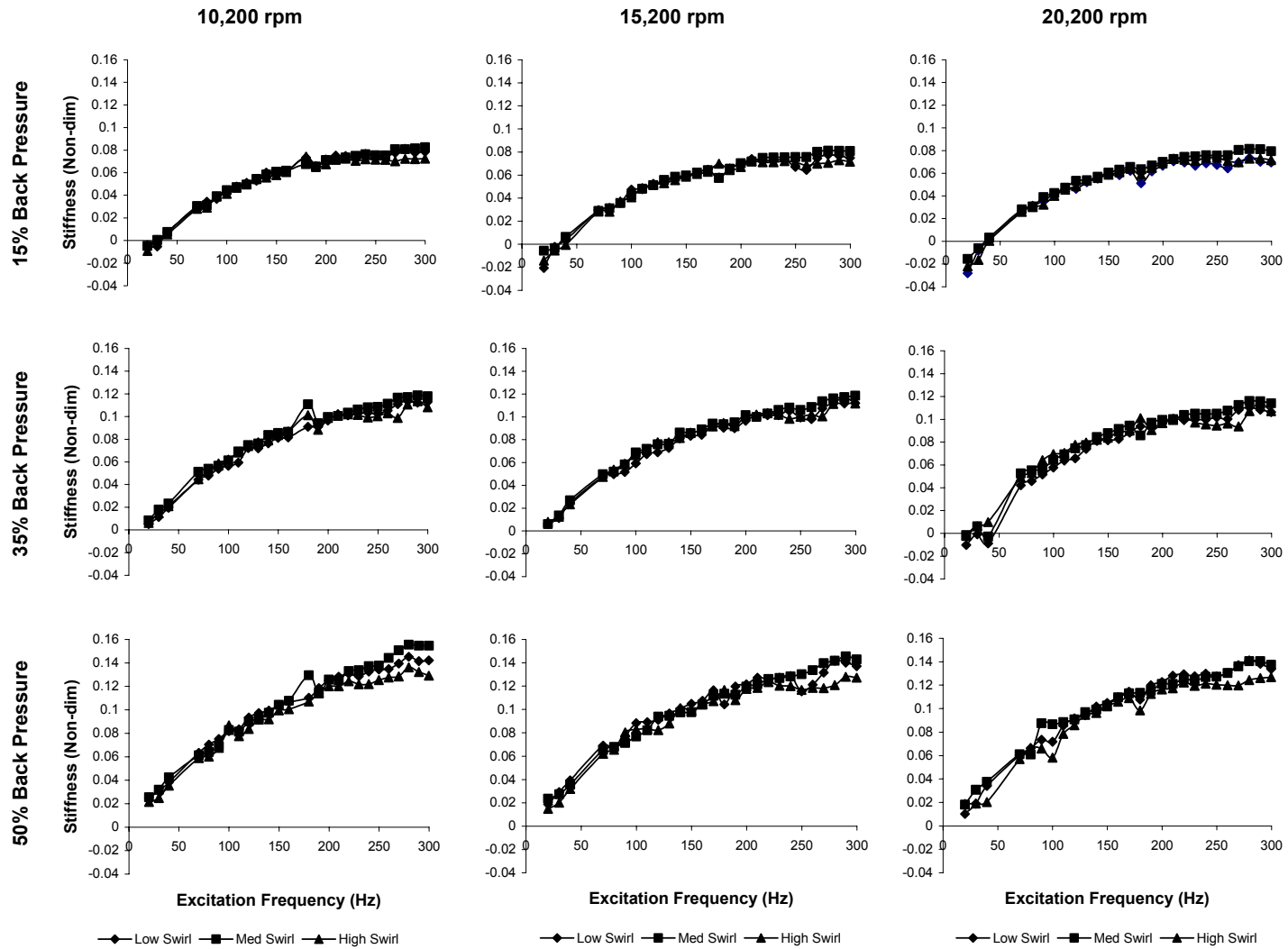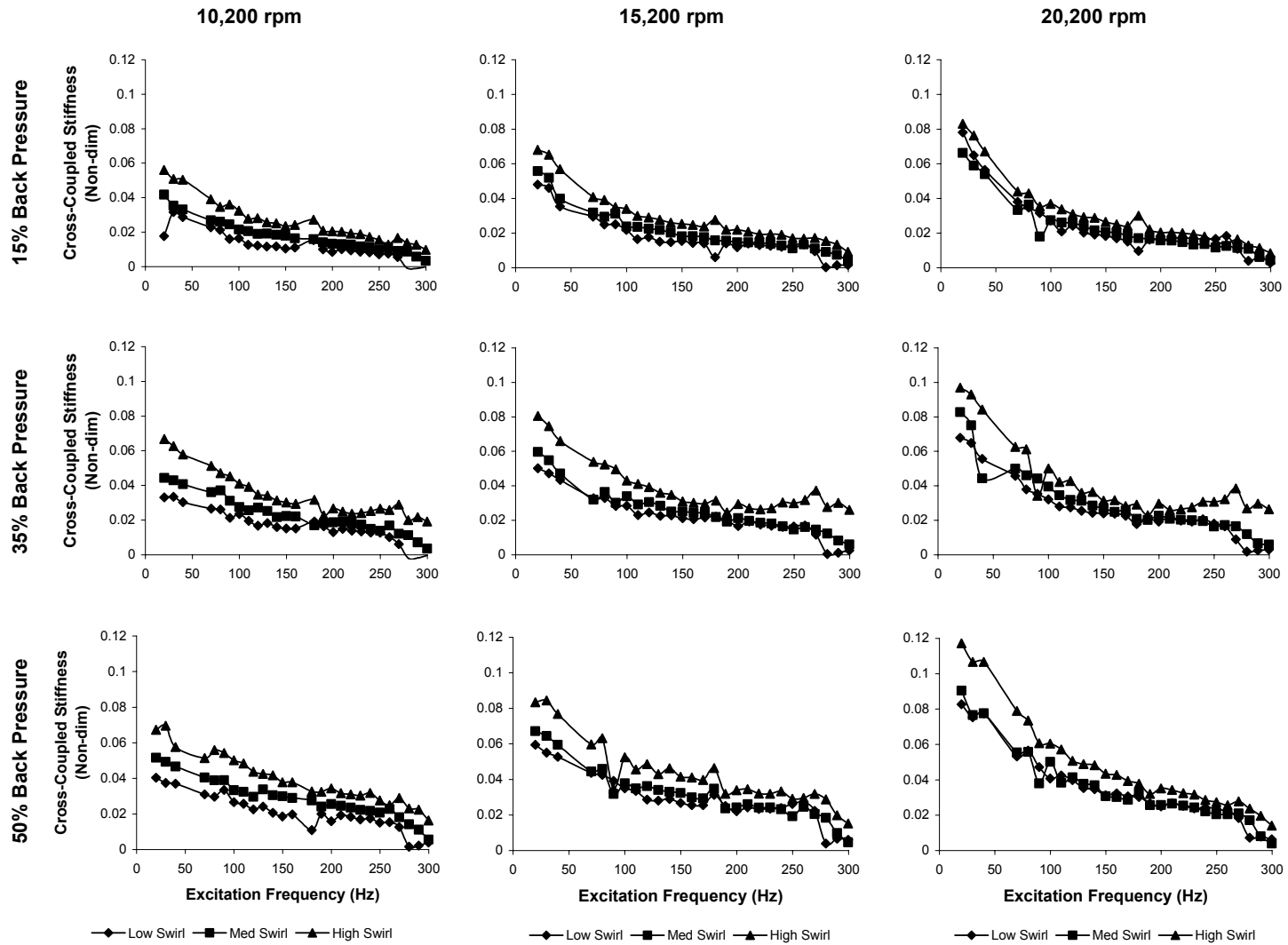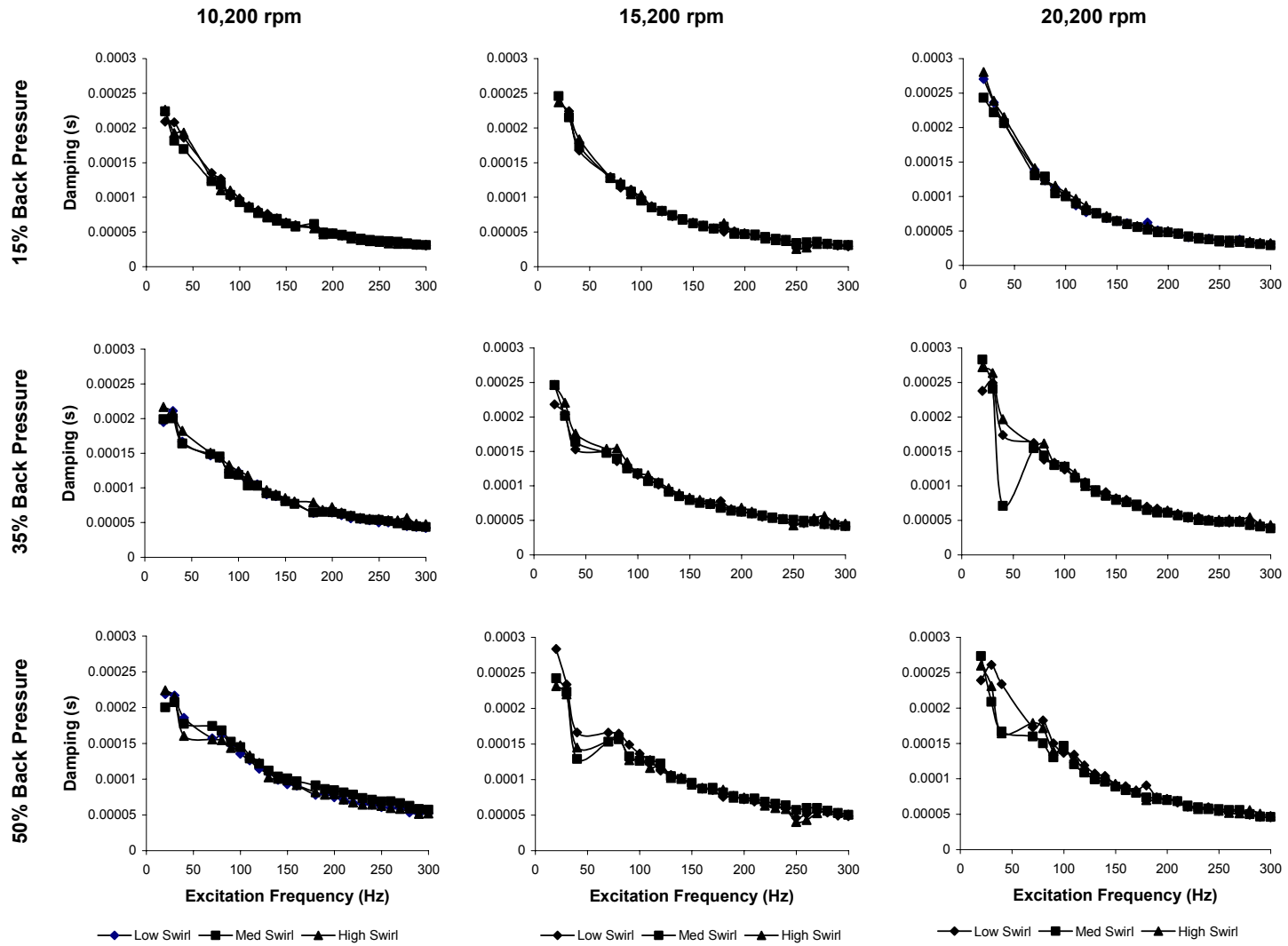
Figure 11: Experimental *C** Versus Excitation Frequency for Honeycomb Seals at Three Levels of Preswirl
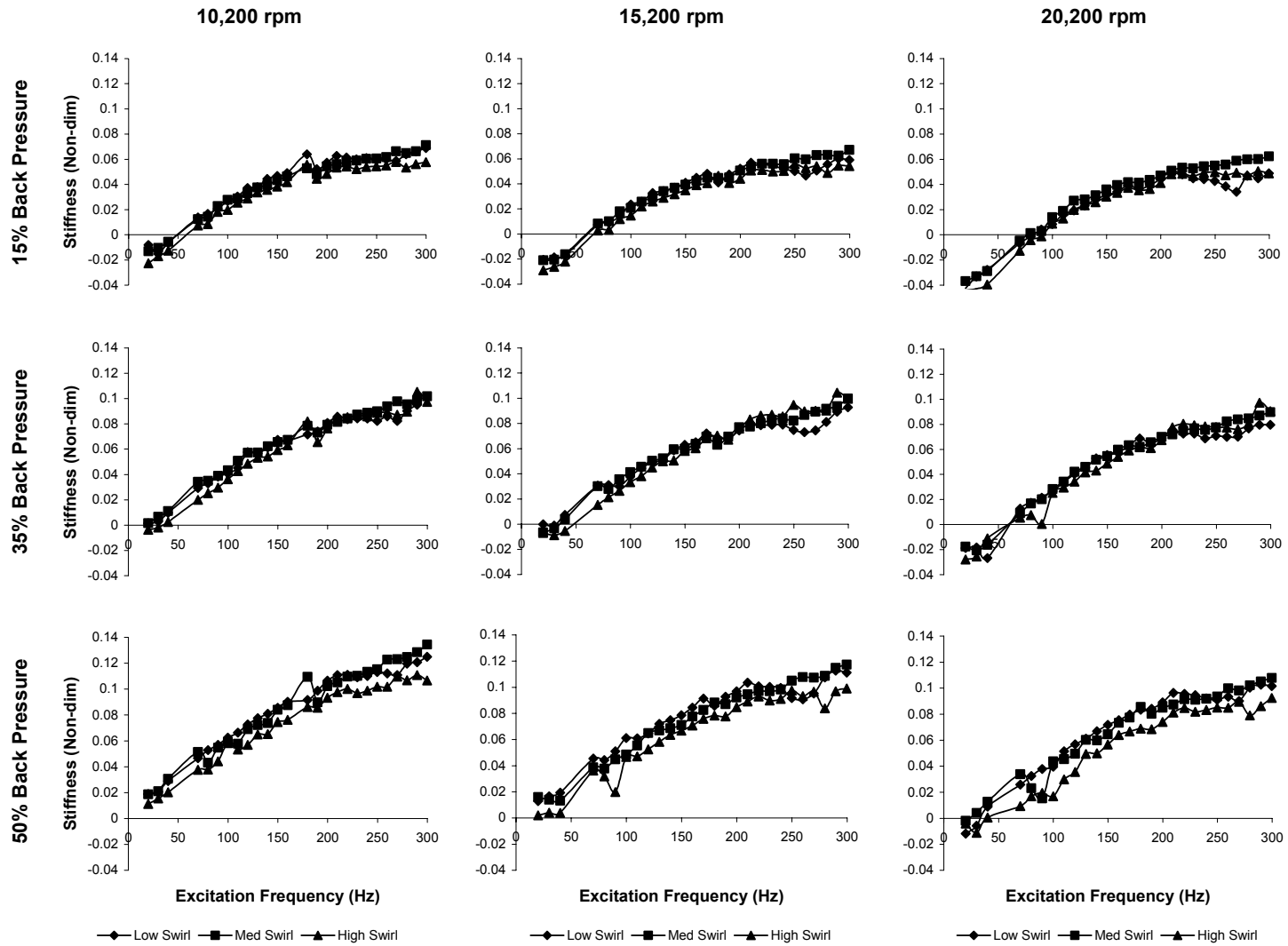
Figure 12: Experimental $K_{eff}*$ Versus Excitation Frequency for Honeycomb Seals at Three Levels of Preswirl
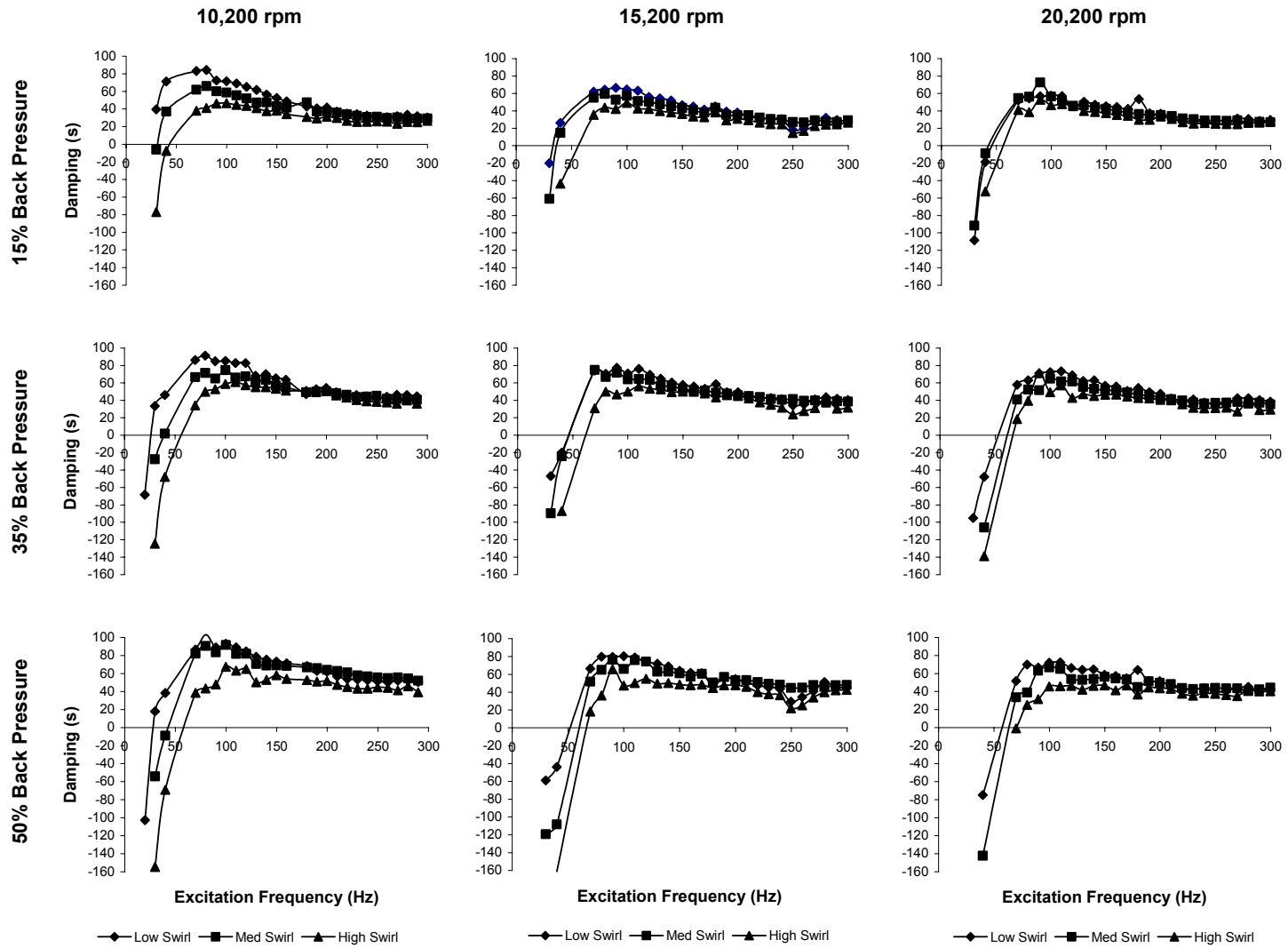
Figure 13: Experimental C_{eff}* Versus Excitation Frequency for Honeycomb Seals at Three Levels of Preswirl

2.2   Smooth-Bore Seal

A total of 12 test cases were conducted using the smooth-bore seal. The actual test conditions for each case are given in Table IV of Appendix B. Note that when the medium inlet preswirl ring was tested, the target inlet pressure of 70 bar-a could only be achieved for one test without the system going unstable. The high inlet preswirl ring could not be tested at all due to destructive instabilities encountered at inlet pressures as low as 14.78 bar-a (200psia). Also, due to a high mass flow rate through the smooth-bore seals, airflow choked near the 35% backpressure condition. This prevented testing at any lower backpressure since the mass flow rate would not increase beyond this point. Therefore, the 15% backpressure test condition was omitted for the smooth-bore seals.

It can be seen in Figure 14 that the magnitude of K^* is much less than that of the honeycomb seal. Thus, the scatter of the measured data is more pronounced. It is apparent, nevertheless, that preswirl has a significant influence on the direct stiffness of the smooth seals. Backpressure also shows a significant effect on K^*. Transitioning from low to medium preswirl shows an increase in direct stiffness of 103% on average for the 35% backpressure, and 28% on average for the 50% backpressure. The higher sensitivity to preswirl for 35% backpressure testing is due to the very small magnitudes of K^* at this backpressure.

It is very apparent that the cross-coupled stiffness, k^*, of the smooth seals is significantly more sensitive to preswirl than the honeycomb seals. The smooth seals are also much more sensitive to rotor speed for the same reason. This being the relative inability to mitigate the circumferencial airflow induced by both the inlet preswirl and the turning of the rotor. Observing Figure 15, the 10,200-rpm, 15,200-rpm, and 20,200-rpm

cases show an increase in k^* on average of 440%, 215% and 125%, respectively, when comparing medium with low preswirl. Note the decline in percent change of k^* with preswirl as rotor speed is increased. Since increased rotor speed creates increased circumferencial flow within the seal, the preswirl has less (though still a large) effect.

Figure 16 illustrates that, as with the honeycomb seal, preswirl has very little effect on the direct damping, C^*. Low and medium preswirl test cases show no more than a 5% difference, with no specific trend in the changes.

Figure 17 shows the effective stiffness, K_{eff}^*. Results are similar to those of K^*, with the cross-coupled damping term, c^*, adding little effect. As with K^*, sensitivity to preswirl is higher at 35% backpressure, showing a 103% increase in K_{eff}^*, on average, when comparing medium preswirl with low preswirl results. For the 50% backpressure condition, K_{eff}^* shows a 22% increase when comparing medium with low preswirl.

Figure 18 demonstrates how detrimental preswirl can be to the effective damping, C_{eff}^*, for the smooth seal. At low preswirl, it can be seen that C_{eff}^* has a cross-over point, or transition from negative to positive values, ranging from about 25 Hz to 70 Hz, depending on rotor speed. However, for medium preswirl testing, C_{eff}^* does not obtain a positive value until about 140 Hz, even at low rotor speed. This large shift in the C_{eff}^* curve with preswirl is due to the much larger measured values of k^* for medium preswirl than low preswirl. In the higher frequency range, such as 250 Hz to 300 Hz, where the two curves begin to level off, there is still about a 45% drop in the values of C_{eff}^* when comparing medium preswirl to low preswirl.

Figure 14: Experimental *K** Versus Excitation Frequency for Smooth-Bore Seals at Two Levels of Preswirl

Figure 15: Experimental *k** Versus Excitation Frequency for Smooth-Bore Seals at Two Levels of Preswirl

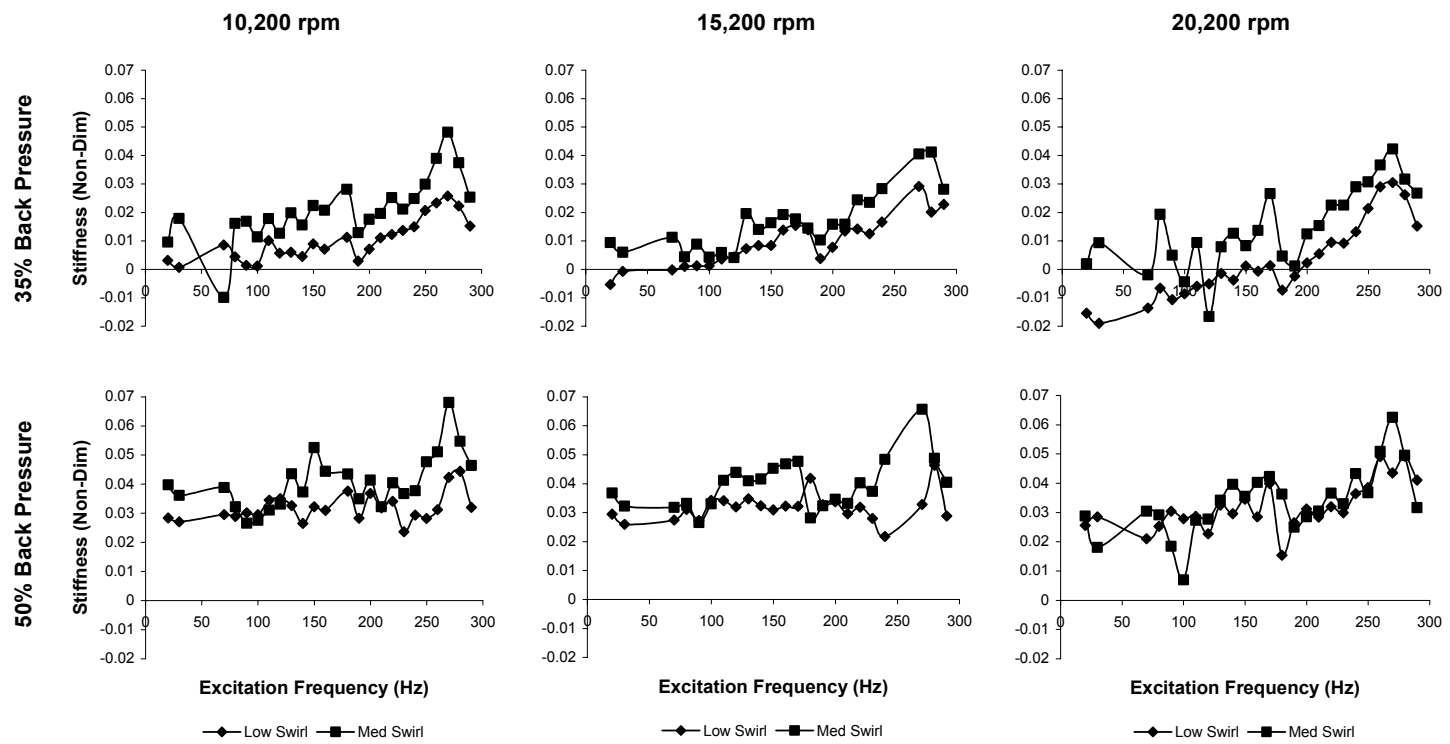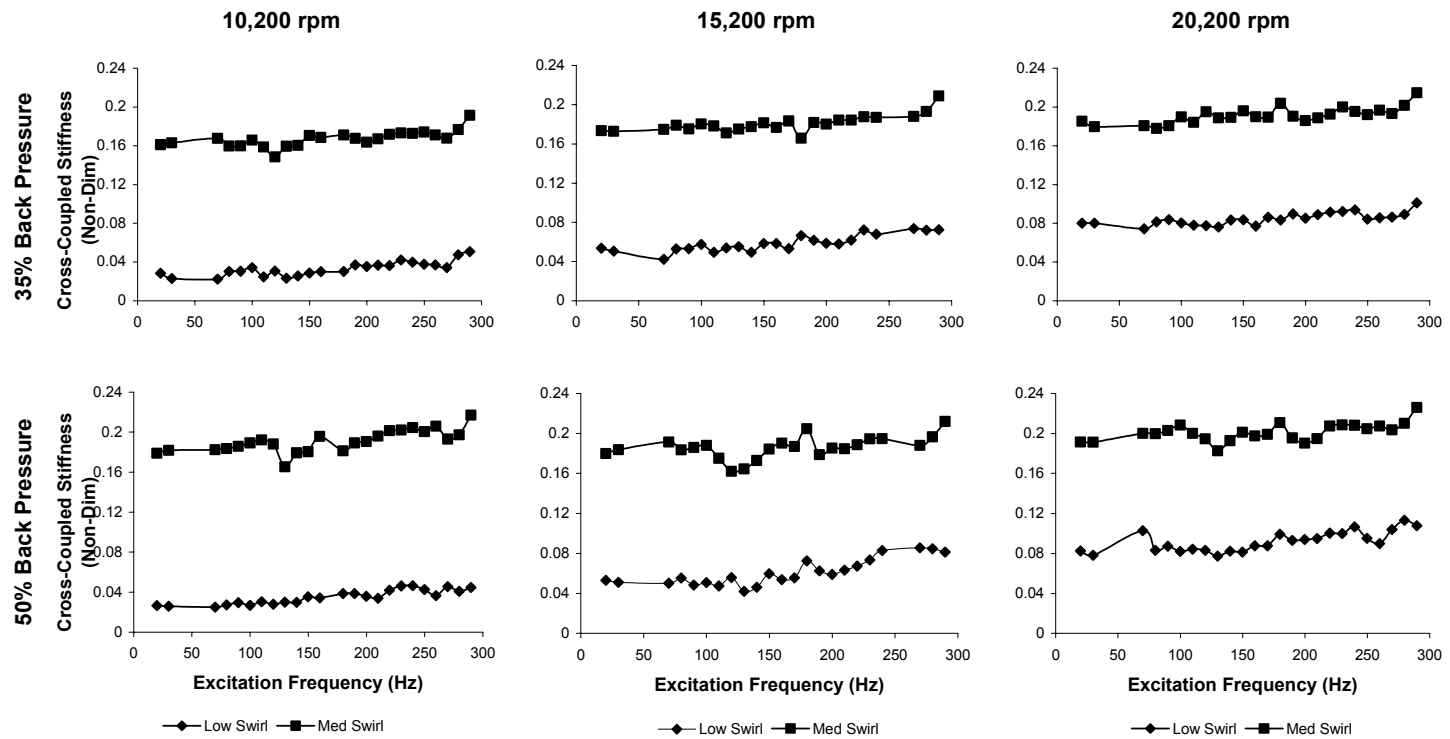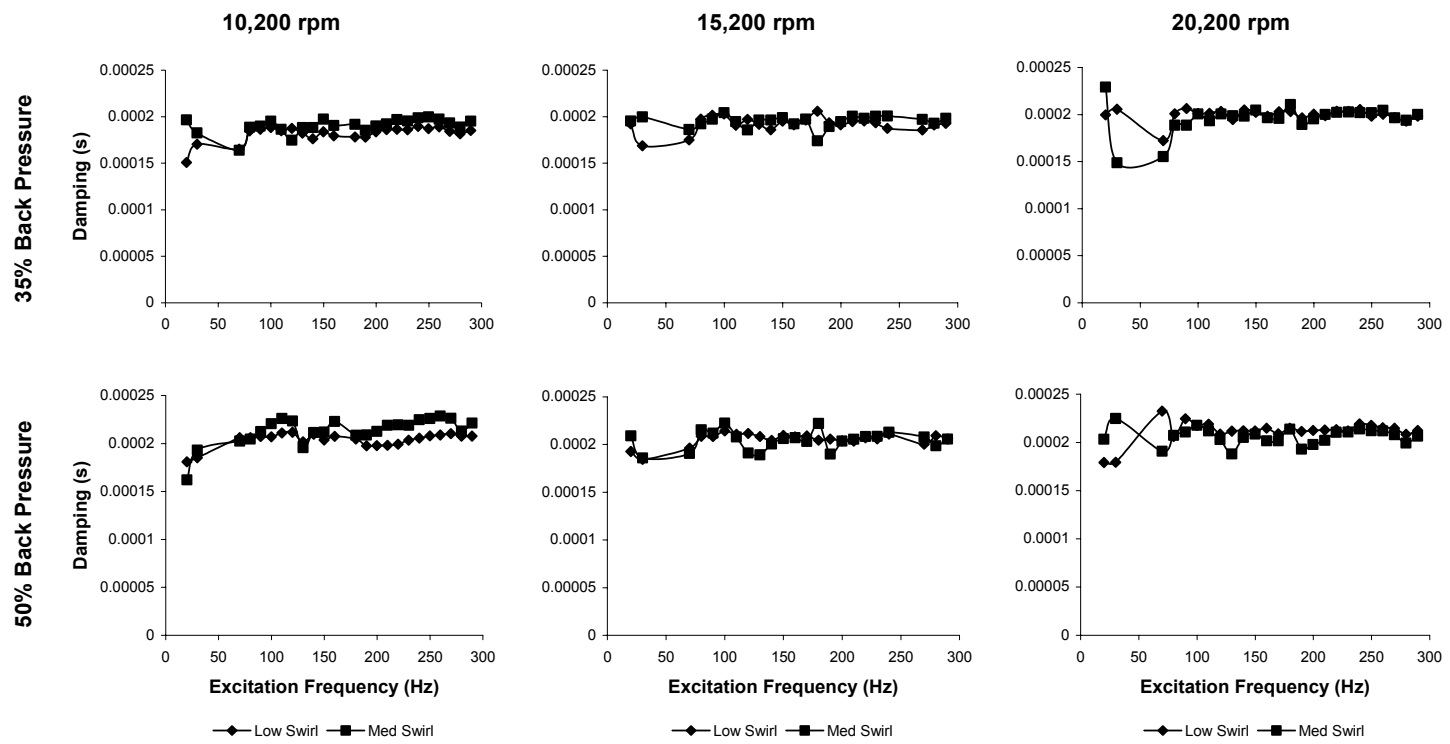**Figure 16: Experimental *C** Versus Excitation Frequency for Smooth-Bore Seals at Two Levels of Preswirl**
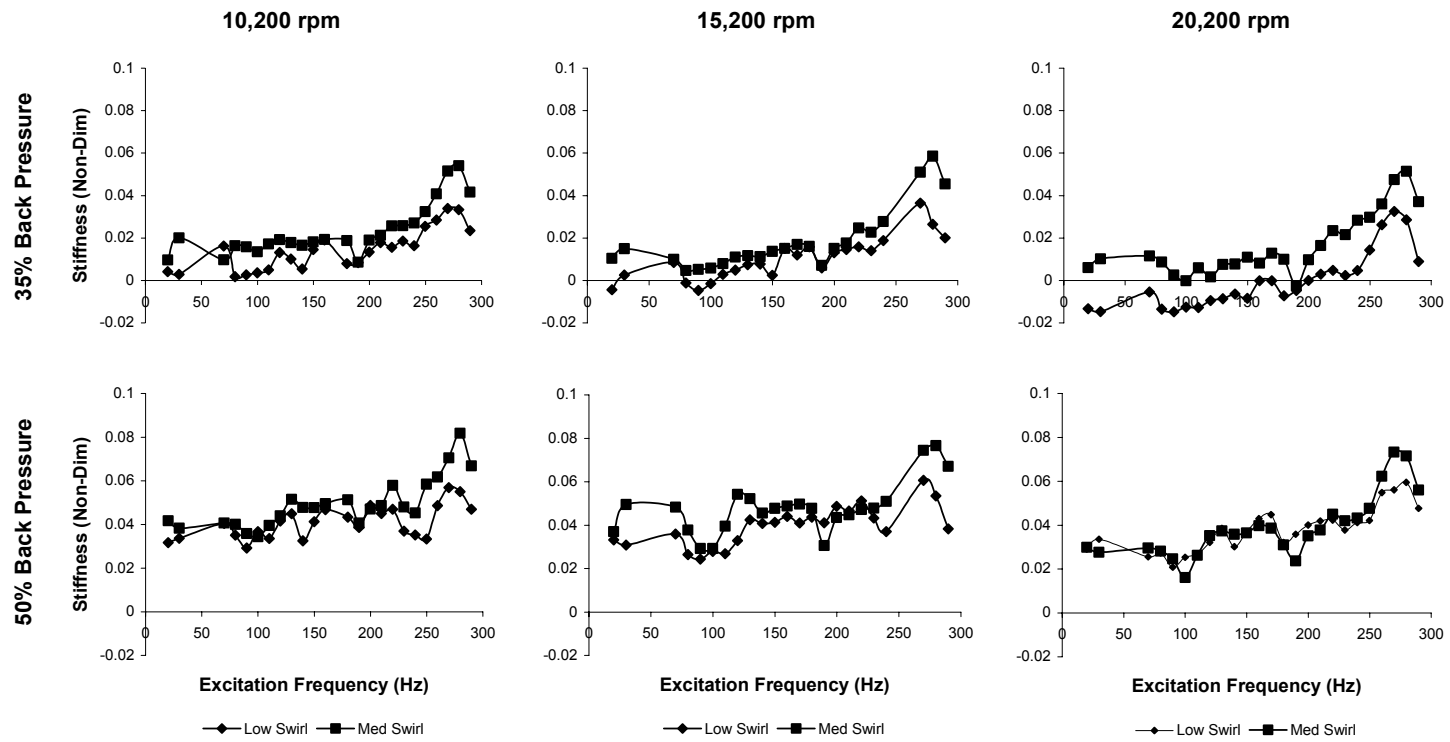
Figure 17: Experimental K_{eff}^{*} Versus Excitation Frequency for Smooth-Bore Seals at Two Levels of Preswirl
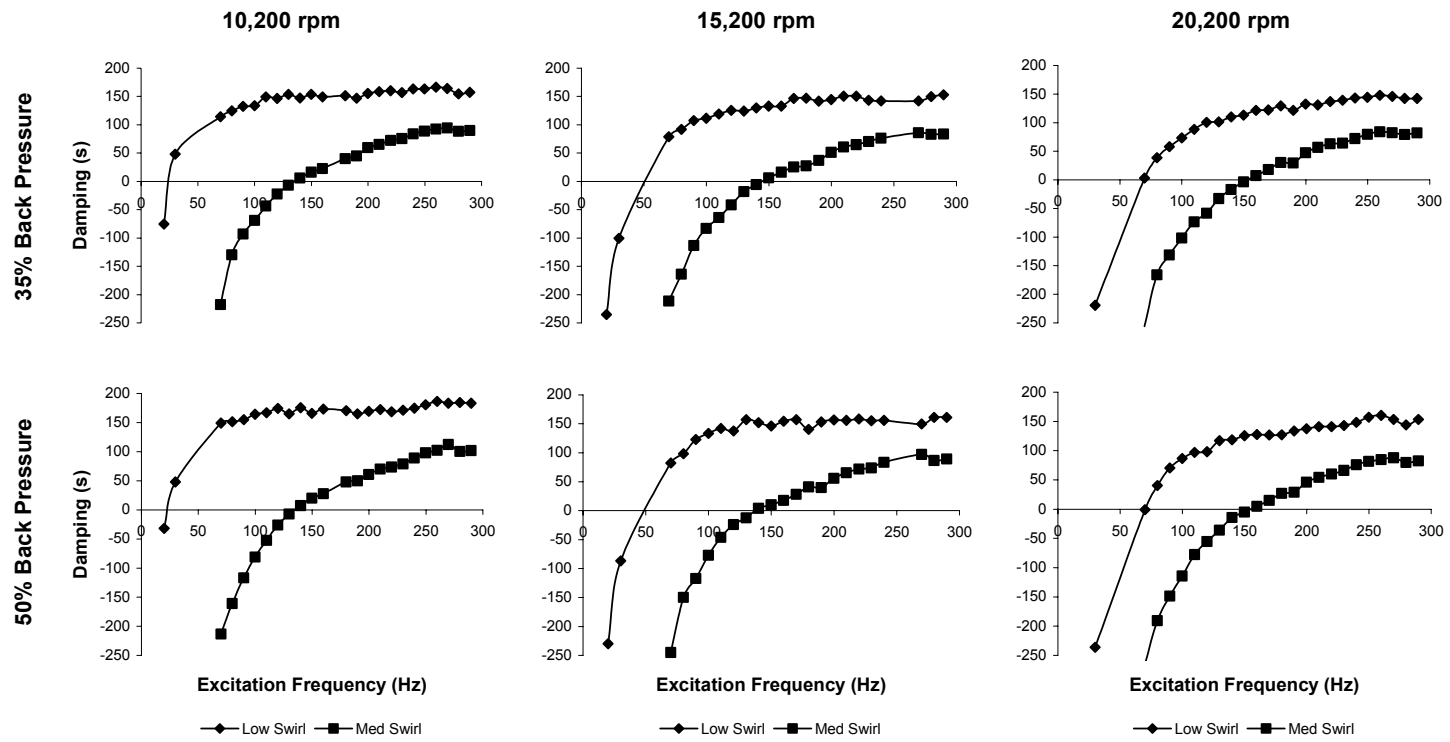
Figure 18: Experimental C_{eff}* Versus Excitation Frequency for Smooth-Bore Seals at Two Levels of Preswirl

2.3 Direct Comparison of Honeycomb and Smooth-Bore Seal

2.3.1 Low Preswirl

Figures 2-11 through 2-15 illustrate a comparison of the measured dynamic coefficients for the honeycomb and smooth seals using the low inlet preswirl ring. Each figure shows measured data for both the honeycomb and the smooth seal under the given test condition in order to give a direct comparison.

Figure 19 shows the significant loss in direct stiffness the honeycomb seal can contribute to the turbomachine rotor if its cells become clogged and it behaves as a smooth seal. The smooth seal maintains a fairly flat direct stiffness curve with relatively low values. The smooth seal also tends to be more sensitive to a change in backpressure, resulting in slightly negative stiffness for 35% backpressure and near zero values in the mid-frequency range for 20,200-rpm. In the 250 Hz to 300 Hz range, there is still about an 80% reduction for 35% backpressure and 72% reduction for 50% backpressure when comparing smooth seal values with that of the honeycomb seal. This could be troublesome if the honeycomb seal was being used to tune the critical speed above a typical running speed.

Figure 20 shows a comparison of the cross-coupled stiffness $k*$ for the two seal types. It can be seen that the values are comparable in the lower frequency range, but begin to diverge quickly as excitation frequency is increased. This divergence becomes more pronounced as rotor speed is increased due to the relative insensitivity of $k*$ for the honeycomb seal in the higher frequency range. Particularly at 20,200-rpm, the value of $k*$ for the honeycomb seals is about ¼ the magnitude of that of the smooth seal for the 200 Hz to 250 Hz range. This shows the significant decrease in stability that can occur if the

honeycomb seal was to begin behaving dynamically like a smooth seal, even for low preswirl conditions. It should be noted, however, that the honeycomb seal shows little stability advantage for low rotor speed and low excitation frequencies, especially below 100 Hz.

Direct damping is where the smooth seal shows a true advantage over the honeycomb seal. As shown in Figure 21, the value of $C*$ remains fairly constant over the entire frequency range for the smooth seal. While, for the honeycomb seal, $C*$ decreases fairly quickly and then levels off at higher frequencies. In the 250 Hz to 300 Hz range, the smooth seal has a magnitude about 310% (4.1x) greater than that of the honeycomb seal.

The effective stiffness, $K_{eff}*$, of the seals is demonstrated in Figure 22. The cross-coupled damping term, $c*$, is about 3 to 4 times larger in magnitude for the honeycomb seal. This causes a larger decrease in $K_{eff}*$ for the honeycomb seal than the smooth seal when compared to $K*$. It can also be seen that $K_{eff}*$ slightly decreases with an increase in rotor speed for the honeycomb seal, whereas, the smooth seal shows virtually no change with rotor speed. Overall, there is still potentially a large reduction in stiffness if the honeycomb seal was to take on the dynamic characteristics of a smooth seal in a dirty operating environment. In the 250 Hz to 300 Hz range, there is still about a 68%

reduction for 35% backpressure and 53% reduction for 50% backpressure when comparing smooth seal values with that of the honeycomb seal.

In Figure 23, the culmination of the effects of direct damping, C^*, and cross-coupled stiffness, k^*, are given in the effective damping coefficient, C_{eff}^*. From Figure 23, it can be seen that the smooth seal actually shows superior effective damping for low preswirl testing. This is the result of their inherently superior direct damping, as seen in Figure 21. Thus, for this case, the honeycomb seal shows little advantage in stability. Taking for example the 10,200-rpm and 15,200-rpm test cases, the smooth seal shows values ranging from about 60% (1.6x) larger at 100 Hz to about 250% (3.5x) larger at 300 Hz than the honeycomb seal. At 20,200-rpm, the smooth seal again shows about a 250% (3.5x) larger value at 300 Hz, however, only about a 20% (1.2x) larger value over the honeycomb seal at 100 Hz. This shows the sensitivity of the smooth seals to the increased tangential airflow created by the higher rotor speed and, thus, increased k^* values.

Figure 19: Comparison of Experimental *K** for Honeycomb and Smooth Bore Seals at Low Preswirl

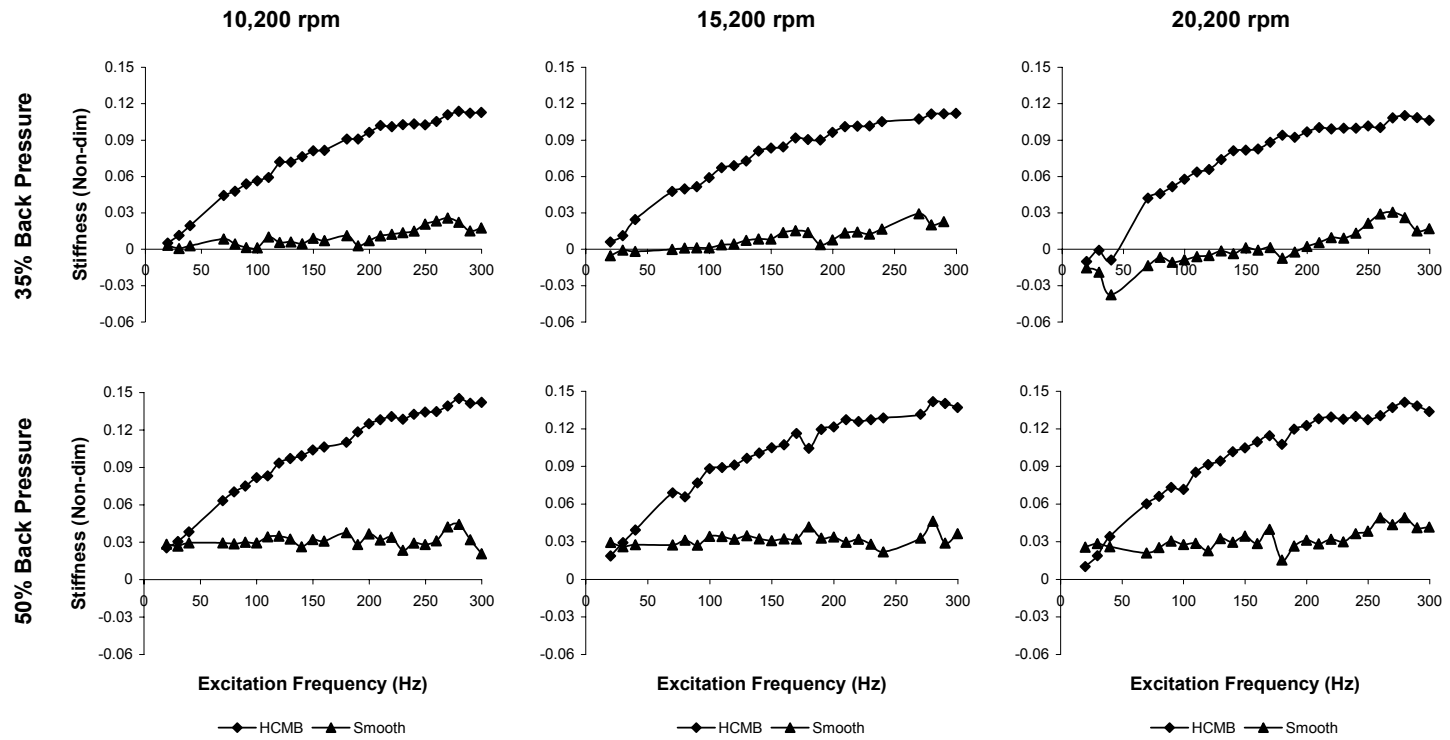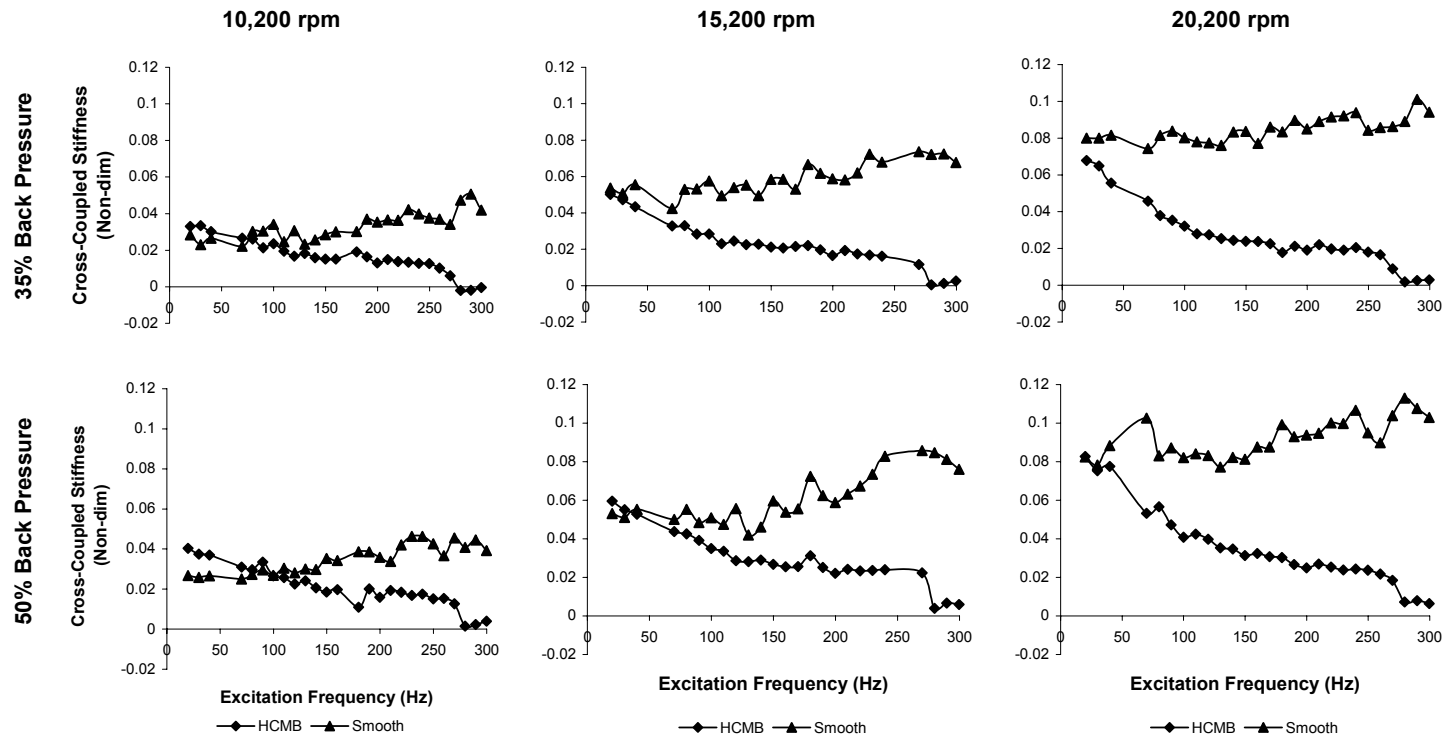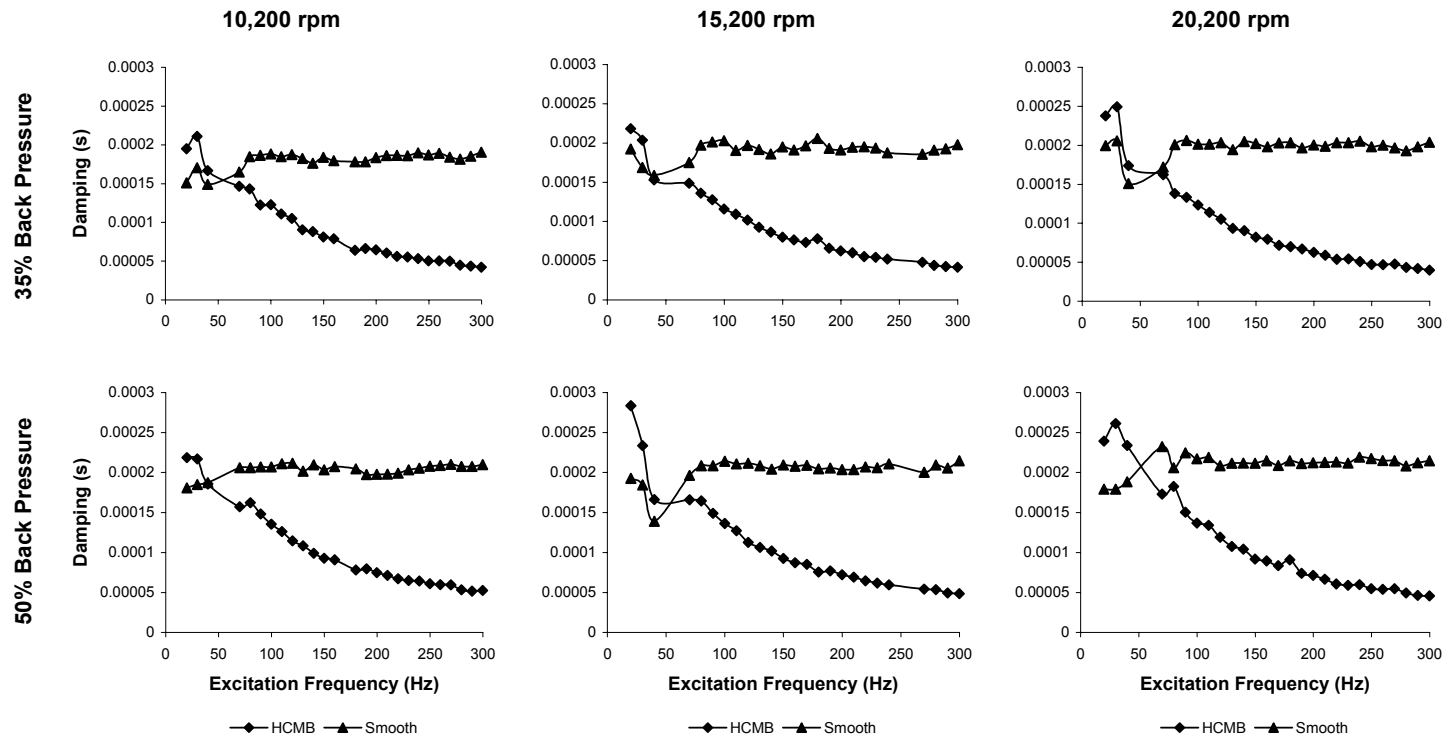**Figure 20: Comparison of Experimental *k** for Honeycomb and Smooth Bore Seals at Low Preswirl**

Figure 21: Comparison of Experimental *C** for Honeycomb and Smooth Bore Seals at Low Preswirl
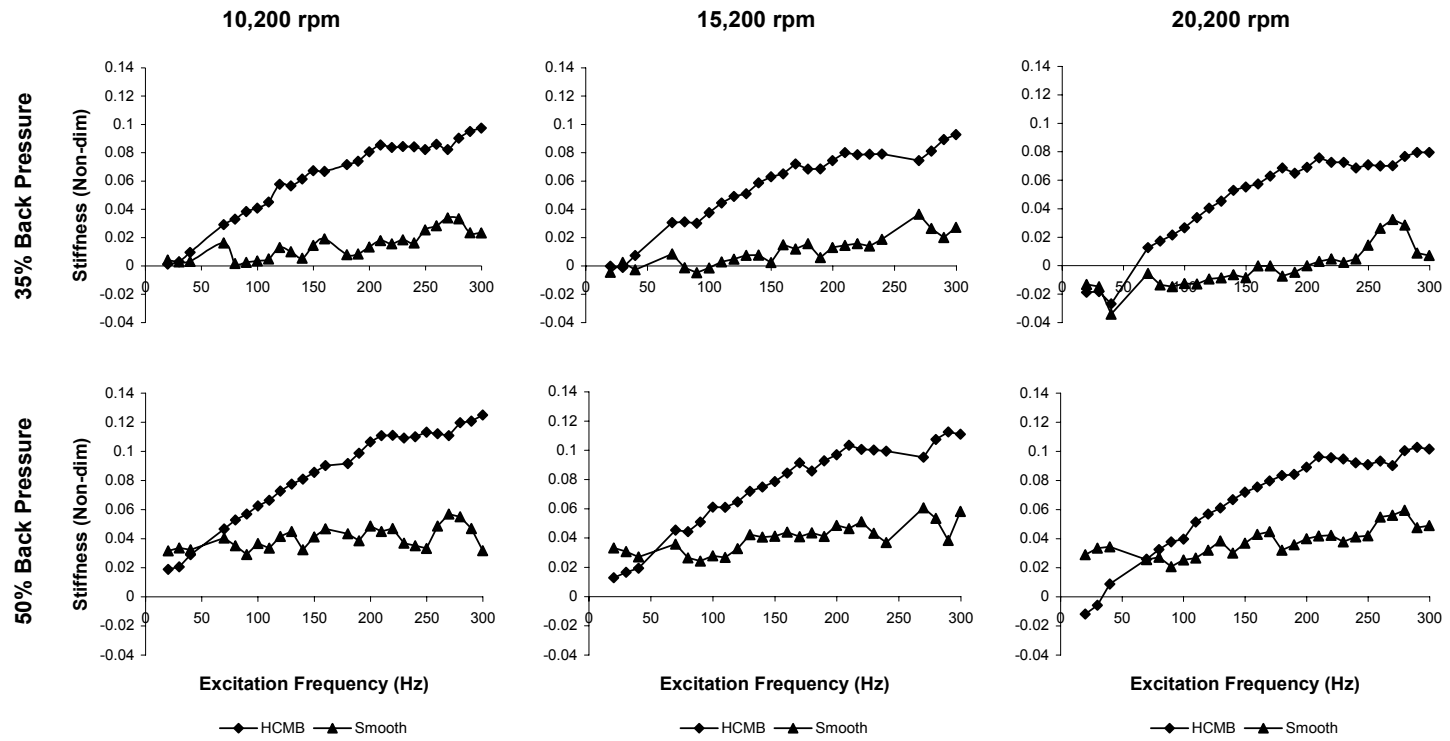
Figure 22: Comparison of Experimental $K_{eff}*$ for Honeycomb and Smooth Bore Seals at Low Preswirl

Figure 23: Comparison of Experimental $C_{eff}*$ for Honeycomb and Smooth Bore Seals at Low Preswirl

2.3.2 Medium Preswirl

Observing the recorded preswirl ratios in Table III and IV of Appendix B, it can be noted that the smooth seal obtains a much higher actual preswirl ratio for the 'medium' inlet preswirl ring installation than the honeycomb seal. Specifically, the smooth seal measures about 65% more preswirl for this inlet ring. Therefore, results for the smooth seal using the 'medium' inlet preswirl ring will be compared with results for the honeycomb seal using the 'high' preswirl inlet ring since there is only about a 15% difference in the actual preswirl ratio between these two.

Figure 24 particularly compares the direct stiffness K^* of each seal. It can be seen that there is an increase in data scatter and uncertainty for this comparison, particularly for the smooth seal. The trends are basically the same as for the low preswirl condition, and the magnitudes, overall, have little change as well. However, the smooth seal is less sensitive to a change in backpressure, and is able to maintain more stiffness in the mid-frequency range for 35% backpressure. This shows that the honeycomb seal would retain slightly more stiffness under higher preswirl conditions (>0.4) if its cells were to become clogged. However, it would still have a significant reduction in stiffness overall. In the 250 Hz to 300 Hz range, there is about a 67% reduction in stiffness for 35% backpressure and 61% reduction for 50% backpressure when comparing smooth seal results with that of the honeycomb seal.

Figure 25 demonstrates the very large loss in stability the honeycomb seal could see under higher preswirl conditions. For the entire frequency range, the smooth seal has significantly higher values, and for the 200 Hz to 300 Hz range, average about 600% (7.0x) higher than the honeycomb seal.

In contrast, Figure 26 shows that there is basically no change for C^* in trend or magnitude for either seal with increased preswirl. Values for the smooth seal still exceed that of the honeycomb seal above about 70 Hz. In the 250 Hz to 300 Hz range, the smooth seal has a magnitude again about 300% (4.0x) greater than that of the honeycomb seal.

A comparison of the effective stiffness, K_{eff}^*, for each seal is given in Figure 27. As with low inlet preswirl, the cross-coupled damping term, c^*, is much larger for the honeycomb seal than the smooth seal; for this case, about 8 times larger. So, again, the reduction in K_{eff}^* is less than the reduction seen in K^* when comparing honeycomb and smooth seal results. In the 250 Hz to 300 Hz range, the honeycomb seal shows a reduction in effective stiffness by about 50% for 35% backpressure, and about 31% for 50% backpressure when compared with smooth seal results. So, overall results show smaller, yet still significant, stiffness reduction for higher preswirl conditions.

Unlike low preswirl tests, Figure 28 demonstrates that the smooth seal no longer shows an advantage for C_{eff}^*. The effect of the much-increased cross-coupled stiffness has driven the values of C_{eff}^* significantly down for the smooth seal. The cross-over frequency has increased from roughly 70 Hz for low preswirl tests to about 140 Hz. Whereas, the honeycomb seal cross-over frequency remains at about 50 to 70 Hz. Also, Figure 28 shows that the honeycomb seal has higher values of C_{eff}^* for all backpressure settings and rotor speeds up to about 200 Hz. This could be detrimental to a system running below 200 Hz if it was applying this honeycomb seal in a dirty working environment which could cause its cells to become clogged.

Figure 24: Comparison of Experimental *K** for Honeycomb and Smooth Bore Seals at Medium Preswirl

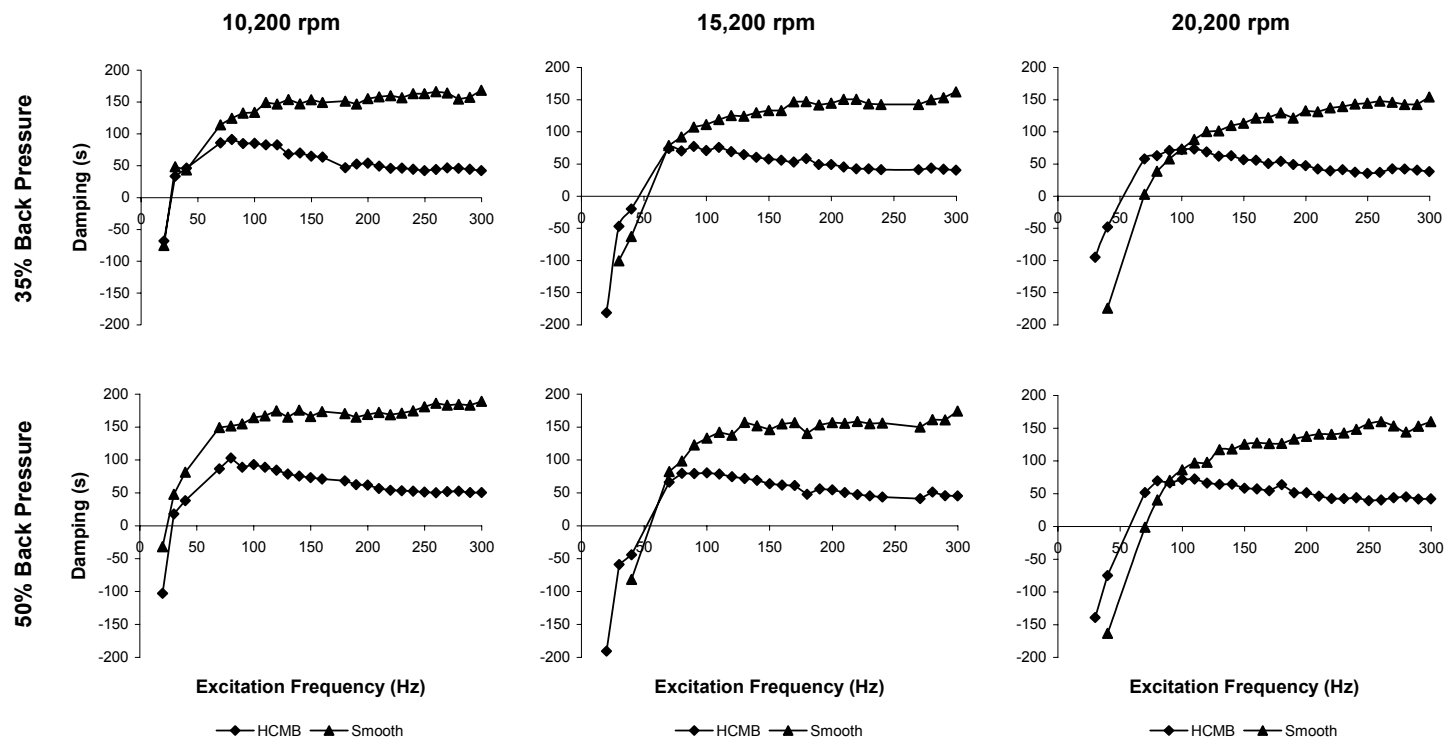**Figure 25: Comparison of Experimental *k** for Honeycomb and Smooth Bore Seals at Medium Preswirl**

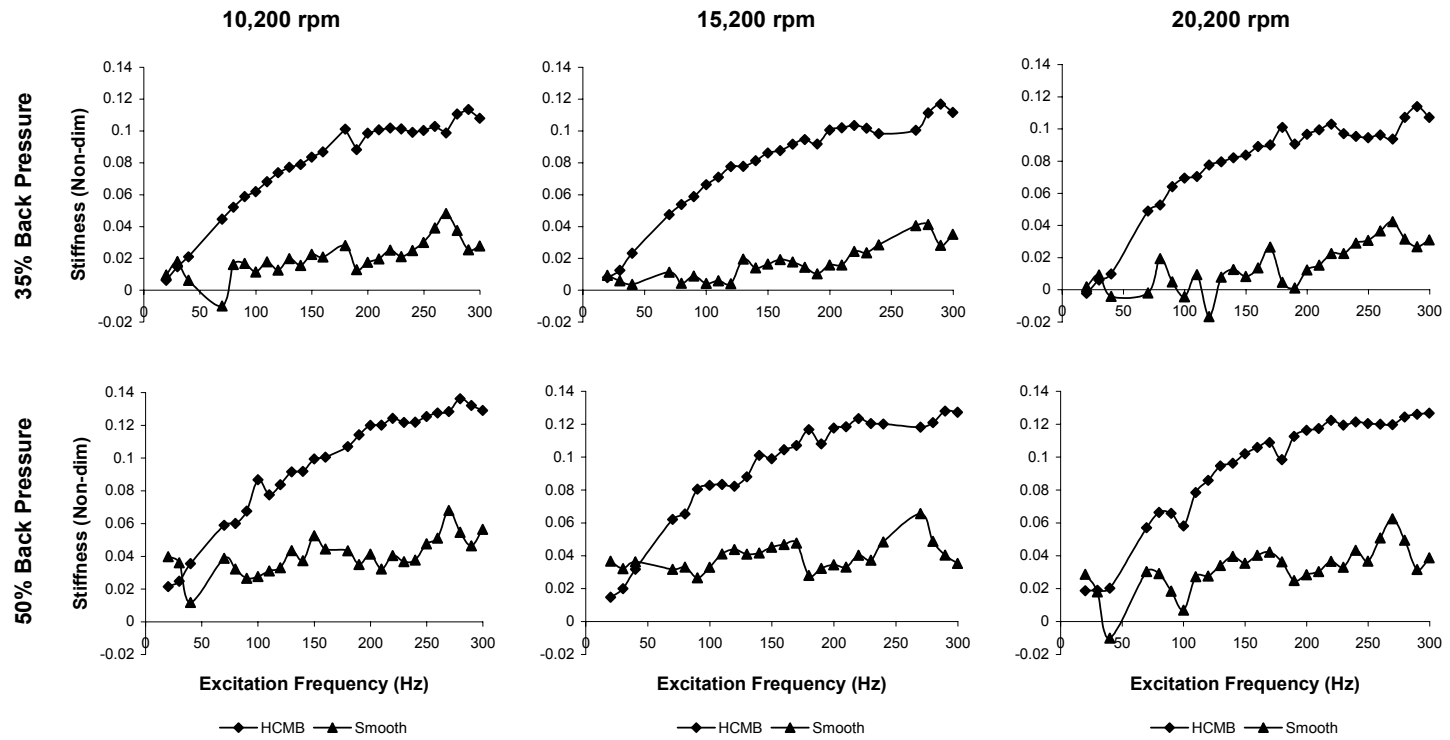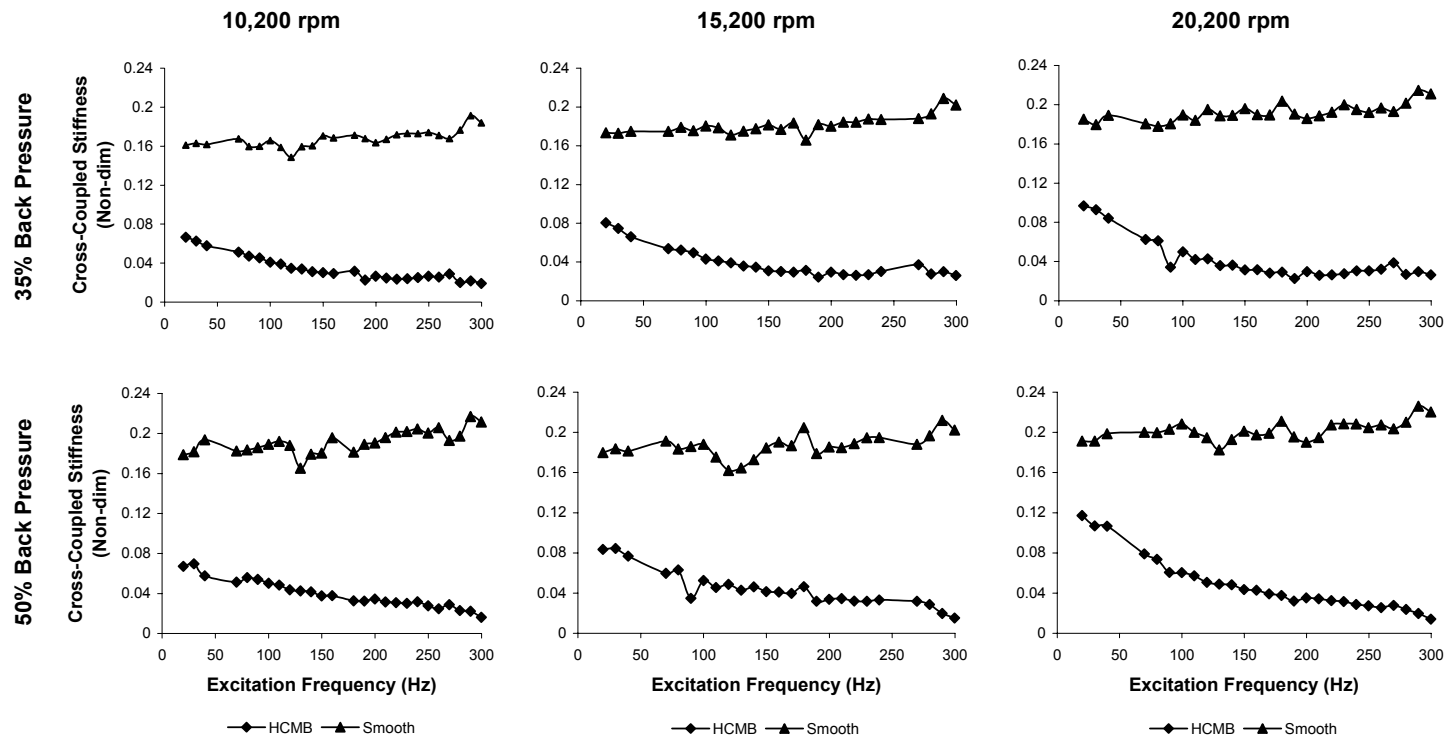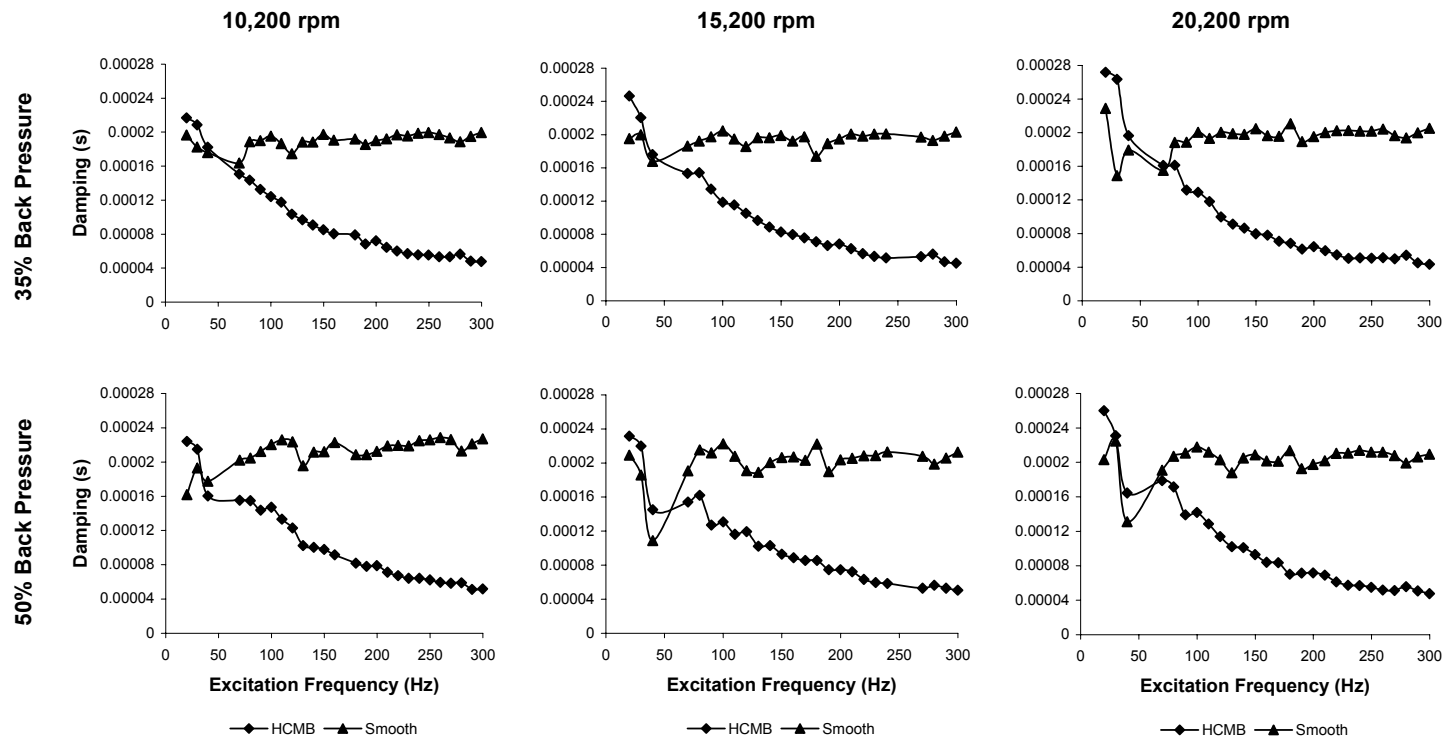**Figure 26: Comparison of Experimental *C** for Honeycomb and Smooth Bore Seals at Medium Preswirl**
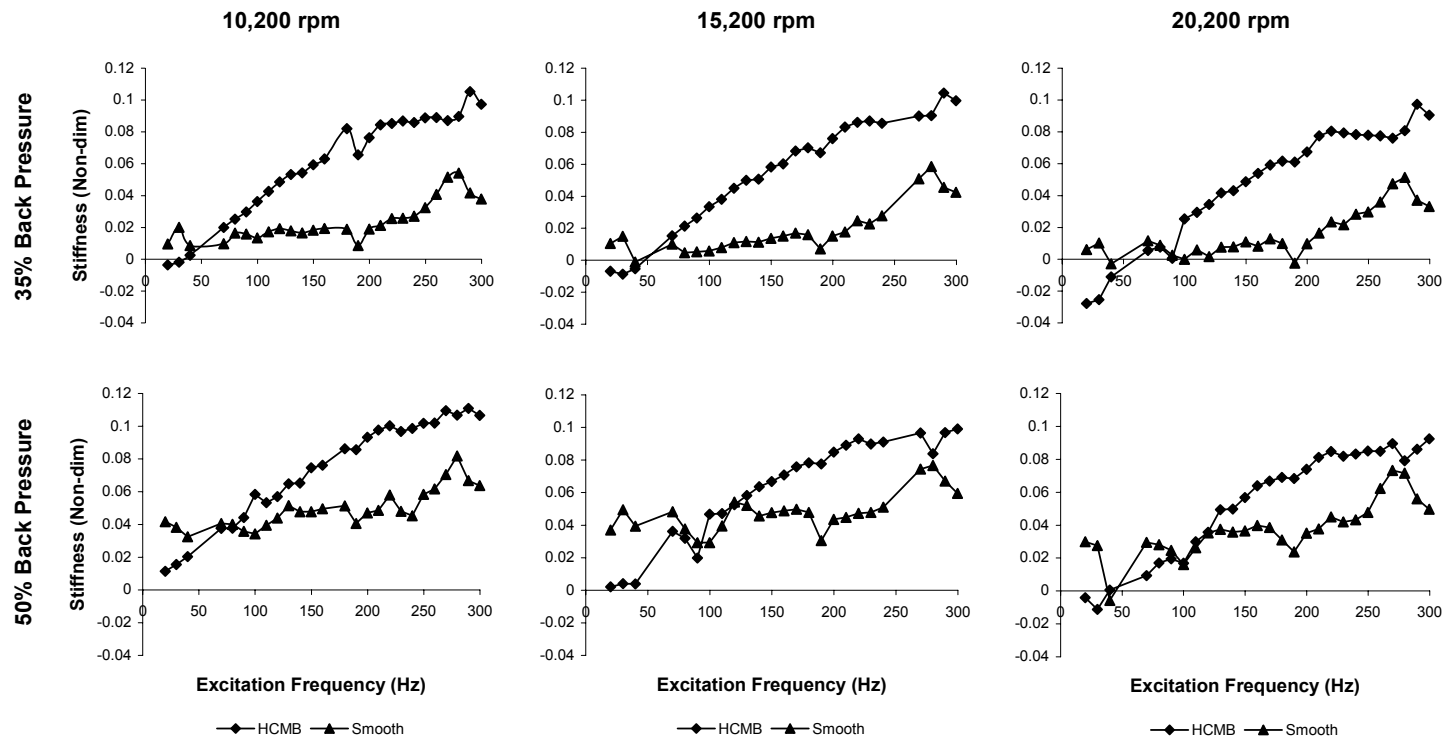
Figure 27: Comparison of Experimental $K_{eff}*$ for Honeycomb and Smooth Bore Seals at Medium Preswirl
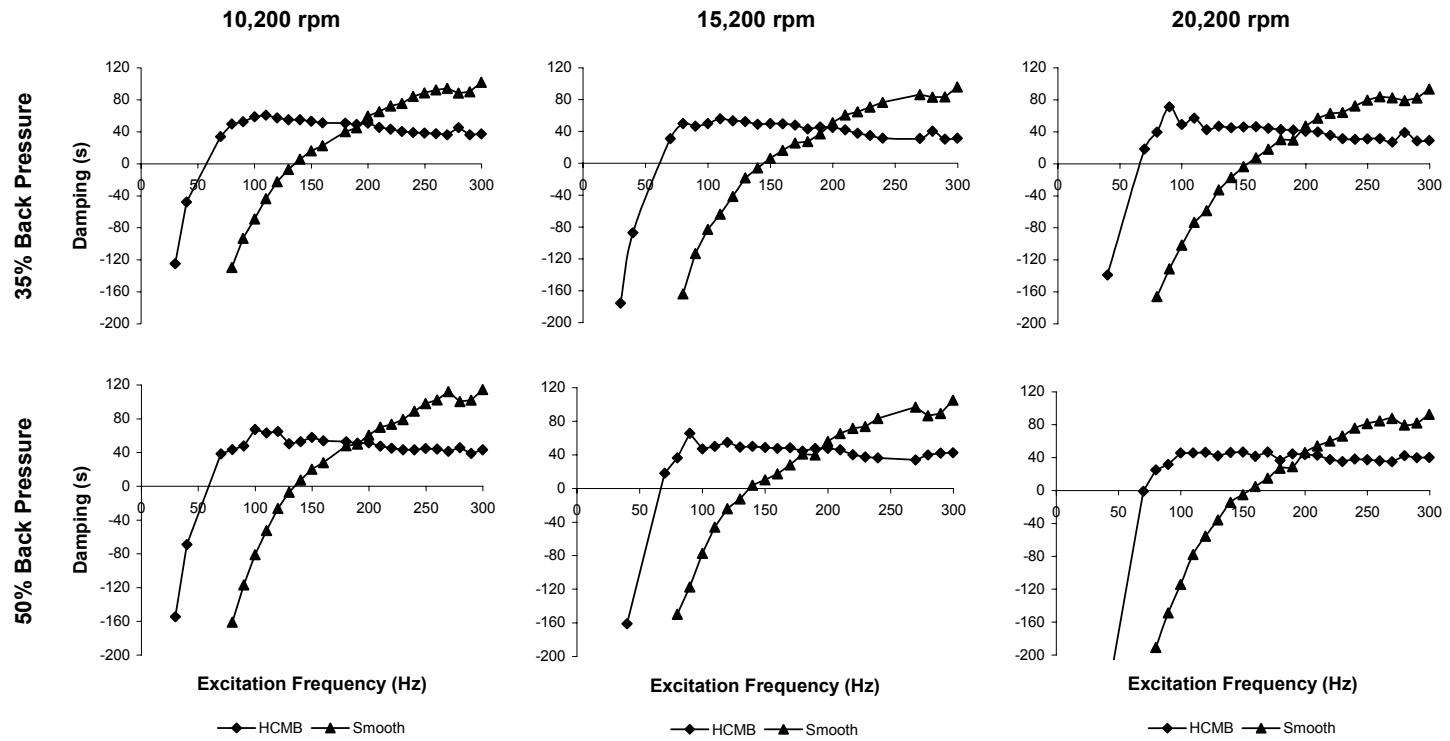
Figure 28: Comparison of Experimental C_{eff}^* for Honeycomb and Smooth Bore Seals at Mediun Preswirl

3   EXPERIMENT VERSUS THEORY

The measured dynamic coefficients illustrated and discussed in Section 2 for the honeycomb and smooth seal are now compared with predictions made by the computer program ISOTSEAL. This program incorporates both a frequency-independent, bulk-flow model for the smooth seal, as well as a frequency-dependent, two-control volume model for the honeycomb seal, developed by Kleynhans and Childs (1997). A sample input to the program is given below in Table I.

Table I: Sample Input to Program ISOTSEAL

Input Parameters	Metric Units	English Units
Reservoir Pressure	71.24 (bar)	1033 (psia)
Sump Pressure	10.69 (bar)	155.0 (psia)
Reservoir Temperature	23.28 (C)	73.9 (F)
Rotational Speed	10209 (rpm)	10209 (rpm)
Seal Diameter	114.295 (mm)	4.4998 (in)
Seal Length	85.73 (mm)	3.3752 (in)
Inlet Clearance	0.20701 (mm)	8.150 (mils)
Exit Clearance	0.20574 (mm)	8.100 (mils)
Cell Volume/Area Ratio	2.2 (mm)	0.0866 (in)
Inlet Preswirl Ratio	1.082 (-)	1.082 (-)
Entrance Loss Coefficient	0.000 (-)	0.000 (-)
Exit Recovery Factor	1.000 (-)	1.000 (-)
Absolute Viscosity	0.1880E-4 (Ns/m^2)	0.1263E-4 (lbm/ft.s)
Molecular Weight	28.96 (-)	28.96 (-)
Specific Heat Ratio	1.400 (-)	1.400 (-)
Compressibility Factor	1.000 (-)	1.000 (-)
Tolerance Percentage	0.500 (-)	0.500 (-)
# Integration Steps	100 (-)	100 (-)
n_{rz}	0.0586	0.0586
m_{rz}	-0.217	-0.217
n_{sz}	0.0785	0.0785
m_{sz}	-0.1101	-0.1101
Nos. of Freq.	30	30
Freq Interval	600	600

The coefficients *n* and *m* in Table I are based on experimental flat-plate test results performed by Ha and Childs (1992), and represent those used for the honeycomb seals in these analyses. These coefficients are used in Equation 27 in Appendix A to determine the appropriate friction factor *f* for the rotor and seals. Similarly, the coefficients used for the smooth seal are based on the work of Ha and Childs (1992). The rotor coefficients remained consistent for both sets of seals.

The ISOTSEAL program also calculates the flow rate through each seal, or the solution to the static equations, based on the same test conditions. These predictions are discussed and compared with experimental measurements for each seal in Section 3.3 at the end of this section.

For the purposes of direct comparison, the calculated theory values for the dynamic coefficients were also non-dimensionalized using Equation 16. Values for inlet pressure, seal inner diameter, etc. were the same as used for the measured values.

3.1 Honeycomb Seals

Error bars are included on experimental data to show spread of values in comparison to theoretical values. The standard deviation about the mean does not seem to be dependent on preswirl for the honeycomb seal. On average, the largest error bars show a standard deviation of approximately ±4%, ±6%, ±3.5%, ±5.5%, and ±6.5% about the mean value for K^*, k^*, C^*, K_{eff}^*, and C_{eff}^* , respectively. In some cases, as with k^*, the error bars average a slightly smaller value at higher preswirl.

Figure 29 through Figure 31 demonstrate experimental data and theoretical predictions for K^*. In agreement with the experimental results in Section 2, the theory also predicts little change in K^* with increased preswirl. Theoretical predictions show good agreement with the measured frequency-dependent nature of the honeycomb seal for all levels of preswirl. Agreement in magnitude is exceptional at 35% and 50% backpressure. Theory, in general, tends to under-predict the value of K^* up to a frequency of about 170 Hz, and over-predict thereafter up to the test limit of 300 Hz. This disagreement is more exaggerated for the 15% backpressure condition, in which there is significant under-prediction by theory in the low excitation frequency range. The discrepancy at this backpressure may be due to the theoretical prediction of choked airflow in the seals, which was not realized in actual tests until a slightly lower backpressure. Excluding the 20 to 100 Hz frequency range for 15% backpressure, there is, on average, no more than a 12% discrepancy between theory and measured values for all test conditions and preswirl levels.

Measured values for k^* also show good agreement in trend with theoretical predictions as shown Figure 32 through Figure 34. Theory typically under-predicts for low preswirl by about 30% on average. For medium preswirl, theory typically over-predicts by 21% on average in the low frequency range, and under-predicts by 18% on average in the upper frequency range. The high preswirl case is similar, with theory over-predicting on average by 24% in the low frequency range, and under-predicting by 23% on average in the upper frequency range. The transition point between over-prediction and under-prediction at high preswirl is 200 Hz for 35% and 50% backpressure, and 170 Hz for 15% backpressure. So, it appears that, as preswirl is increased, the theory over-

compensates for the change in k^* in the low to mid frequency range, but continues to under-predict in the upper frequency range.

Figure 35 through Figure 37 compare theory with measured values for direct damping C^*. Again, theory matches the frequency-dependent nature of C^* well in trend. Magnitude is slightly under-predicted for 35% and 50% backpressure by 16% on average in all three cases of preswirl. However, it seems the theory overcompensates as the backpressure is lowered to 15%, causing an over-prediction across nearly the entire frequency range (20-250 Hz) by an average of 14% for all levels of preswirl. Theory under-predicts after 250 Hz by an average of 11%.

Results for K_{eff}^* are shown in Figure 38 through Figure 40. Similar to K^*, theory tends to under-predict for low frequencies and over-predict for higher frequencies. However, theory predicts a larger magnitude for the cross-coupled damping c^* than was measured, causing under-prediction for a larger portion of the frequency range. This under-prediction increases as preswirl and rotor speed are increased. For example, excluding 15% backpressure, the theory under-predicts K_{eff}^* by about 32% on average up to at least 280 Hz, if not for the entire frequency range, for high preswirl. In contrast, at low preswirl and low rotor speed, theory under-predicts by about 21% on average up to about the 120 to 150 Hz range, and over-predicts thereafter by about 15%. Correlation was less agreeable for 15% backpressure. Theory under-predicts in the low frequency range between 54% and 75%, and over-predicts in the upper frequency range between 29% and 9% as preswirl is increased from low to high.

Finally Figure 41 through Figure 43 show experiment and theory for the effective damping, C_{eff}^*. Immediate observation shows that, again, theory predicts the trend of the

data over the frequency range quite well. Theory predicts a larger drop in the values of $C_{eff}*$ with increased inlet preswirl than was actually measured This causes agreement between measured data and theory to lessen for 35% and 50% backpressure. On the contrary, agreement betters for 15% backpressure since theory significantly over-predicts measured data at low preswirl. On average, theory under-predicts for 35% and 50% backpressure by about 10% at low preswirl, 25% at medium preswirl, and 37% at high preswirl. The 15% backpressure condition shows a 27% over-prediction at low preswirl, 17% over-prediction at medium preswirl, 16% over-prediction at high preswirl. Rotor speed seems to have little effect on correlation.

Table II below shows the measured and predicted frequencies at which $C_{eff}*$ is a maximum for the various test conditions. This is referred to as the break frequency, or break point. Theory predicts a steady shift of the break point to higher frequencies as preswirl, rotor speed, and backpressure are all increased. Each of these three parameters seems to have about an equal effect on the shift. Measured data shows some agreement with prediction overall. Some scatter of the measured data in the low frequency range for medium and high preswirl made it difficult to locate the actual break point. So, the table simply shows the frequency with the highest measured value of $C_{eff}*$. Consequently, agreement between theory and experiment is highest for low preswirl, where data scatter is minimal.

Table II: Experiment vs. Theory for Damping Break Points

Back-Pressure		Low Preswirl			Medium Preswirl			High Preswirl		
		10200 (RPM)	15200	20200	10200	15200	20200	10200	15200	20200
15%	Theory	60 (Hz)	70	90	80	90	100	100	110	110
	Measured	80	90	100	80	80	90	100	100	90
35%	Theory	80	90	110	100	120	130	140	140	150
	Measured	80	90	110	100	70	100	110	120	90
50%	Theory	90	100	120	120	130	150	160	170	180
	Measured	80	100	110	100	90	100	100	90	150

Figure 29: Experimental and Theoretical _K*_ Versus Excitation Frequency for Low Preswirl

10,200 rpm   **15,200 rpm**   **20,200 rpm**

Figure 30: Experimental and Theoretical *K** Versus Excitation Frequency for Medium Preswirl

Figure 31: Experimental and Theoretical *K** Versus Excitation Frequency for High Preswirl

Figure 32: Experimental and Theoretical _k*_ Versus Excitation Frequency for Low Preswirl

Figure 33: Experimental and Theoretical *k** Versus Excitation Frequency for Medium Preswirl

Figure 34: Experimental and Theoretical *k** Versus Excitation Frequency for High Preswirl
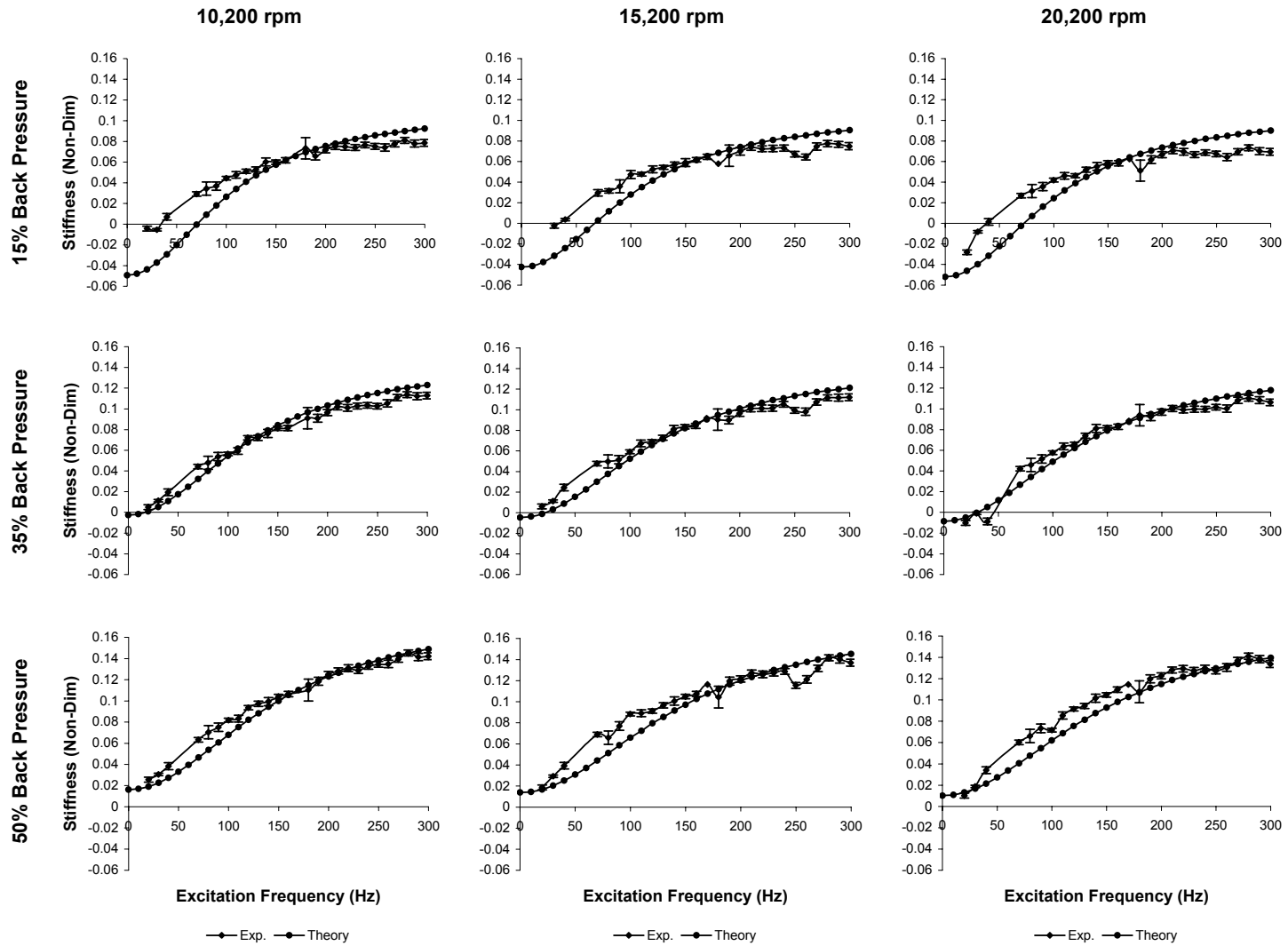
Figure 35: Experimental and Theoretical *C** Versus Excitation Frequency for Low Preswirl
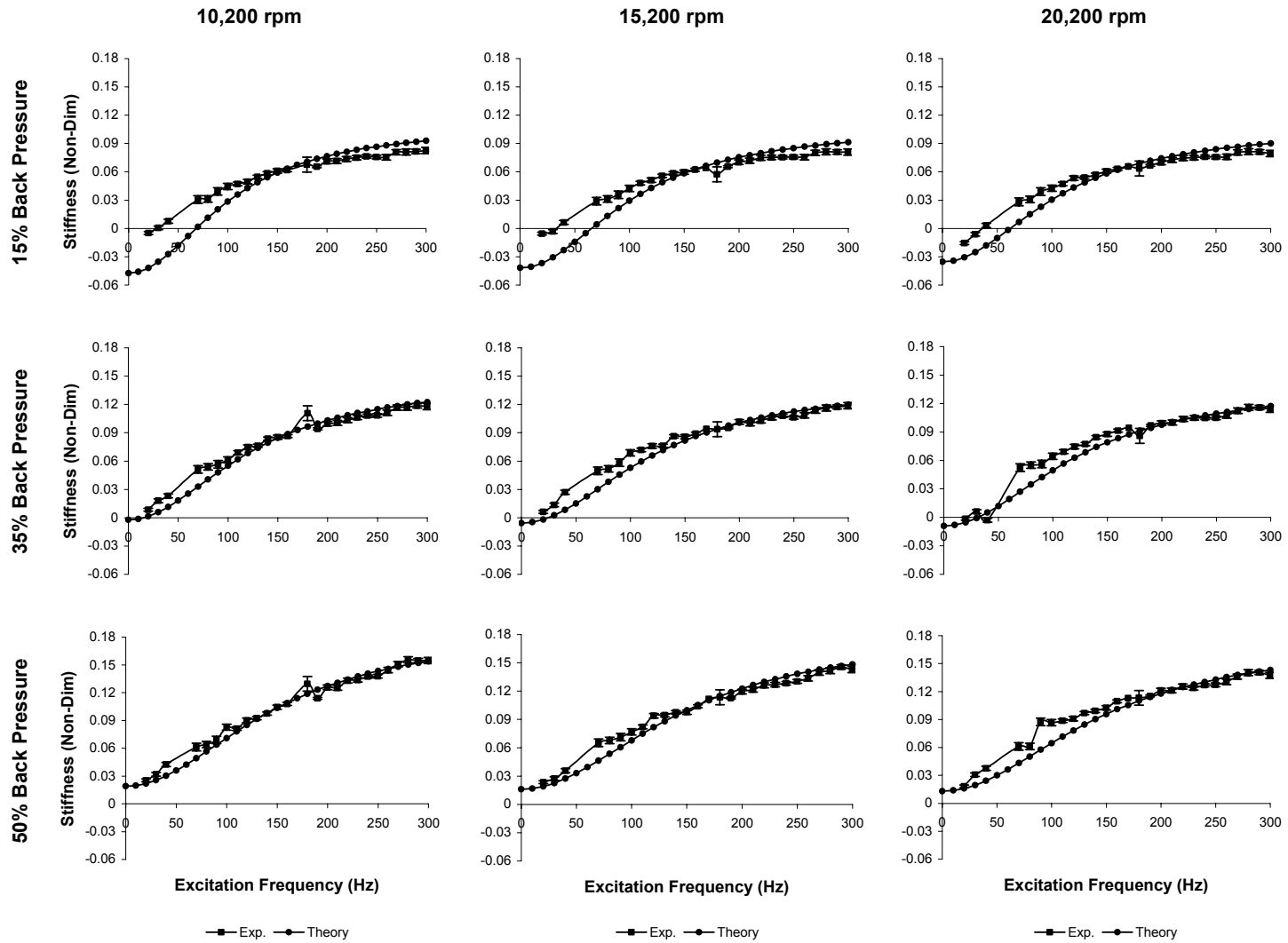
Figure 36: Experimental and Theoretical *C** Versus Excitation Frequency for Medium Preswirl

Figure 37: Experimental and Theoretical *C** Versus Excitation Frequency for High Preswirl

Figure 38: Experimental and Theoretical $K_{eff}*$ Versus Excitation Frequency for Low Preswirl

Figure 39: Experimental and Theoretical K_{eff}* Versus Excitation Frequency for Medium Preswirl

Figure 40: Experimental and Theoretical $K_{eff}*$ Versus Excitation Frequency for High Preswirl

Figure 41: Experimental and Theoretical $C_{eff}*$ Versus Excitation Frequency for Low Preswirl
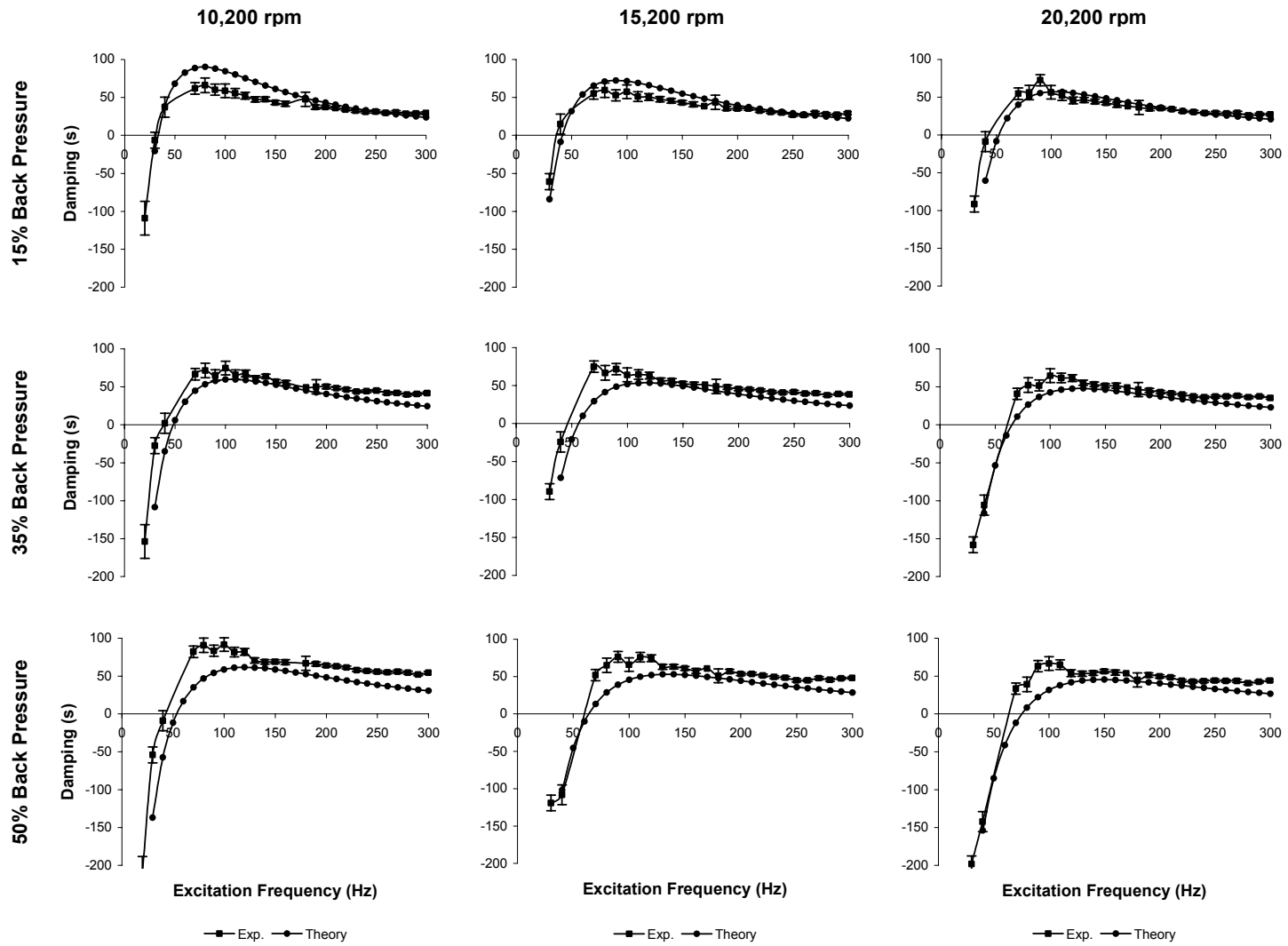
Figure 42: Experimental and Theoretical $C_{eff}*$ Versus Excitation Frequency for Medium Preswirl
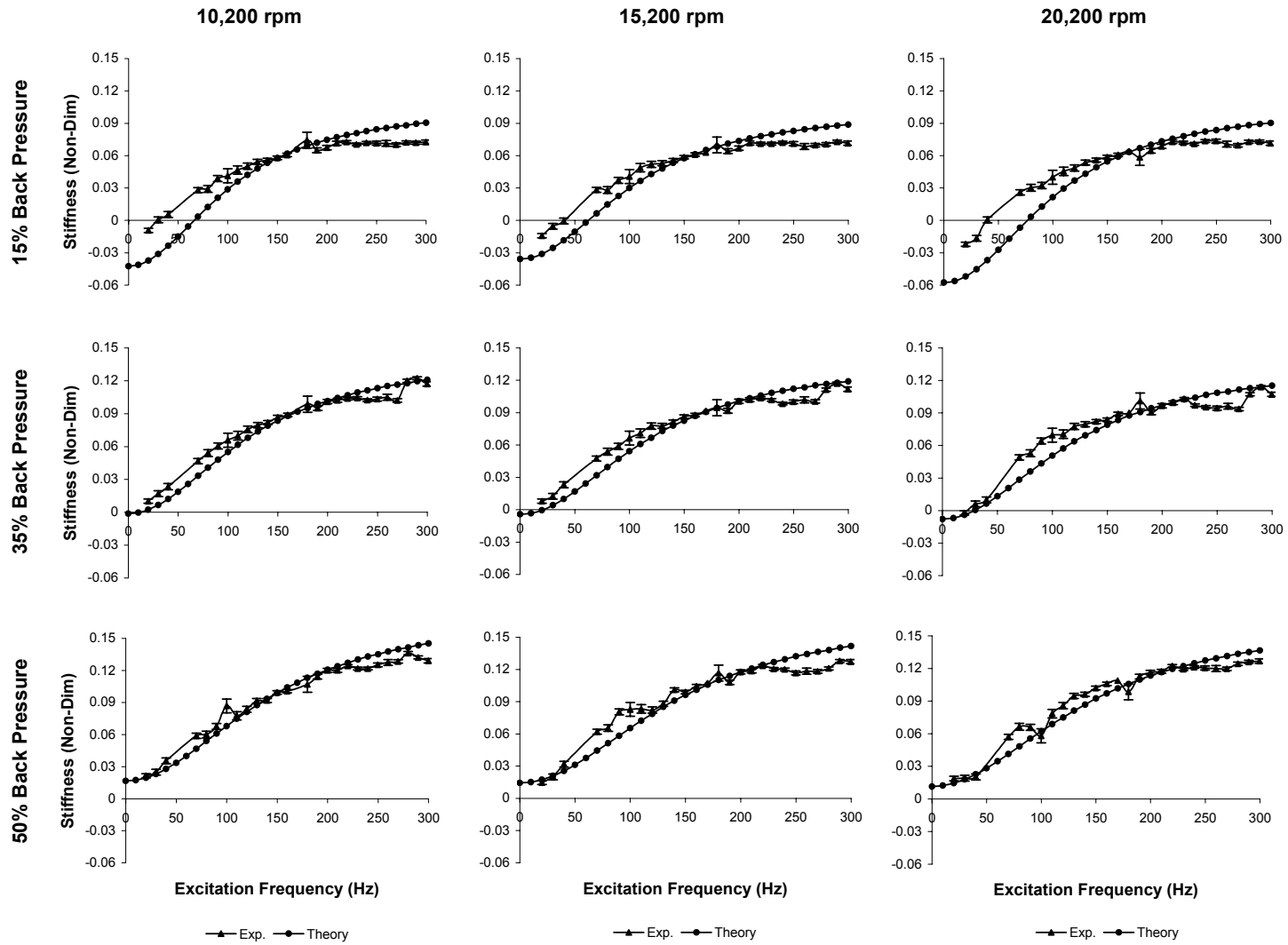
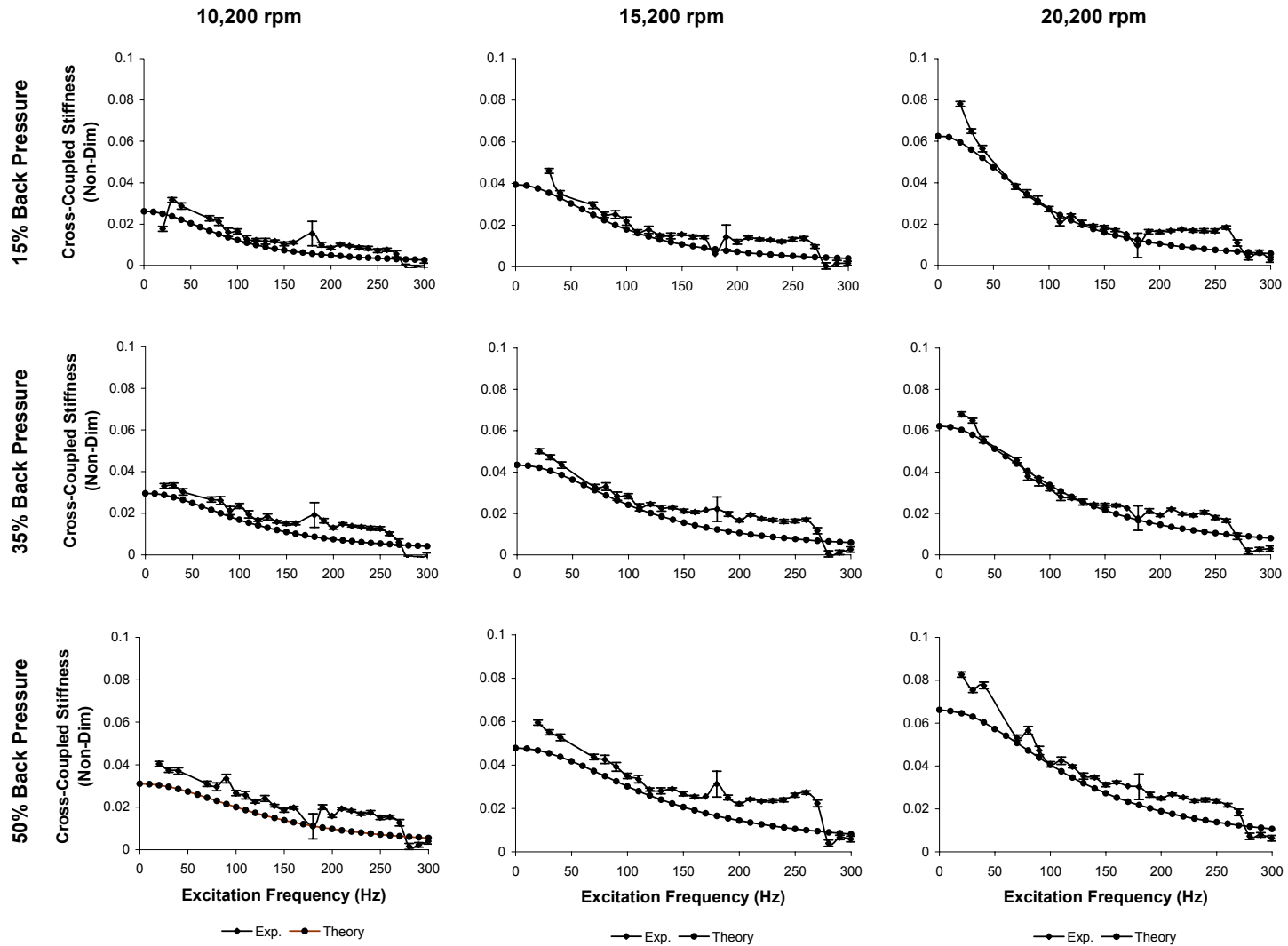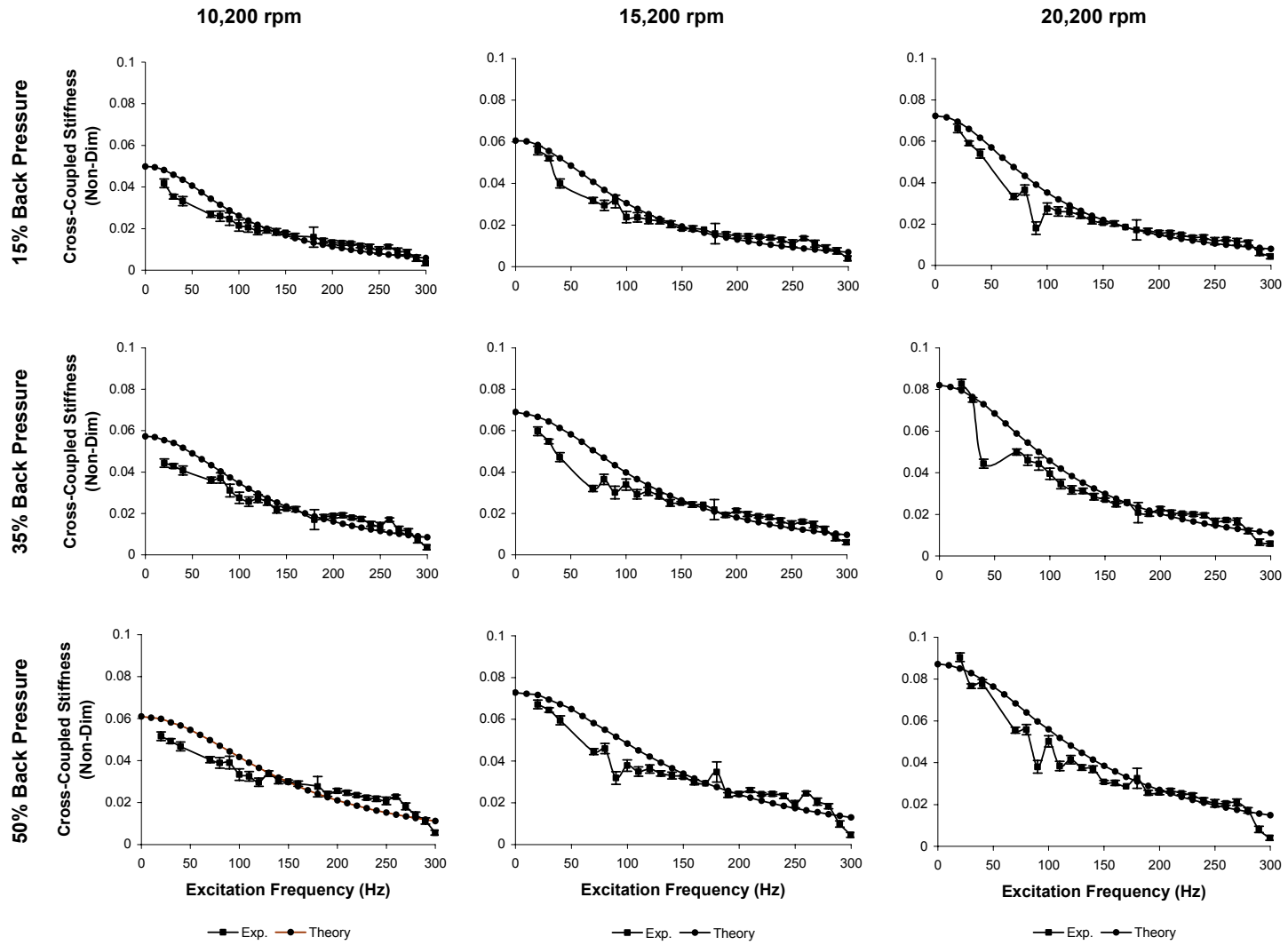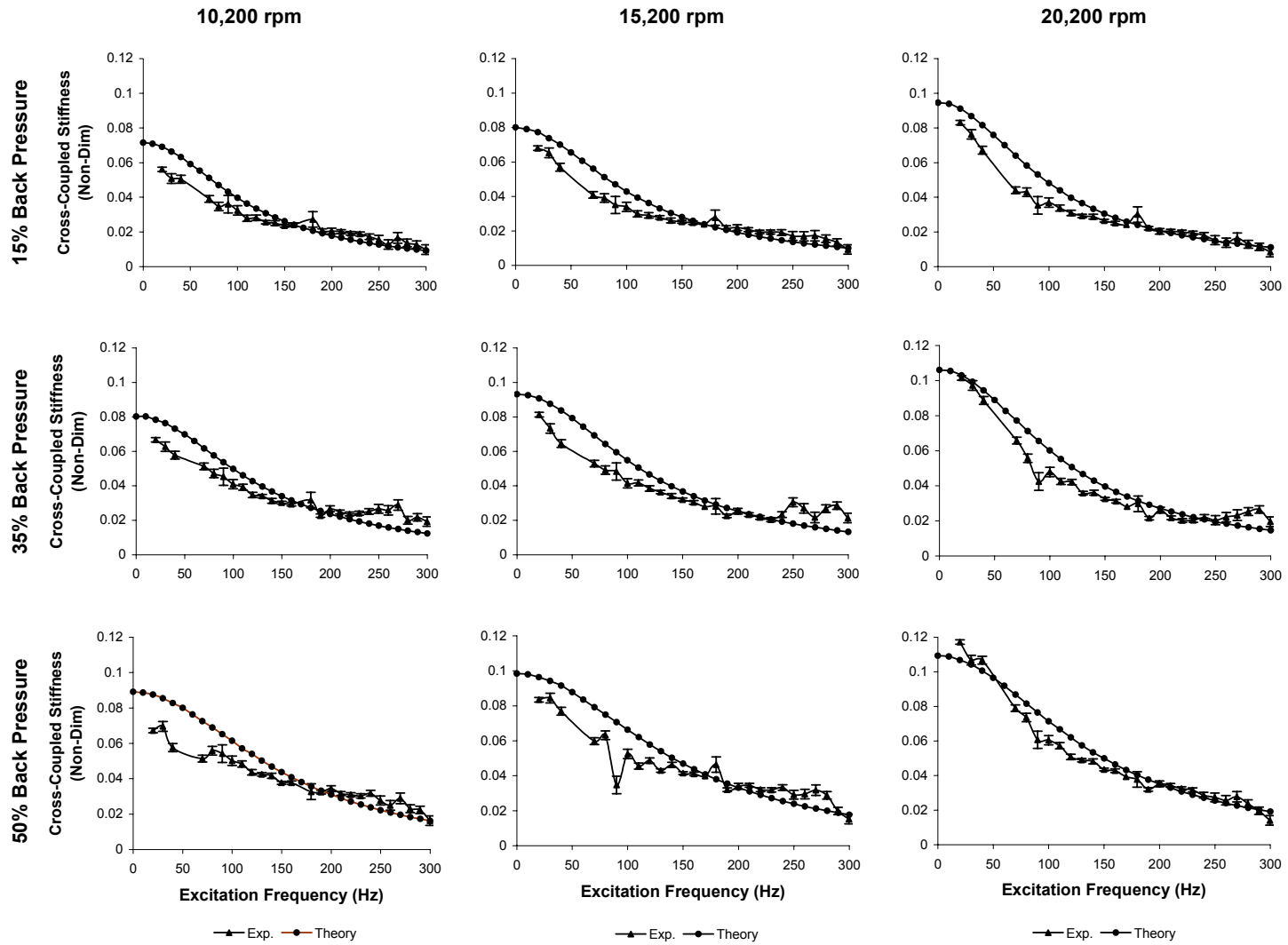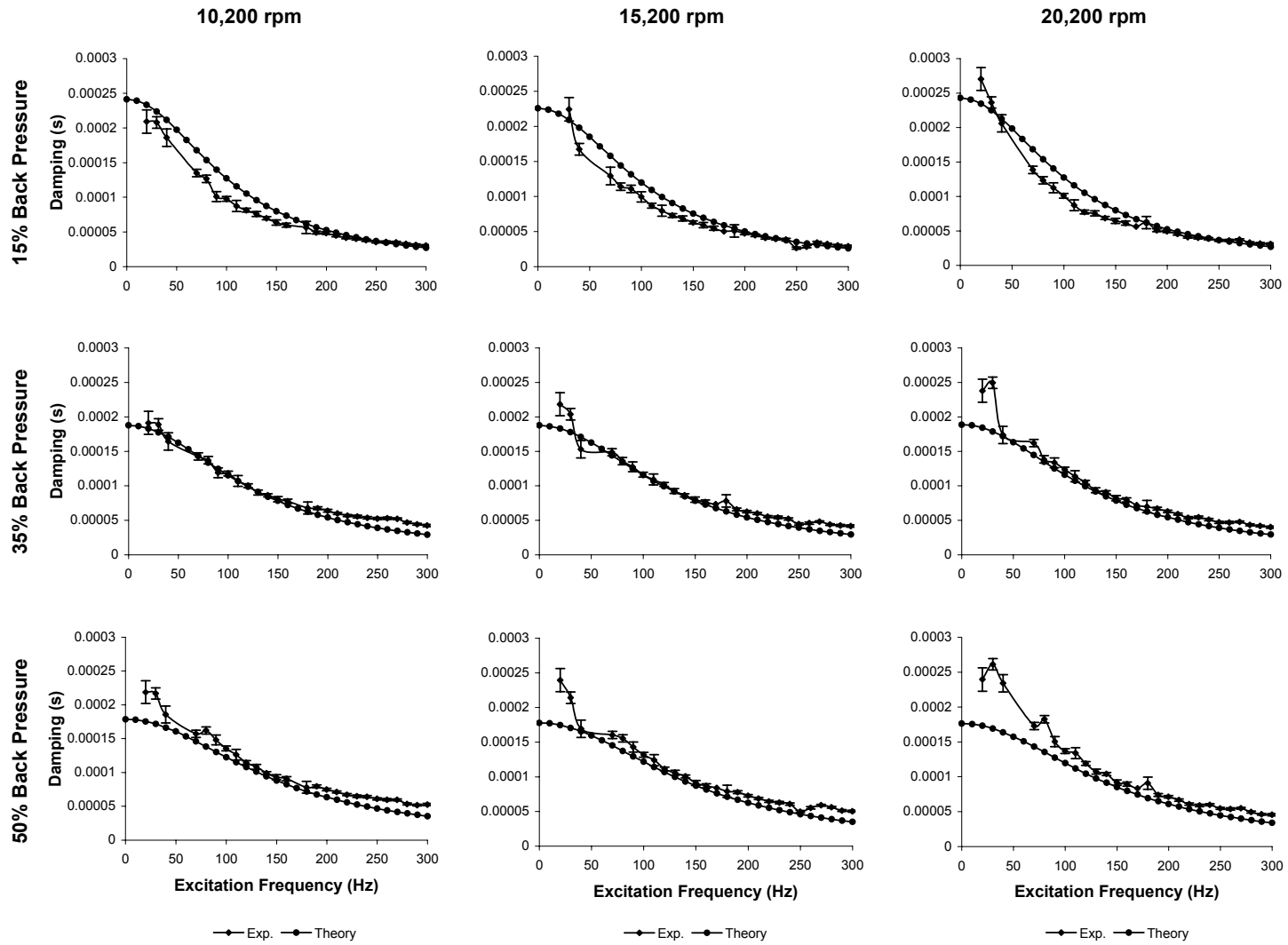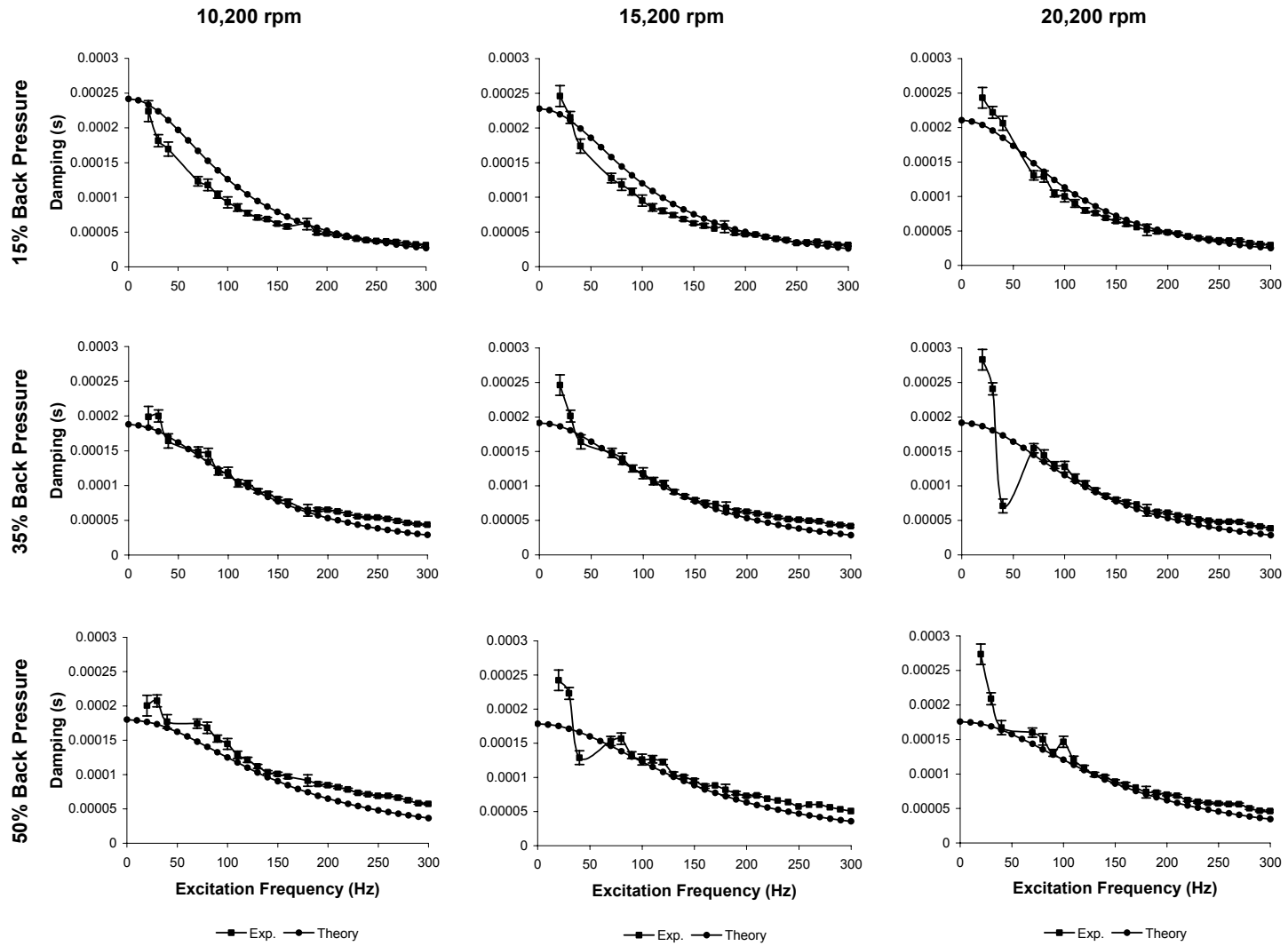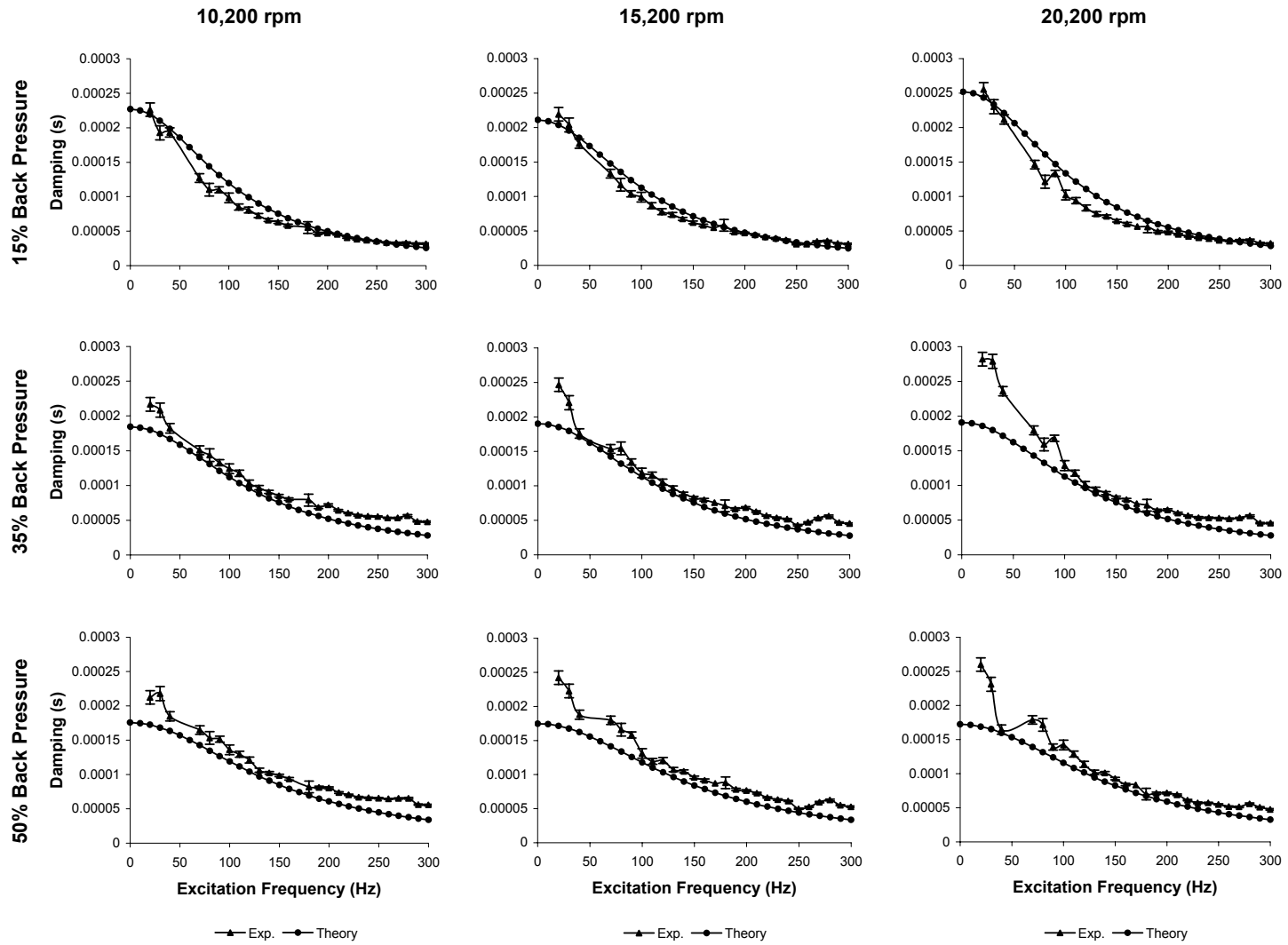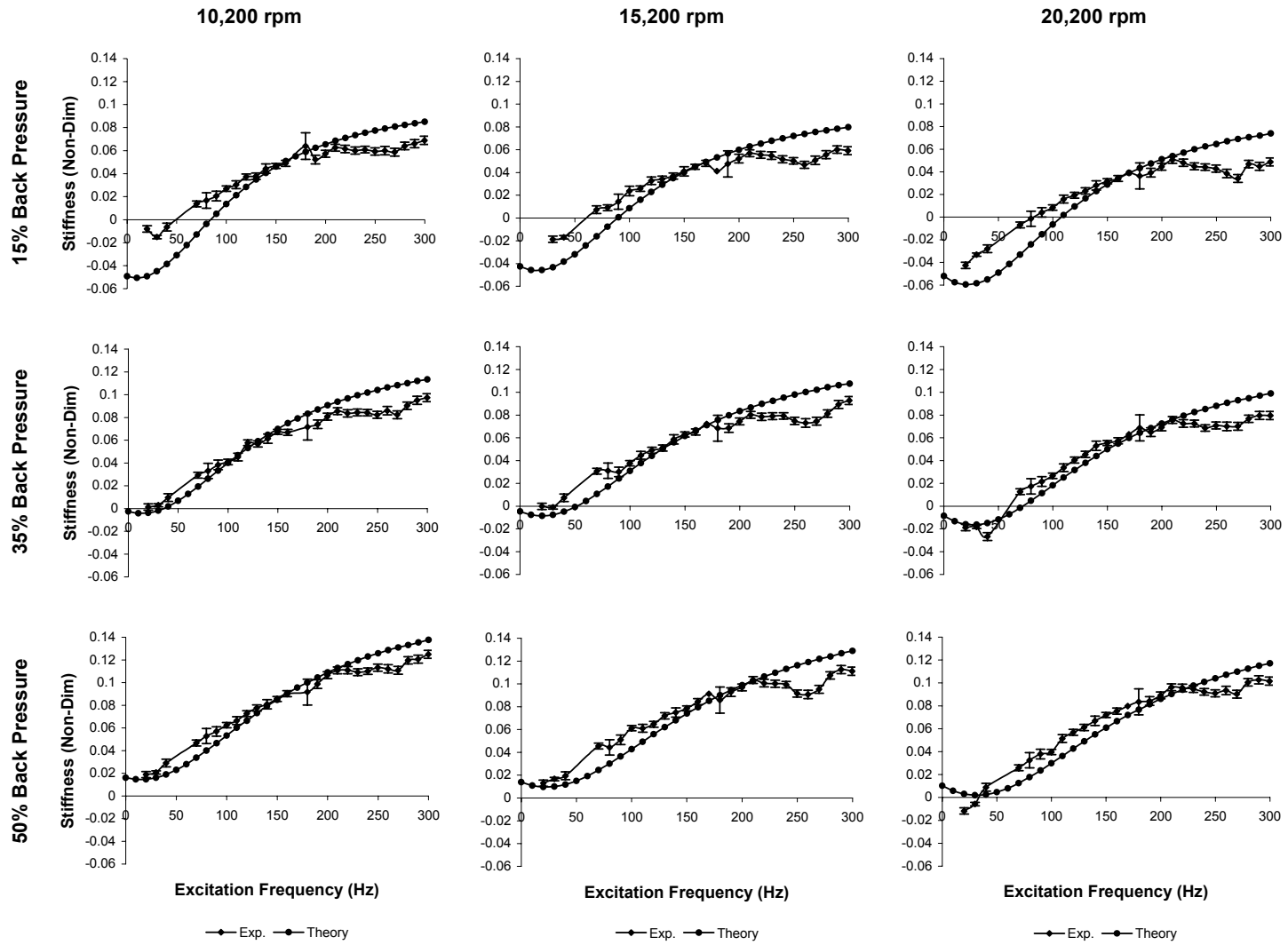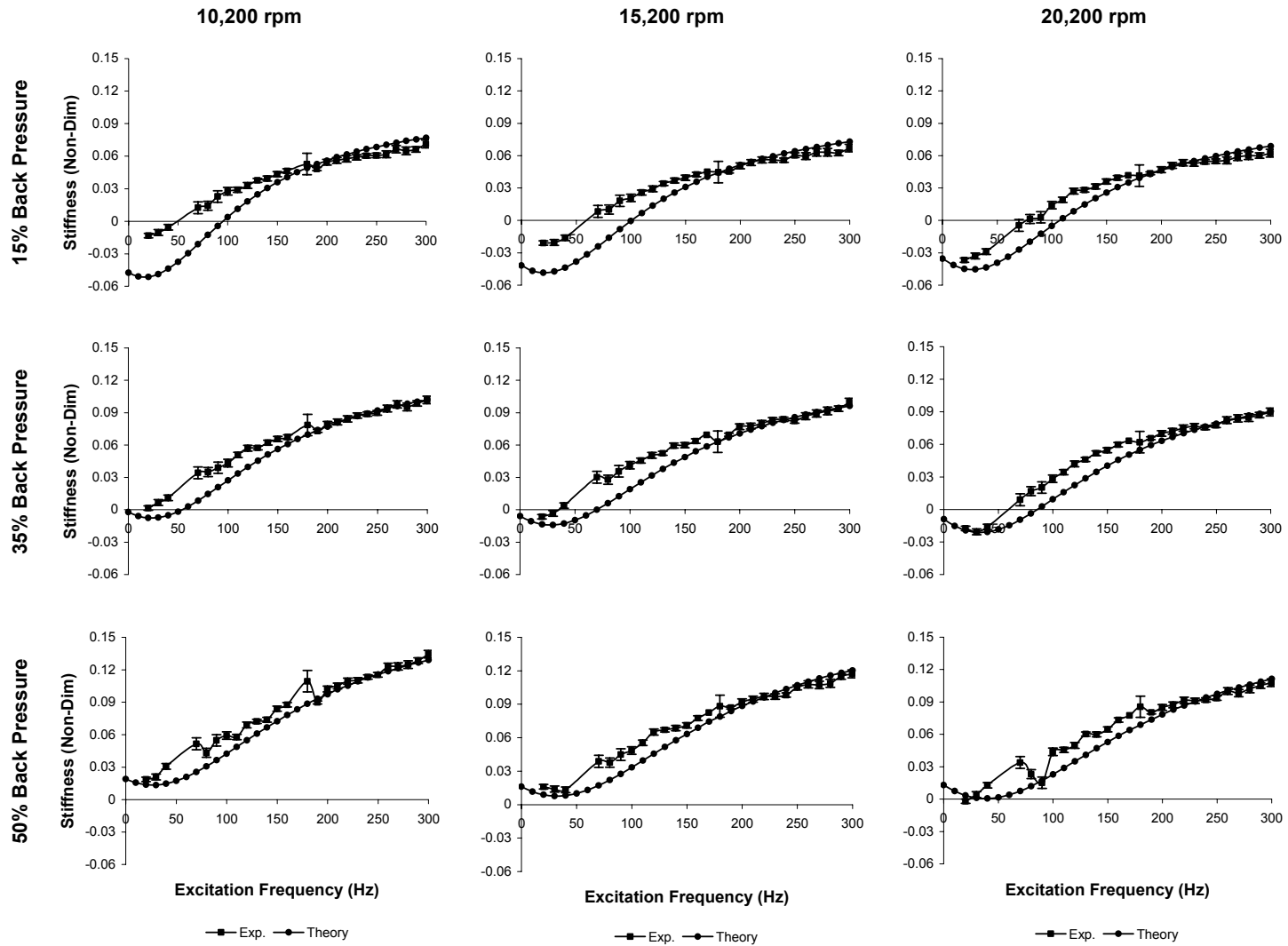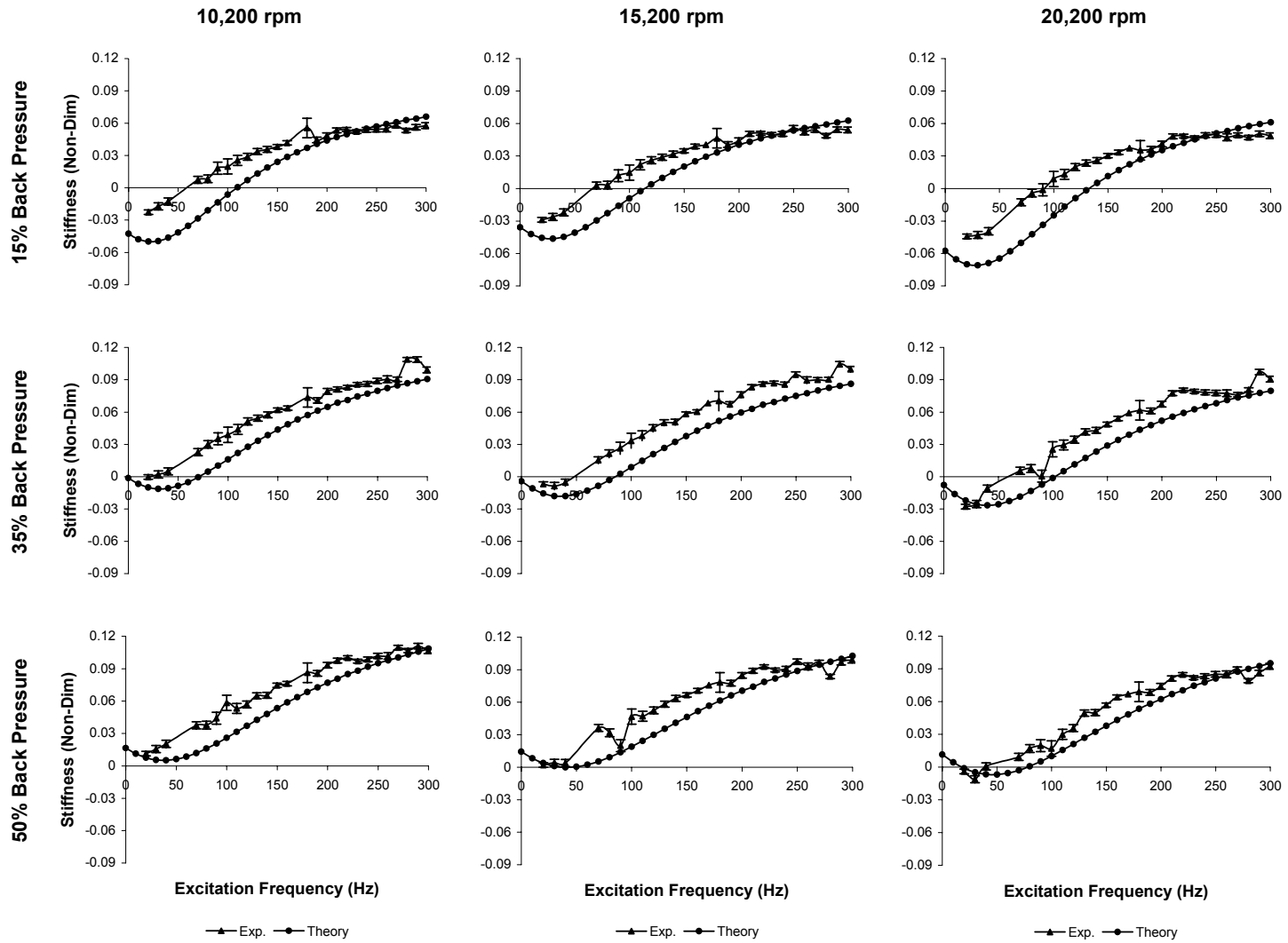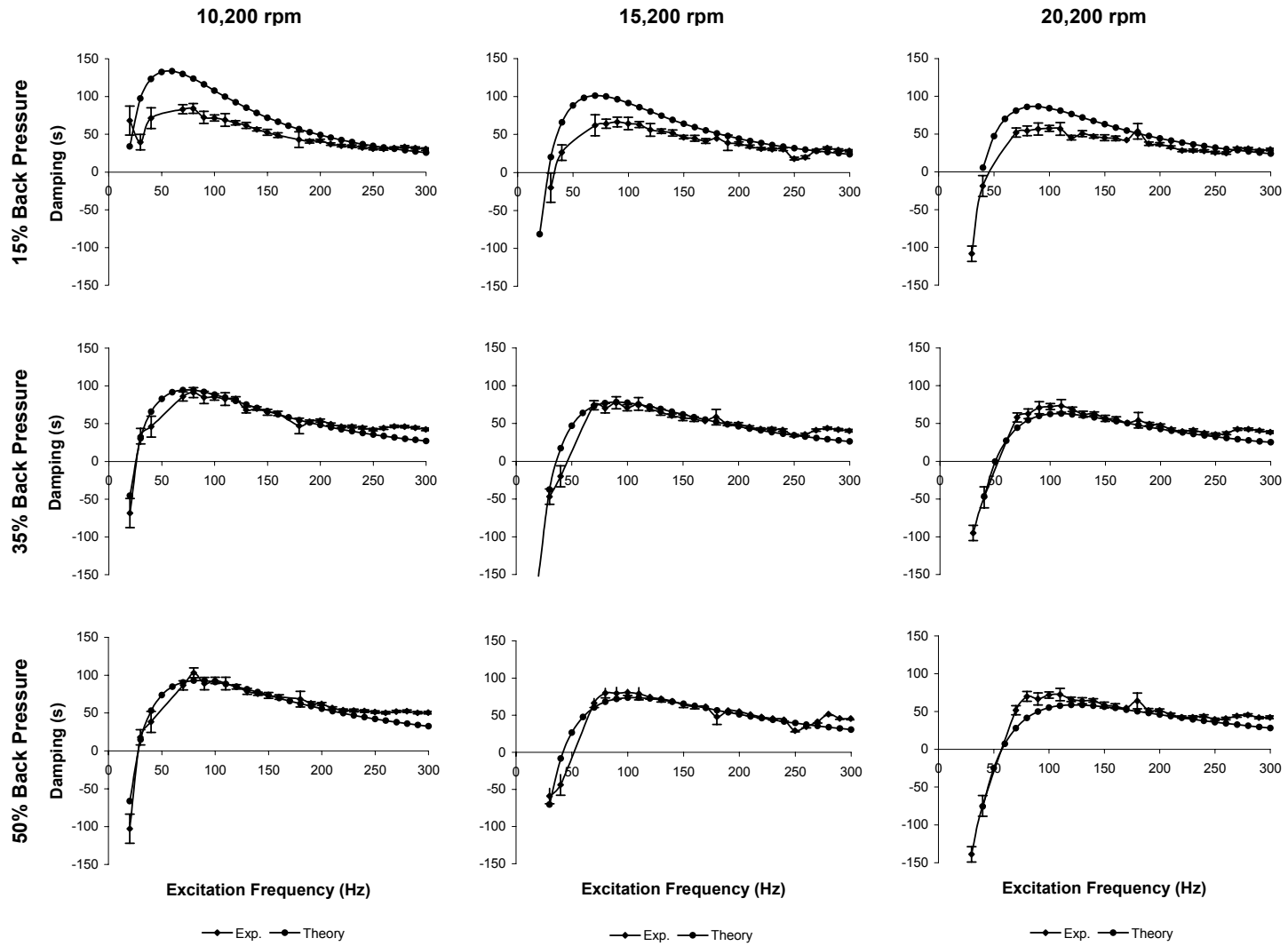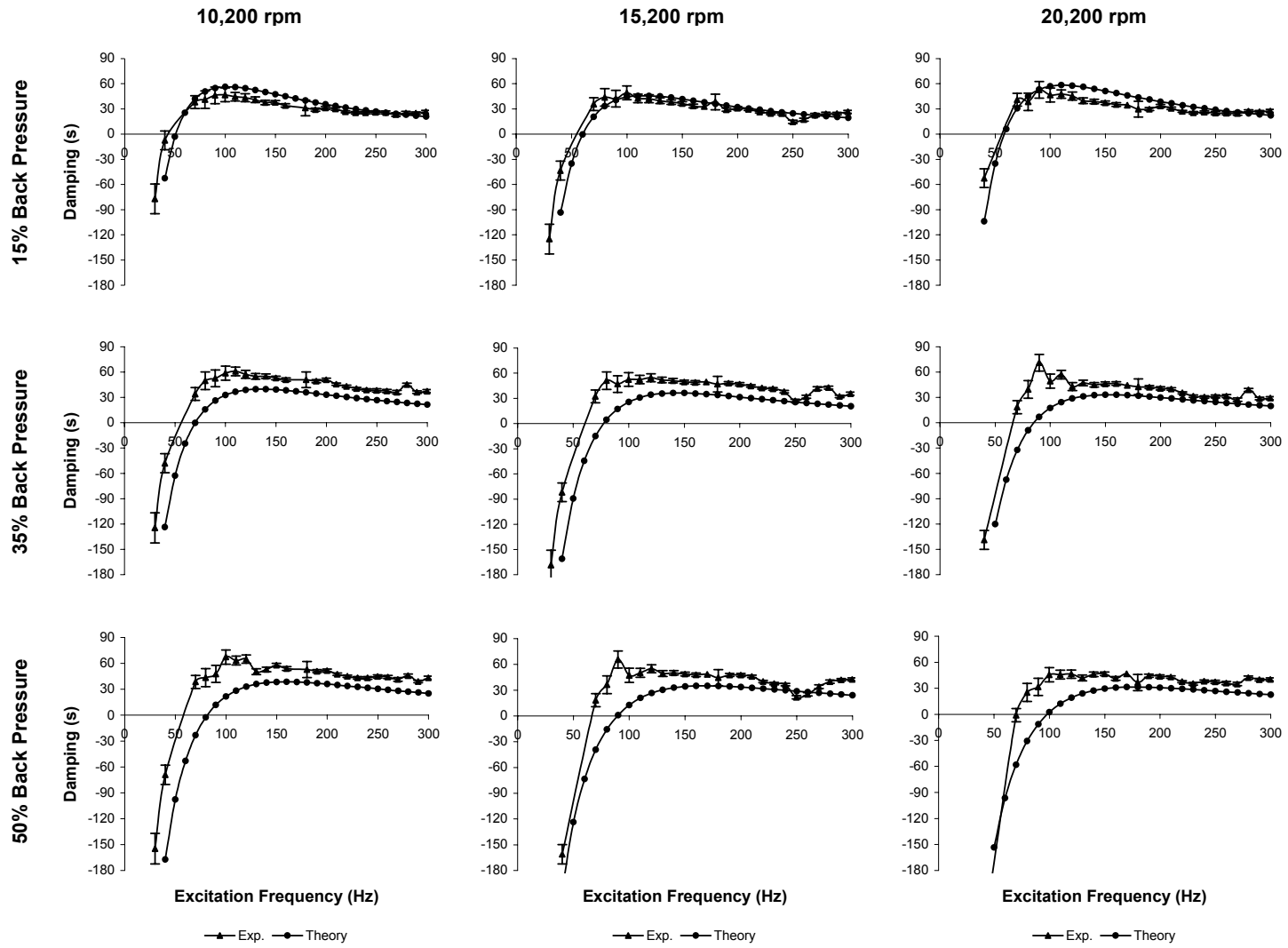**Figure 43: Experimental and Theoretical C_{eff}* Versus Excitation Frequency for High Preswirl**

3.2   Smooth-Bore Seals

Theory for the smooth seal is based on the one-control volume, bulk-flow model. This model predicts K^*, k^*, and C^* to be frequency-independent, as shown in Figures 44 through 49. As with the honeycomb seal results, error bars are included on experimental data to show spread of values measured at each frequency. For low preswirl, the error bars show one standard deviation of about ±30%, ±7%, ±2.5%, ±27%, and ±5% about the mean value of K^*, k^*, C^*, K_{eff}^*, and C_{eff}^*, respectively. The error bars show a standard deviation of about ±28%, ±3.5%, ±5.5%, ±35%, and ±12% about the mean value of K^*, k^*, C^*, K_{eff}^*, and C_{eff}^*, respectively, for medium preswirl. Note the large spread for K^* and K_{eff}^*, which is due to the small measured values near the noise range of the test equipment. Again, there are no results available for the smooth seal at 15% backpressure since the airflow choked at a higher backpressure. Also, there are no results for the high inlet preswirl ring due to instabilities.

Figures 44 and 45 show experiment versus theory for the direct stiffness, K^*, of the smooth seal. Overall, the measured data seems to reflect the frequency-independent nature predicted by the theory, with measured data at 35% backpressure showing a slight slope, or increase in K^* with frequency. The magnitude is obviously under-predicted by theory for all test conditions, considerably for 35% backpressure where values are predicted to be negative. Similar to the 15% backpressure case for the honeycomb seal, theory predicts the airflow to be choked at this backpressure, which could be the cause of predicted negative stiffness values. Theory predicts a larger increase in K^* with an increase in inlet preswirl than was measured, thereby improving correlation between experiment and theory. Theory also over-estimates the decrease in K^* with increased

rotor speed, thereby decreasing correlation. On average, theory under-predicts for low preswirl and 50% backpressure by 50%, 85%, and 118% for low, medium, and high rotor speeds, respectively, and by about 535% for all rotor speeds at 35% backpressure. For medium preswirl, under-prediction averages only 24%, 46%, and 75% for low, medium, and high rotor speeds, respectively, at 50% backpressure, and 230%, 320%, and 517% for low, medium, and high rotor speeds, respectively, at 35% backpressure.

Figures 46 and 47 reflect theory and measured data for cross-coupled stiffness, $k*$. Experimental data, again, seems to validate the prediction by theory of frequency independence. Theory under-predicts measured values of $k*$ for all cases at low preswirl, however, it makes an impressive prediction of the large increase in $k*$ with increased rotor speed. Theory slightly overstates this increase, which causes better agreement between theory and measured data as rotor speed is increased. On average theory under-predicts by 55%, 42%, and 7% for low, medium, and high rotor speeds, respectively Agreement is even better for medium preswirl. Theory under-predicts by no more than 8%, on average, for any test conditions at medium preswirl. Note that backpressure seems to have an insignificant effect on correlation of theory and measured data for $k*$.

Figures 48 and 49 show that the theory again under-predicts values, this time for $C*$. However, theory predicts well the measured insensitivity of $C*$ values to a change in rotor speed, backpressure, or preswirl. The measured data also seems, again, to verify the predicted frequency-independence of $C*$, especially for frequencies above 90 Hz. The 35% backpressure condition shows slightly better agreement, with theory under-predicting by an average of 14%, while the 50% backpressure condition shows an under-prediction of 18%.

Figures 50 and 51 compare theory and measured data for the effective stiffness, $K_{eff}*$, of the smooth seal. Again, as with $K*$, the theory under-predicts the measured data for all test conditions, and largely under-predicts for 35% backpressure. On average, theory under-predicts for low preswirl and 50% backpressure by about 45%, 73%, and 110% for low, medium, and high rotor speeds, respectively. For low preswirl and 35% backpressure, theory under-predicts by 597%, 692%, and 670% for low, medium, and high rotor speeds, respectively. For medium preswirl, under-prediction is slightly less, averaging 51%, 72%, and 107% for low, medium, and high rotor speeds, respectively, at 50% backpressure, and 264%, 340%, and 505% for low, medium, and high rotor speeds, respectively, at 35% backpressure. The large discrepancy at 35% backpressure is due to the relatively small, near zero, measured values in the low to mid-frequency range compared with those predicted by theory.

Theory seems to predict very well in trend for the effective damping $C_{eff}*$, shown in Figures 52 and 53. For low preswirl, theory slightly over-predicts up to a frequency of about 70 Hz, and under-predicts thereafter by about 9% for low and medium rotor speed, and 30% for high rotor speed. The larger under-prediction at high rotor speed is actually due to the more accurately predicted $k*$ at this speed, as discussed earlier and shown in Figure 46. Medium preswirl shows an under-prediction by theory for all frequencies, and for all of the test conditions. Under-prediction is consistently about 46%.

Figure 44: Experimental and Theoretical *K** Versus Excitation Frequency for Smooth Seals at Low Preswirl

Figure 45: Experimental and Theoretical *K** Versus Excitation Frequency for Smooth Seals at Medium Preswirl
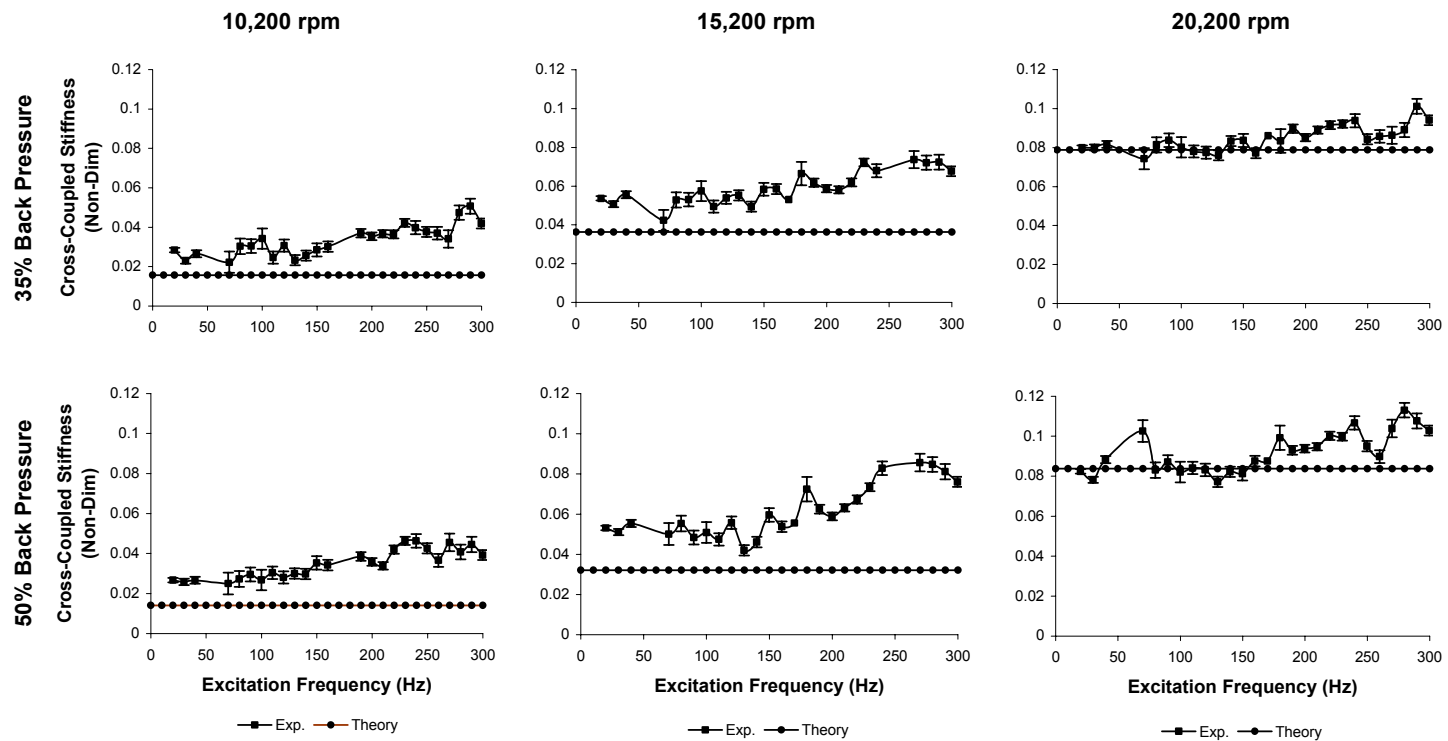
Figure 46: Experimental and Theoretical *k** Versus Excitation Frequency for Smooth Seals at Low Preswirl
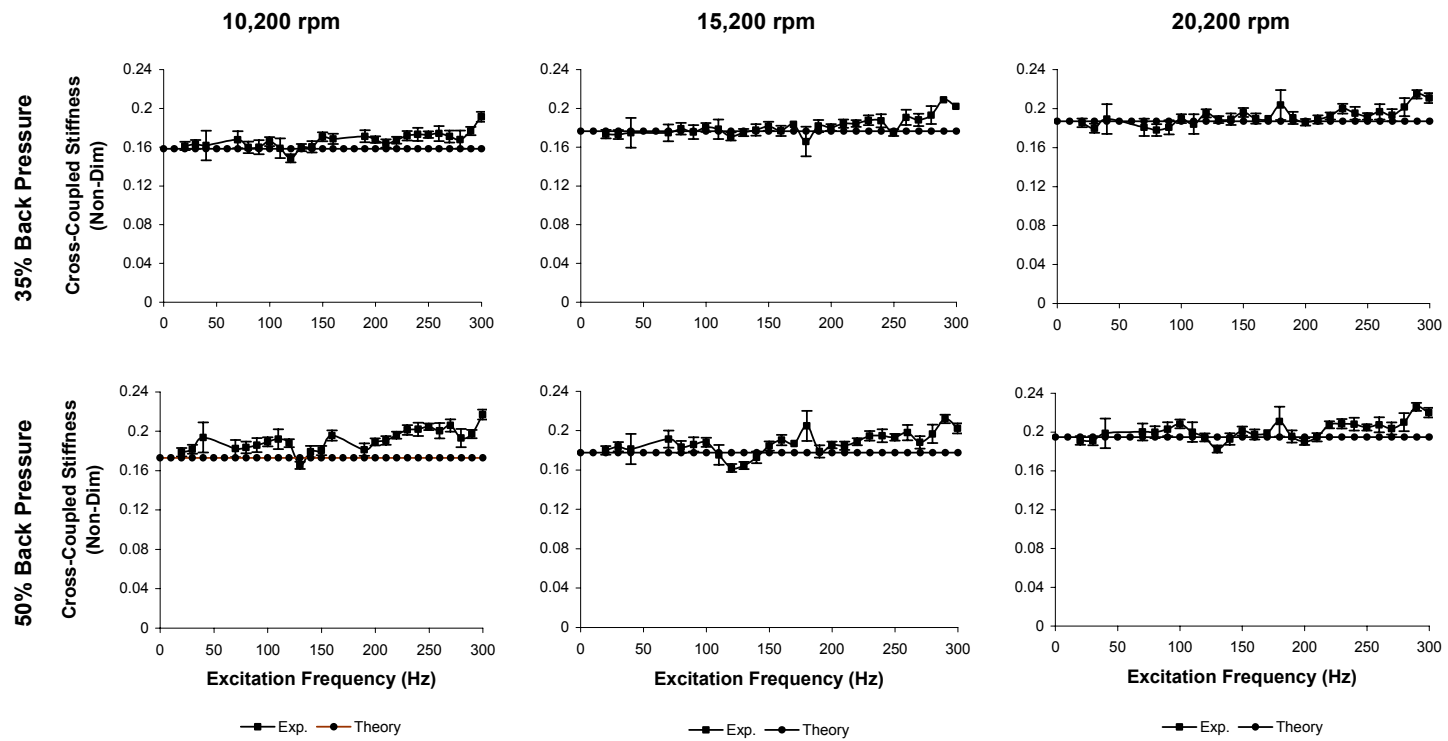
Figure 47: Experimental and Theoretical *k** Versus Excitation Frequency for Smooth Seals at Medium Preswirl
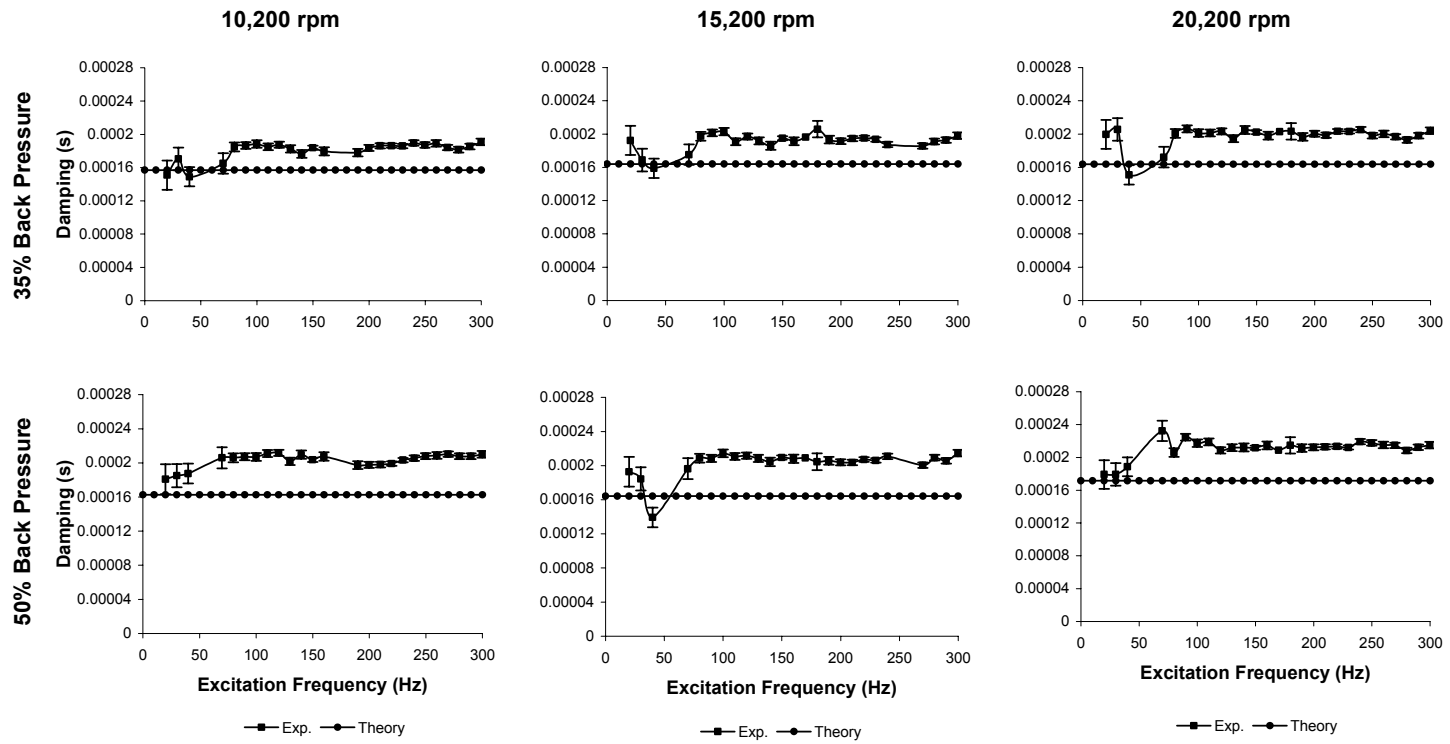
Figure 48: Experimental and Theoretical *C** Versus Excitation Frequency for Smooth Seals at Low Preswirl
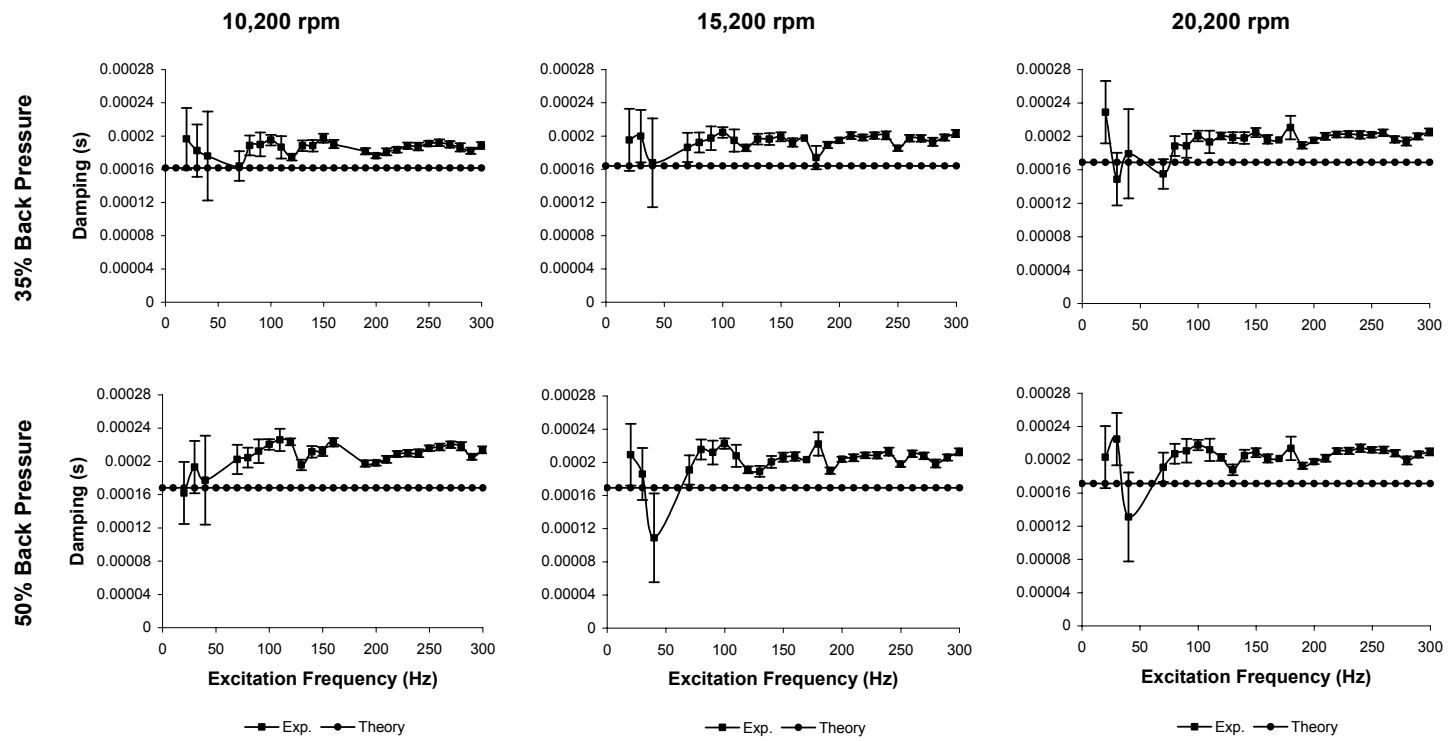
Figure 49: Experimental and Theoretical *C** Versus Excitation Frequency for Smooth Seals at Medium Preswirl
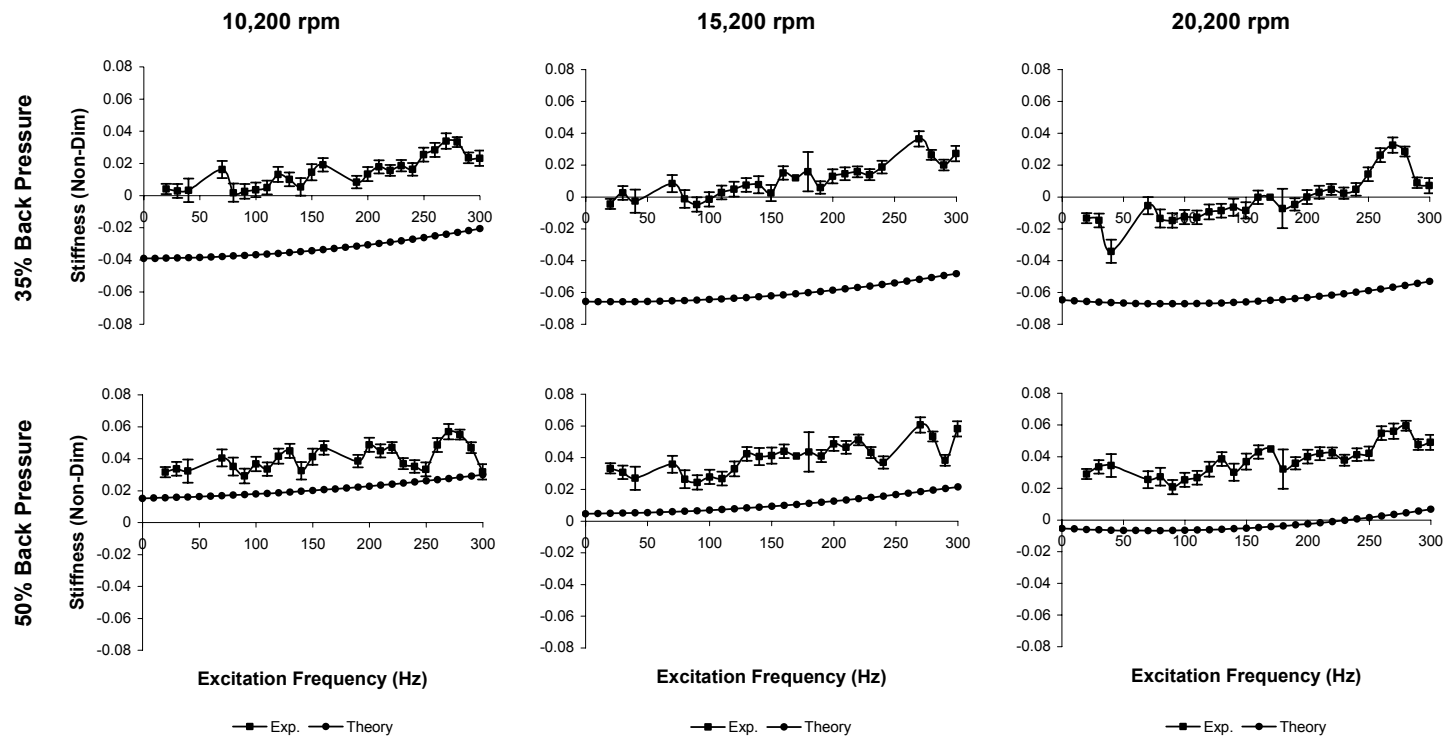
Figure 50: Experimental and Theoretical K_{eff}* Versus Excitation Frequency for Smooth Seals at Low Preswirl
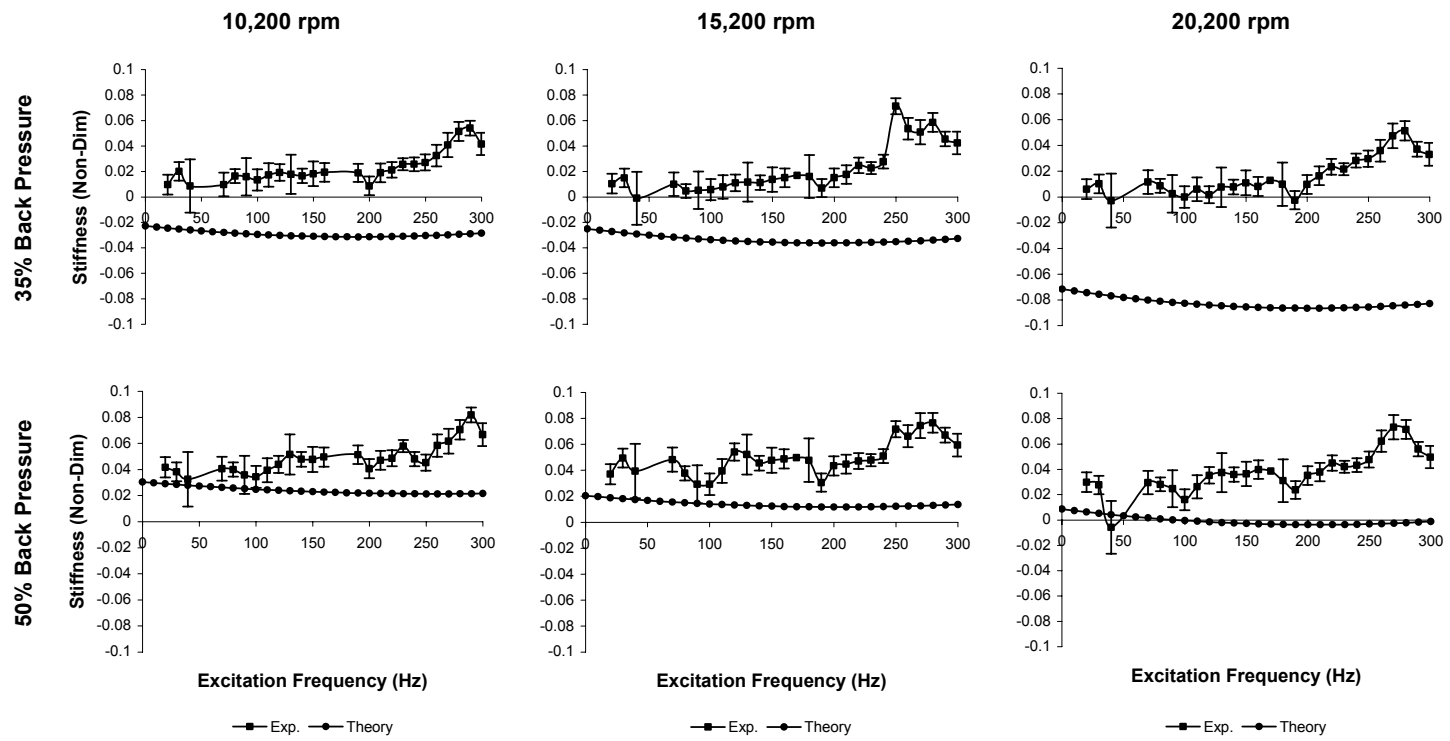
Figure 51: Experimental and Theoretical $K_{eff}*$ Versus Excitation Frequency for Smooth Seals at Medium Preswirl
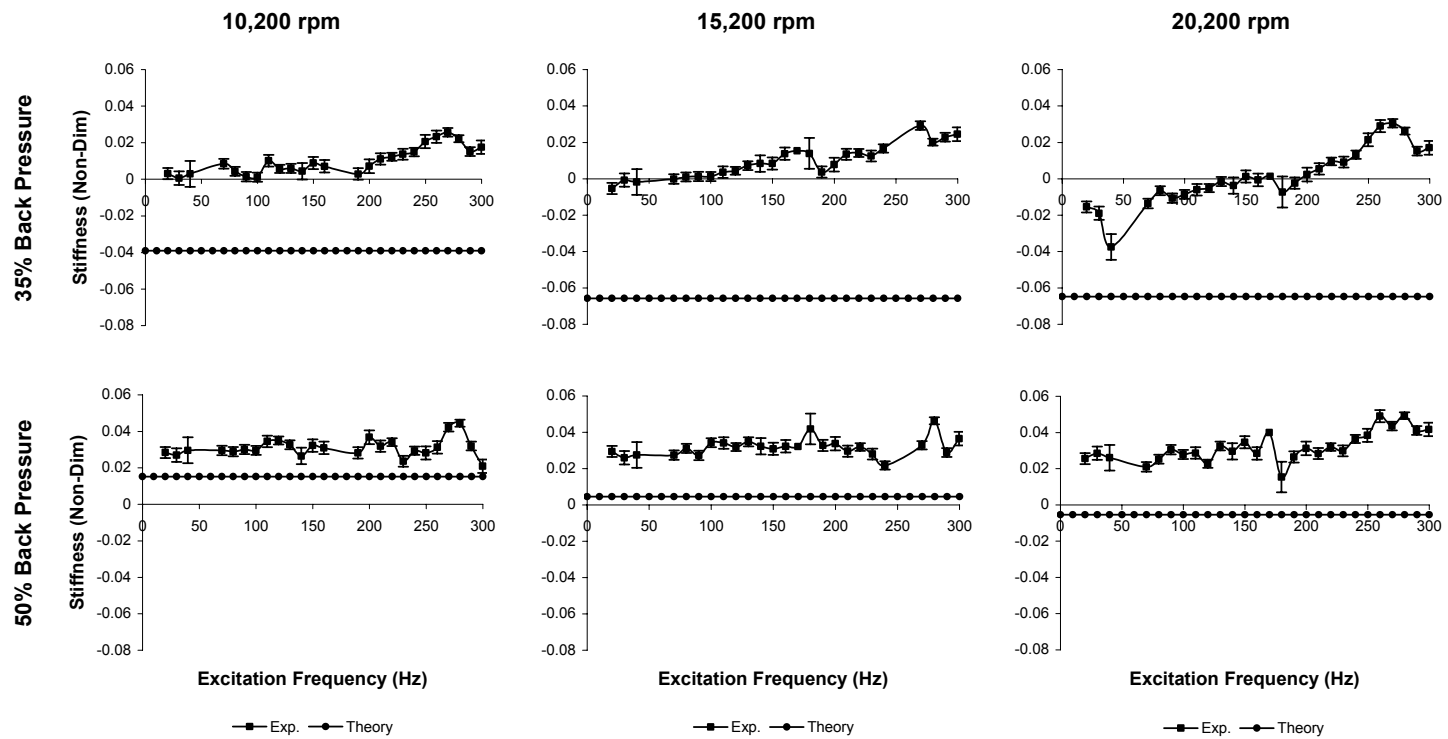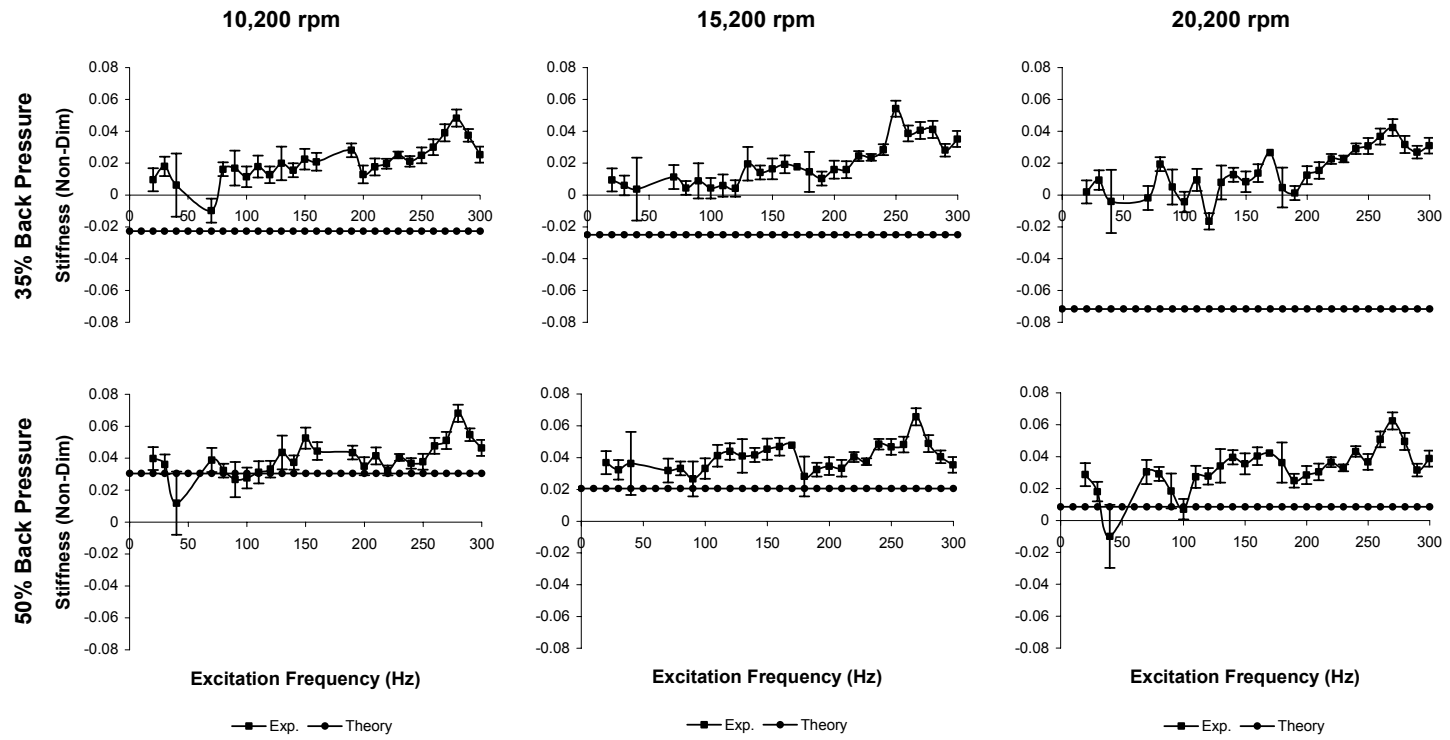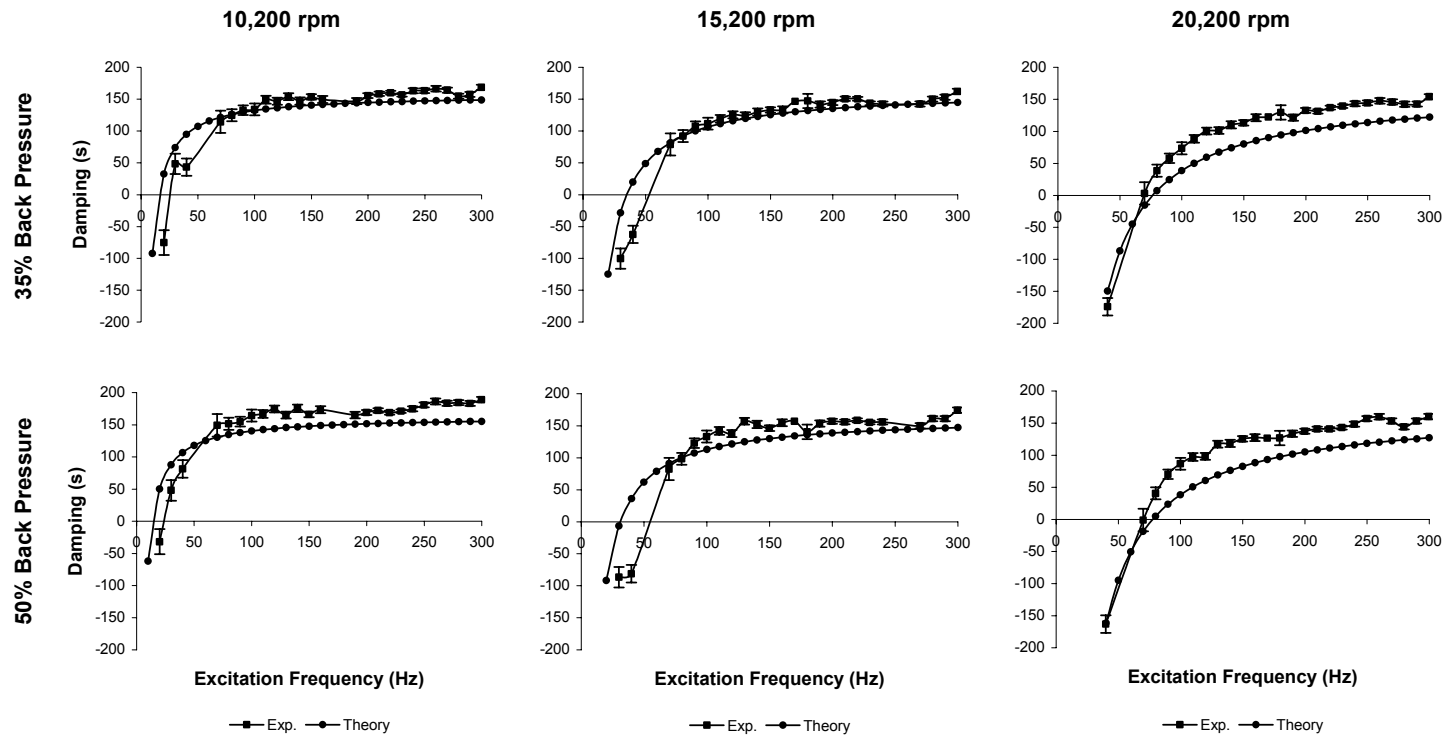
Figure 52: Experimental and Theoretical $C_{eff}*$ Versus Excitation Frequency for Smooth Seals at Low Preswirl
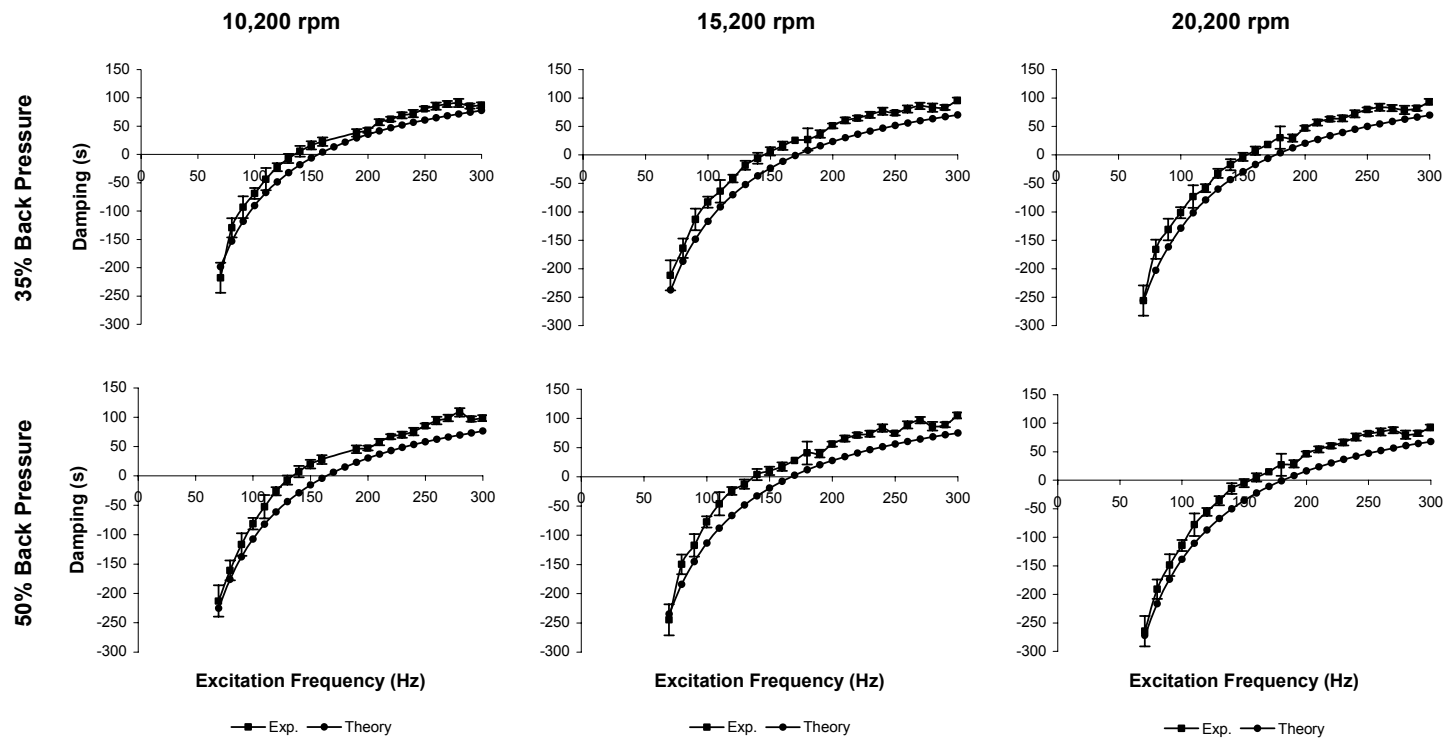
Figure 53: Experimental and Theoretical $C_{eff}*$ Versus Excitation Frequency for Smooth Seals at Medium Preswirl

3.3   Leakage Rates

The mass flowrate through each seal will also be given in a non-dimensional form based on the discharge coefficient, C_d, in Equation 17 below from Childs et al. (1990).

$$\Delta P = C_d \frac{\rho \cdot V^2}{2} \tag{17}$$

A non-dimensional flow coefficient, ϕ, can be derived in terms of mass flowrate, seal geometry, and test conditions using Equation 17 to give,

$$\phi = C_d^{-\frac{1}{2}} = \frac{\dot{m}}{\left(\pi \cdot D_{in} \cdot C_r\right)} \sqrt{\frac{R_c \cdot T_i}{2 \cdot \Delta P \cdot P_i}} \tag{18}$$

A detailed derivation of Equation 18 is given in Appendix C and definitions for the variables and constants are given in the *Nomenclature* section at the beginning of this paper.

Figure 54 represents experimental results and theoretical predictions for both the honeycomb and smooth-bore seals. Again, the smooth seal could not be tested using the 'high' inlet preswirl ring. However, the plots in Figure 54 show that its preswirl ratio obtained with the 'medium' preswirl ring (its 2nd data point on each plot) is close to that of the honeycomb seal using the 'high' inlet preswirl ring (its 3rd data point on each plot).

Observing Figure 54, it is apparent that leakage will increase if the cells of the honeycomb seal become clogged, causing it to behave as a smooth seal. The measured data shows that the smooth seal consistently has about 80% higher leakage than the honeycomb seal, regardless of inlet preswirl ratio or other test conditions. Theory, which has bold curves on the plots, predicts that there is consistently about 56% higher leakage, on average, for the smooth seal, again independent of test conditions.

Comparing theory with measured data for the honeycomb seal, the two-control volume model based on Ha's friction factor coefficients over-predicts leakage under all testing conditions. Careful observation also shows increased over-prediction as both preswirl and rotor speed are increased. The theory curves tend to remain relatively flat, whereas, measured data shows a decrease in leakage with increased preswirl and rotor speed. Specifically, theory over-predicts by about 15% at low preswirl and the low rotor speed, and by about 21% at high preswirl and the high rotor speed.

Using the bulk-flow theory model with Ha's friction factors for the smooth seal produces very impressive agreement with measured data. The theory over-predicts leakage, as with the honeycomb seal, and, again, has increasing disagreement with measured data as preswirl and rotor speed are increased. However, there is, on average, no more than 6% disagreement between measured data and theoretical prediction.
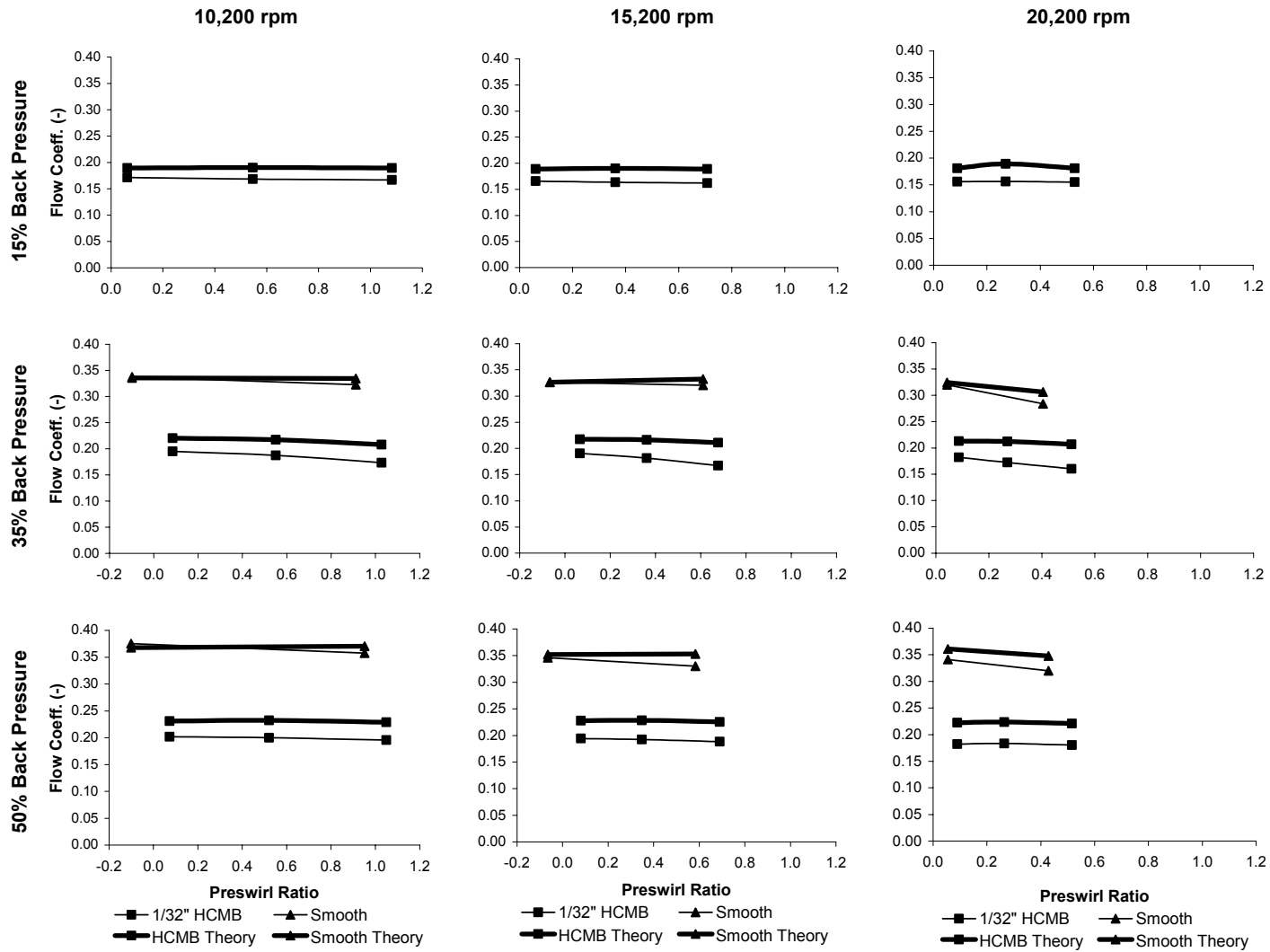
Figure 54: Experimental and Theoretical Leakage Rates for Honeycomb and Smooth Seal

4   SUMMARY AND CONCLUSIONS

The experimental results show that the honeycomb seal has little change in effective stiffness, $K_{eff}*$, as preswirl is increased, and a moderate decrease (~20%) in effective damping, $C_{eff}*$, for each preswirl increase. Also, there is little change (~40 Hz to 70 Hz) in the cross-over frequency, or frequency at which $C_{eff}*$ obtains a positive value and thus becomes stable. Results for the smooth seal shows an increase of up to 98% in $K_{eff}*$, and about a 44% drop in $C_{eff}*$ values when preswirl is increased by using the medium inlet preswirl ring. Also, $C_{eff}*$ shows a large shift (70 Hz to 140 Hz) in its cross-over frequency when the using the medium inlet preswirl ring. Tests using the high preswirl ring could not be conducted for the smooth seal due to instabilities.

Direct comparison of the dynamic coefficients for the honeycomb and smooth seal were made to understand how the honeycomb seal might behave if its cells became clogged and caused it to behave dynamically like a smooth seal. Overall, there is a potential reduction in $K_{eff}*$ of up to 68% for the low preswirl condition and up to 50% for the higher preswirl condition. This could cause a problem if the honeycomb seal is being used to keep a rotor critical speed placed above the operating speed. $C_{eff}*$ values are not degraded for conditions of virtually no preswirl (<0.1). However, for higher preswirl (>0.4), the cross-over frequency for $C_{eff}*$ increases from 70 Hz (honeycomb) to 140 Hz (smooth) with clogged cells due to its loss of ability to effectively mitigate cross-coupled stiffness. Also, comparing values, $C_{eff}*$ for the smooth seal is less than that of the honeycomb seal for frequencies up to about 200 Hz (12000 rpm), which is well within the range of many medium to large compressors and turbines.

The two-control-volume theory model by Kleynhans and Childs (1997) with Ha's

friction factor coefficients seems to follow the frequency-dependent experimental data well for the honeycomb seal. However, correlation in magnitude could use improvement for the 15% backpressure condition and for $K_{eff}*$. Also, the theory seems to over-compensate increases in the values of $k*$ as preswirl is increased. Thus, values for $C_{eff}*$ are typically under-predicted as preswirl is increased, except for 15% backpressure. The measured values for the smooth-bore seal seem to follow the frequency-independent model for $K*$ and $C*$ well in trend. Theory consistently under-predicts for all test conditions and preswirl levels. Theory highly under-predicts $K*$ and $K_{eff}*$ at 35% backpressure for both preswirl levels. However, increases in $k*$ with increased preswirl and rotor speed are predicted very well by theory. Thus, the large drop and shift in measured values of $C_{eff}*$ are predicted well by the theory as well.

Finally, experimental leakage results show a consistent increase of about 80% regardless of preswirl level or other test conditions for the smooth seal compared to the honeycomb seal. Theory predicts a consistent increase of 56% for the same comparisons. This shows the increased leakage to be expected for the honeycomb seal if its cells were to become clogged. Theory over-predicts by about 17% on average for all cases for the honeycomb. Also, it does not predict the measured decrease in leakage with increased rotor speed and preswirl, causing less agreement between theory and experiment. Theory over-predicts for the smooth-bore seal under all test conditions as well, and also does not predict its decrease in leakage with increased rotor speed and preswirl. However, there is no more than 6% disagreement seen between theory and experiment for the smooth seal.

In conclusion, experimental results show that a swirl brake should be used at the inlet of the honeycomb seal if it is being used in a dirty operating environment and it

should be routinely inspected if possible to prevent future stability problems. Theory versus experiment results show that predictions for stability parameters such as k^* and C_{eff}^* are typically conservative and trustworthy. Predictions for K and K_{eff} may possibly be improved with better measured friction factor coefficients for each seal.

REFERENCES

Allaire, P., Gunter, E., Lee, C., and Barrett, L., 1976, "The Dynamic Analysis of the Space Shuttle Main Engine High Pressure Fuel Turbopump Final Report, Part II, Load Capacity and Hybrid Coefficients for Turbulent Interstage Seals", University of Virginia report UVA/528140/ME76/103.

Armstrong, J., and Perricone, F., 1996, "Turbine Instability Solution- Honeycomb Seals", Proceedings of the 25th Turbomachinery Symposium, Turbomachinery Laboratory, Texas A&M University, pp. 47-56.

Black H., and Jenssen, D., 1969, "Effects of Hydraulic Forces in Annular Pressure Seals on the Vibration of Centrifugal Pump Rotors", *Journal of Mechanical Engineering Science*, Vol. 11, No. 2, pp. 206-213.

Black H., and Jenssen, D., 1970, "Dynamic Hybrid Properties of Annular Pressure Seals", *Proc. J. Mechanical Engineering*, Vol. 184, pp. 92-100.

Childs, D., 1983a, "Dynamic Analysis of Turbulent Annular Seals Based on Hirs' Lubrication Equation", ASME *Journal of Lubrication Technology*, Vol. 105, pp. 429-436.

Childs, D., 1983b, "Finite Length Solutions for Rotordynamic Coefficients of Turbulent Annular Seals", ASME *Journal of Lubrication Technology*, Vol. 105, pp. 437-444.

Childs, D., and Moyer, D., 1985, "Vibration Characteristics of the HPOTP (High Pressure Oxygen Turbopump) of the SSME (Space Shuttle Main Engine)", ASME *Journal of Engineering for Gas Turbines and Power*, Vol. 107, No.1, pp. 152-159.

Childs, D., and Kim, C.-H., 1986, "Test Results for Round Hole-Pattern Damper Seals: Optimum Configurations and Dimensions for Maximum Net Damping", ASME *Journal of Tribology*, Vol. 108, pp. 605-611.

Childs D., Elrod, D., and Hale K., 1989, "Annular Honeycomb Seals: Test Results for Leakage and Rotordynamic Coefficients; Comparison to Labyrinth and Smooth Configurations", ASME *Journal of Tribology*, Vol. 111, pp. 293- 301.

Childs D., Nolan, S., Kilgore J., 1990, "Additional Test Results for Round Hole-Pattern Damper Seals: Leakage, Friction Factors, and Rotordynamic Force Coefficients", ASME *Journal of Tribology*, Vol. 112, pp. 365- 371.

Dawson, M. P., 2000, "A Comparison of the Static and Dynamic Characteristics of Straight-Bore and Convergent Tapered-Bore Honeycomb Annular Gas Seals", M.S. Thesis, Turbomachinery Laboratory, Texas A&M University, TL-SEAL-1-00.

Elrod, D., Childs, D., and Nelson, C., 1990, "An Annular Gas Seal Analysis Using Empirical Entrance and Exit Region Friction Factors", ASME *Journal of Tribology*, Vol. 112, No. 2, pp.254-258.

Fleming, D., 1977, "High Stiffness Seals for Rotor Critical Speed Control", Design Engineering Technical Conference, Chicago, ASME Paper 77-DET-10.

Fleming, D., 1979, "Stiffness of Straight and Tapered Annular Gas Seals", ASME *Journal of Lubrication Technology*, Vol. 101, No.3, pp. 349-355.

Ha, T. and Childs, D., 1992, "Friction-Factor Data for Flat-Plate Tests of Smooth and Honeycomb Surfaces," ASME *Journal of Tribology*, Vol. 114, pp. 722-729.

Hirs, G., 1973, "A Bulk-Flow Theory for Turbulence in Lubricating Films", ASME *Journal of Lubrication Technology*, Vol. 95, pp.137-146.

Holt, C.G., 2001, "Rotordynamic Evaluation of Frequency Dependent Impedances of Hole-Pattern Gas Damper Seals", M.S. Thesis, Turbomachinery Laboratory, Texas A&M University, TL-SEAL-1-01.

Kleynhans, G., and Childs, D., 1997, "The Acoustic Influence of Cell Depth on the Rotordynamic Characteristics of Smooth Rotor/ Honeycomb Stator Annular Gas Seals", ASME *Journal of Engineering for Gas Turbines and Power*, Vol. 119, pp. 949-957.

Lomakin, A., 1958, "Calculation of Critical Speed and Securing of the Dynamic Stability Rotors in High-Pressure Hydraulic Machines with Reference to Forces Arising in Seal Gaps", *Energomashinostroenie*, Vol. 4, No.1, pp.1158.

Nelson, C., 1984, "Analysis for Leaking and Rotordynamic Coefficients of Surface-Roughened Tapered Annular Gas Seals", ASME *Journal of Engineering for Gas Turbines and Power*, Vol. 106, pp. 927-934.

Nelson, C., 1985, "Rotordynamic Coefficients for Compressible Flow in Tapered Annular Seals", ASME *Journal of Tribology*, Vol. 107, pp.318-325.

Rouvas, C., 1993, *Parameter Identification of the Rotordynamic Coefficients of High-Reynolds-Number Hydrostatic Bearings,* Ph.D. Dissertation, Texas A&M University.

Vance, John M., *Rotordynamics of Turbomachinery*, John Wiley & Sons, Inc., New York, 1988, p.20.

Von Pragenau, G., L., 1982, "Damping Seals for Turbomachinery", NASA TP-1987, Marshall Space Flight Center, AL.

Wachter, J., and Benkert, H., 1980, "Flow Induced Spring Coefficients of Labyrinth Seals for Applications in Rotordynamics", Proceedings of the Rotordynamic Instability Problems in High-Performance Turbomachinery Workshop, Texas A&M University, NASA CP-2133, pp. 189-212.

Yu, Z., and Childs, D., 1998, "A Comparison of Experimental Rotordynamic Coefficients and Leakage Characteristics Between Hole-Pattern Gas Damper Seals and a Honeycomb Seal", ASME *Journal of Engineering for Gas Turbines and Power*, Vol. 120, pp. 778-783.

Zeidan, F., Perez, R. and Stephenson, E., 1993, " The Use of Honeycomb Seals in Stabilizing Two Centrifugal Compressors", Proceedings of the 22nd Turbomachinery Symposium, Turbomachinery Laboratory, Texas A&M University, pp. 3-15.

APPENDIX A

A.1 Single-Control-Volume Bulk-Flow Model for Smooth Seals

Continuity Equation for Single-Control-Volume Model

$$\frac{\partial}{\partial t}(\rho H) + \frac{1}{R}\frac{\partial}{\partial \Theta}(\rho U H) + \frac{\partial}{\partial Z}(\rho W H) = 0 \tag{19}$$

Axial Momentum Equation for Single-Control-Volume Model

$$-H\frac{\partial P}{\partial Z} = \tau_{sz} + \tau_{rz} + \frac{\partial}{\partial t}(\rho W H) + \frac{1}{R}\frac{\partial}{\partial \Theta}(\rho U W H) + \frac{\partial}{\partial Z}(\rho W^2 H) \tag{20}$$

Circumferential Momentum Equation for Single-Control-Volume Model

$$-\frac{H}{R}\frac{\partial P}{\partial \Theta} = \tau_{s\Theta} + \tau_{r\Theta} + \frac{\partial}{\partial t}(\rho U H) + \frac{1}{R}\frac{\partial}{\partial \Theta}(\rho U^2 H) + \frac{\partial}{\partial Z}(\rho U W H) \tag{21}$$

A.2 Two-Control-Volume Bulk-Flow Model for Honeycomb Seals

 Figure 55 below illustrates the two-control volume model.
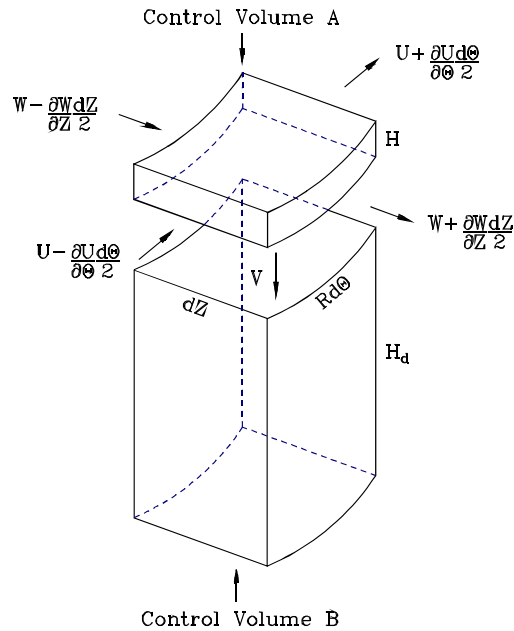
Figure 55: Two-Control Volume Bulk-Flow Model

Continuity Equation for Two-Control-Volume Model (Control Volume A):

$$\frac{\partial}{\partial t}(\rho H) + \frac{1}{R}\frac{\partial}{\partial \Theta}(\rho U H) + \frac{\partial}{\partial Z}(\rho W H) + \rho V = 0 \tag{22}$$

Continuity Equation for Two-Control-Volume Model (Control Volume B):

$$\rho V = H_d \frac{\partial \rho}{\partial t} \tag{23}$$

Axial Momentum Equation for Two-Control-Volume Model:

$$-H\frac{\partial P}{\partial Z} = \tau_{sz} + \tau_{rz} + \rho W V + \frac{\partial}{\partial t}(\rho W H) + \frac{1}{R}\frac{\partial}{\partial \Theta}(\rho U W H) + \frac{\partial}{\partial Z}(\rho W^2 H) \tag{24}$$

Circumferential Momentum Equation for Two-Control-Volume Model:

$$-\frac{H}{R}\frac{\partial P}{\partial \Theta} = \tau_{s\Theta} + \tau_{r\Theta} + \rho U V + \frac{\partial}{\partial t}(\rho U H) + \frac{1}{R}\frac{\partial}{\partial \Theta}(\rho U^2 H) + \frac{\partial}{\partial Z}(\rho U W H) \tag{25}$$

A.3 Friction Factor Model for Single-Control-Volume and Two-Control-Volume Model

Wall Shear Stress:

$$\tau = f\left(\frac{1}{2}\rho U_m^2\right) \tag{26}$$

Blasius Friction Factor Model:

$$f = n\,\mathrm{Re}^m \tag{27}$$

where,

$$\mathrm{Re} = \frac{\rho(2H)U_m}{\mu} \tag{28}$$

APPENDIX B

The actual test conditions for all tests run are given below in Table III for the 0.79mm cell width, 3.2mm cell depth, honeycomb seal, and Table IV for the smooth-bore seal. Each test condition is coded by a four-digit number for brevity. The first digit can either be a 0, 1, or 2, representing low ($\approx$0%), medium (30% of medium rotor speed), or high (60% of medium rotor speed) preswirl, respectively. The second digit can also be a 0, 1, or 2, representing low (10,200rpm), medium (15,200rpm), or high (20,200rpm) rotor speed. The third digit can, likewise, be a 0, 1, or 2, representing low (15%), medium (35%), or high (50%) backpressure. Finally, the last digit represents a static eccentricity of the rotor from the stator center. All tests were performed with no eccentricity, so this digit will, consequently, always be 0.

Table III: Actual Test Conditions for Honeycomb Seals

Test Conditions (by Code)	Reservoir Pressure (bar-a)	Sump Pressure (bar-a)	Pressure Ratio (Pe/Pi) (%)	Temperature Inlet (°C)	Rotational Speed (rpm)	Flow Rate (per seal) (kg/sec)	Preswirl Ratio (Non-dim.)
No Preswirl Ring							
0000	71.52	10.76	15%	18.1	10,212	0.411	0.062
0100	69.24	10.21	15%	18.2	15,215	0.385	0.060
0200	48.90	7.03	14%	16.9	20,225	0.257	0.088
0010	70.90	25.66	36%	19.1	10,209	0.401	0.084
0110	71.45	25.52	36%	19.6	15,210	0.396	0.066
0210	70.34	24.21	34%	19.8	20,194	0.376	0.086
0020	69.52	32.28	46%	16.8	10,208	0.374	0.073
0120	70.00	31.86	46%	17.1	15,200	0.366	0.080
0220	70.76	30.90	44%	17.1	20,207	0.353	0.090
Medium Preswirl Ring							
1000	69.93	11.17	16%	12.8	10,194	0.396	0.546
1100	70.21	11.10	16%	13.1	15,207	0.386	0.361
1200	70.00	10.97	16%	13.3	20,187	0.369	0.270
1010	70.83	25.52	36%	8.9	10,198	0.393	0.550
1110	71.86	25.10	35%	9.4	15,200	0.388	0.361
1210	72.14	24.48	34%	9.9	20,203	0.373	0.270
1020	70.00	33.66	48%	11.5	10,209	0.371	0.521
1120	70.07	32.69	47%	12.1	15,202	0.362	0.348
1220	70.83	31.93	45%	12.6	20,222	0.353	0.264
High Preswirl Ring							
2000	71.24	10.69	15%	23.3	10,209	0.395	1.082
2100	70.48	10.41	15%	23.6	15,207	0.380	0.708
2200	69.66	10.14	15%	24.0	20,204	0.360	0.530
2010	50.34	18.00	36%	8.1	10,203	0.259	1.028
2110	51.03	17.79	35%	8.3	15,210	0.255	0.677
2210	51.38	17.24	34%	9.2	20,207	0.248	0.512
2020	72.00	32.83	46%	20.6	10,216	0.376	1.050
2120	70.69	31.59	45%	21.3	15,214	0.358	0.690
2220	71.79	31.03	43%	21.9	20,209	0.352	0.515

Table IV: Actual Test Conditions for Smooth-Bore Seals

Test Conditions (by Code)	Reservoir Pressure (bar-a)	Sump Pressure (bar-a)	Pressure Ratio (Pe/Pi) (%)	Temperature Inlet (°C)	Rotational Speed (rpm)	Flow Rate (per seal) (kg/sec)	Preswirl Ratio (Non-dim.)
No Preswirl Ring							
0010	69.59	25.38	36%	21.3	10,194	0.678	-0.098
0110	69.93	25.03	36%	21.4	15,194	0.661	-0.066
0210	69.66	24.48	35%	23.8	20,209	0.646	0.042
0020	68.62	32.48	47%	29.8	10,210	0.667	-0.101
0120	71.24	32.83	46%	18.3	15,207	0.658	-0.065
0220	70.69	32.14	45%	28.8	20,200	0.636	0.055
Medium Preswirl Ring							
1010	50.00	19.17	38%	16.9	10,219	0.462	0.912
1110	49.31	18.90	38%	17.9	15,192	0.452	0.610
1210	36.21	12.62	35%	18.6	20,196	0.301	0.405
1020	69.86	34.28	49%	19.3	10,213	0.647	0.952
1120	48.97	23.17	47%	17.5	15,192	0.427	0.583
1220	49.45	22.76	46%	17.2	20,196	0.423	0.429

APPENDIX C

The flow coefficient is based on the discharge coefficient, C_d, defined by Equation 17:

$$\Delta P = C_d \frac{\rho \cdot V^2}{2} \tag{17}$$

A non-dimensional flow coefficient, ϕ, can be defined using the inverse square root of the discharge coefficient as follows:

$$\phi = C_d^{-\frac{1}{2}} = \sqrt{\frac{\rho \cdot V^2}{2 \cdot \Delta P}} \tag{29}$$

The average axial flow velocity, V, can be defined in terms of mass flowrate and seal geometry using Equation 30:

$$V = \frac{\dot{m}}{\rho \cdot A_c} = \frac{\dot{m}}{\rho \cdot (\pi \cdot D \cdot C_r)} \tag{30}$$

Substituting back into Equation 29 gives,

$$\phi = C_d^{-\frac{1}{2}} = \frac{\dot{m}}{(\pi \cdot D \cdot C_r)} \sqrt{\frac{1}{2 \cdot \Delta P \cdot \rho}} \tag{31}$$

Finally, substituting $\rho = P/R_cT$ for the fluid at the seal inlet gives Equation 18:

$$\phi = C_d^{-\frac{1}{2}} = \frac{\dot{m}}{(\pi \cdot D \cdot C_r)} \sqrt{\frac{R_c \cdot T_i}{2 \cdot \Delta P \cdot P_i}} \tag{18}$$

VITA

Tony Brandon Sprowl was born on October 22, 1974 in Bossier City, LA, but spent most of his adolescent years in Lafayette, LA. In May of 1999, he graduated as outstanding graduate of the Department of Mechanical Engineering with a Bachelor of Science degree from the University of Southwestern Louisiana. Brandon also worked as an accompanying student at NASA-Marshall Space Flight Center in the summer of 1998. From 1999 to 2001, he attended Texas A&M University as a full time graduate student. Currently, he resides in Fort Worth, TX, where he is working as a structural engineer for Bell Helicopter Textron. Brandon can be reached at the following permanent address:

Tony Brandon Sprowl

717 Red Elm Ln.

Fort Worth, TX 76131